To the Graduate Council

I am submitting herewith a thesis written by Jennifer Lynn Parsons entitled “Modeling the Wall Effects of a Tissue Equivalent Proportional Counter Using MCNP ” I have examined the final copy of this thesis for form and content and recommend that it be accepted in partial fulfillment of the requirements for the degree of Masters of Science, with a major in Nuclear Engineering

Dr Lawrence W Townsend, Major Professor

We have read this thesis
and recommend its acceptance

Dr Laurence F Miller

Dr Ronald E Pevey

Accepted for the Council

Associate Vice Chancellor and
Dean of The Graduate School

Modeling the Wall Effects of a Tissue Equivalent Proportional Counter Using MCNP

A Thesis
Presented for the
Master of Science
Degree
The University of Tennessee, Knoxville

Jennifer Lynn Parsons
May 2000

ACKNOWLEDGEMENTS

Without the help of many individuals, I would not have been able to cover such an extensive subject. I wish to gratefully thank Dr. Thomas Borak of Colorado State University, Dr. Les Braby of Texas A&M University, and Dr. Francis Cucinotta of NASA Johnson Space Center for their assistance in this study. I would also like to thank Dr. Ronald Pevey and Dr. Laurence Miller of the University of Tennessee for agreeing to sit on my committee. Lastly, I would like to thank Dr. Lawrence Townsend, my committee chair and advisor, for providing me the wonderful opportunity to work on this study and for encouraging and guiding me throughout every step of this study. This research was performed under an appointment to the U.S. Department of Energy Nuclear Engineering and Health Physics Fellowship Program sponsored by DOE's Office of Nuclear Energy, Science and Technology.

ABSTRACT

Tissue equivalent proportional counters (TEPCs) utilize tissue equivalent materials to depict homogeneous microscopic volumes of human tissue. Although both the walls and gas simulate the same medium, they respond to radiation differently. Differences between the densities of the two materials cause distortions in the measured spectra, called wall effects. The most common type of wall effect is caused by delta rays given off when charged particles strike the TEPC. The number of delta rays that enter the gas cavity of the TEPC is often greater than the number that appear in the microscopic volume. A Monte Carlo transport code, MCNP, is chosen to simulate the transport of secondary electrons, or delta rays, within a TEPC The TEPC modeled in this study is composed of A-150 tissue equivalent plastic and propane-based tissue equivalent gas. The Rudd model is used to describe the secondary electron energy spectrum obtained by the impact of two iron beams, 250 and 1050 MeV nucleon^{-1}, on water. The wall effects in a TEPC are characterized by changing the source location, on either side of the TEPC wall, and by excluding the solid wall.

A comparison of flux responses with and without delta rays or re-entrant particles shows that the delta rays or re-entrant particles in either the gas/wall consistently directed the flux response for the gas/wall much higher than would be normally seen in a microscopic volume of tissue. Another comparison between a solid-wall TEPC and a wall-less one illustrates that the wall attenuates the lower energy electrons at a much higher rate than the higher energy electrons. This causes a lower initial flux of particles that enter the gaseous volume for the lower end of the secondary electron energy spectrum

In addition to characterizing the flux response, the energy deposition as a function of impact parameter within the TEPC is evaluated. The wall-less TEPC has a higher lineal energy as a function of impact parameter than the solid-wall TEPC The wall-less TEPC gives a much better approximation of a microscopic volume. The most important conclusion about the lineal energy within a solid-wall TEPC is that MCNP has the ability to adequately model wall effects in a TEPC.

TABLE OF CONTENTS

LIST OF FIGURES

LIST OF TABLES

1. INTRODUCTION

The study of energy deposition in small volumes by ionizing radiation is microdosimetry. Microdosimetry deals with small volumes that are on the scale from about 1 μm to 1 nm. These distances are comparable to the diameter of most cells down to the diameter of the DNA double helix (1). H.H. Rossi launched the study of microdosimetry in the early 1950s when he "recognized the fundamental difference between absorbed dose and the corresponding random variables that are described by probability distributions" (2). Rossi and his colleagues developed experimental methods to analyze "the microscopic distribution of energy deposition in irradiated matter" (3) and "to measure random fluctuations of energy deposition" (2).

During this time Rossi et al developed the original Rossi counter at the Radiological Research Laboratories of Columbia University (3). This counter, in its various and modified forms, is still used today to study experimental microdosimetry. A Rossi counter is a spherical or cylindrical, walled or wall-less proportional counter with inner cavity diameters ranging from 6 mm to 20 cm that are used to simulate microscopic tissue regions. Today these counters are called tissue equivalent proportional counters (TEPC). TEPCs have the same general characteristics as the original Rossi counter, but as research in the field of microdosimetry has progressed, they have been improved and studied more closely.

This closer look has given insight to one of the major problems with TEPCs – the effect of a solid wall on the detection of incoming radiation within a gaseous volume This effect is called "the wall effect." Once researchers noted this problem, other forms of TEPCs were developed to aid in the reduction of the magnitude of the wall effect. These detectors are called wall-less counters and exist in two types. The first type is a truly wall-less counter that utilizes field-shaping electrodes to contain the gaseous volume The second type is the tissue equivalent grid that reduces the wall solid area to ten percent of the total surface area (3). Although these detectors are useful, it is still easier to work with a solid wall detector; therefore, it has become necessary to find ways to estimate the effect that the walls will have on the measurement of a TEPC. This is especially necessary now because microdosimetry has become more applicable to many different and practical applications. These applications range from radiation chemistry to radiation therapy, and include radiobiology, radiation protection, and risk assessment

This study seeks to characterize the wall effects of a tissue equivalent proportional counter through the use of a Monte Carlo transport method, MCNP This characterization is attained through multiple comparisons based on the type of beam used to produce the secondary electron source and on the location of the electron source within the TEPC. Beam types include a 1050 MeV nucleon^{-1} iron beam and a 250 MeV nucleon^{-1} iron beam. Possible secondary electron source locations include placing the electron source on the inside of the solid wall, on the outside of the solid wall, and on the outside of the gaseous volume when there is no solid wall present. The final characterizations of the wall effects for the 1050 MeV nucleon^{-1} iron beam are then compared to experimental results performed by S.E. Rademacher et al (4) to determine the validity of modeling the wall effects using MCNP.

The following chapters demonstrate how the wall effects of a tissue equivalent proportional counter are characterized Chapter II presents the conceptual development behind the information used in this study. This section presents a review of cell sensitivity to radiation, interactions of charged particles, fundamentals of proportional counters, and the basic theory of electron transport in a Monte Carlo transport code, MCNP. The input file illustrating the tissue equivalent proportional counter design, source and setup is presented in Chapter III. This chapter also includes the method behind the determination of the electron source, data collection and statistical analysis. The results are given in Chapter IV. This chapter also describes, more in detail, the calculations used to generate the appropriate results. Chapter V presents and discusses conclusions, and Chapter VI presents recommendations for future work. Appendices include Rudd model calculations, alternate MCNP input files and portions of the MCNP output files

2. CONCEPTUAL DEVELOPMENT

This study deals with charged particles from an energetic iron beam striking a tissue equivalent proportional counter and creating secondaries, which cause errors in the response of the detector. These secondaries, mostly in the form of delta rays, are modeled using a Monte Carlo code package, MCNP4B. This section begins with a review of cell sensitivity to radiation and the interactions between radiation and tissue It then looks at linear energy transfer versus lineal energy, the interactions of charged particles, the fundamentals of proportional counters, and the basic theory of electron transport in the MCNP transport code.

2.1. REVIEW OF CELL SENSITIVITY TO RADIATION

The human body, besides being composed of 61 percent water, contains other essential compounds including proteins, nucleic acids, fats and enzymes. The chemical composition by weight for the elements within the human body is 10% hydrogen, 18% carbon, 3% nitrogen, 65% oxygen, 1.5% calcium, 1% phosphorus, and less than 1% of other elements (5). The typical diameter of a cell is on the order of 10^{-5} meters, while the diameter of a DNA (deoxyribonucleic acid) double helix within the cell nucleus is about 2×10^{-9} meters, or 2 nm (6).

Cells are sensitive to radiation depending on their rate of division and their location within the cell cycle. The most radiosensitive phases of the mammalian cell cycle are the mitotic and growth phases, while the DNA synthesis phase is the most resistant to radiation. Table 2.1 categorizes the sensitivity of mammalian cells according to division rate (6). As the rate of division increases and the amount of differentiation decreases, the sensitivity to radiation increases. Differentiation refers to the cell's ability to perform a specific function. The last group (fixed postmitotic cells) requires the highest doses of radiation in order to die, and is therefore the group which is most resistant to radiation. As can be seen in Table 2.1, more radiation is needed to destroy the functioning ability of the cell than to stop the mitotic ability of a dividing cell (6).

Cell damage occurs when incoming radiation delivers extra energy, which causes physical and chemical effects, to the cell The extra energy may be utilized to destroy parts or entire functions of the cell. Radiation interaction can happen anywhere within the cell, including DNA strands or chromosomes. Within DNA strands, radiation can produce single-strand or double-strand breaks. If a break occurs in a single strand, DNA is easily repaired by using the opposite DNA strand as a template. If a break

Table 2.1. Categories of Mammalian Cell Sensitivity. (6)

Cell Type	Properties	Examples	Sensitivity
Vegetative intermitotic cells	Divide regularly; no differentiation	Erythroblasts; intestinal crypt cells; germinal cells of epidermis	High
Differentiating intermitotic cells	Divide regularly; some differentiation between divisions	Myelocytes	↑
Connective tissue cells			↑
Reverting postmitotic cells	Do not divide regularly; variably differentiated	Liver	↑
Fixed postmitotic cells	Do not divide; highly differentiated	Nerve cells; muscle cells	Low

occurs in both strands, but the breaks are well separated, the DNA is also easily repaired because each break is treated as a separate event. However, if the breaks in both strands occur opposite or nearly opposite each other, the resulting double-strand break is not readily repaired. If a double-strand break is copied during cell mitosis, a cell mutation or fatality may occur.

The next section describes the effect that linear energy transfer has on DNA in the production of double-strand breaks and discusses the difference between linear energy transfer and lineal energy.

2.2. EFFECT OF LINEAR ENERGY TRANSFER ON DNA

Linear energy transfer (LET) is the average energy imparted to the medium (dE) by a charged particle of a specific energy per distance traveled by the particle (dl) LET is written as.

$$LET = \frac{dE}{dl}. \tag{2.1}$$

In the production of a double-strand break in a DNA molecule, a particle of high linear energy transfer (LET) is more efficient than one of low LET. Electrons, beta particles, gamma rays, and x-rays are examples of low LET particles. Neutrons, protons, alphas, and heavy ions are high LET particles. A low LET particle may deposit more energy in a single collision, but the probability of a large energy deposition in one pass of the strand is incredibly small The high LET particle causes more damage

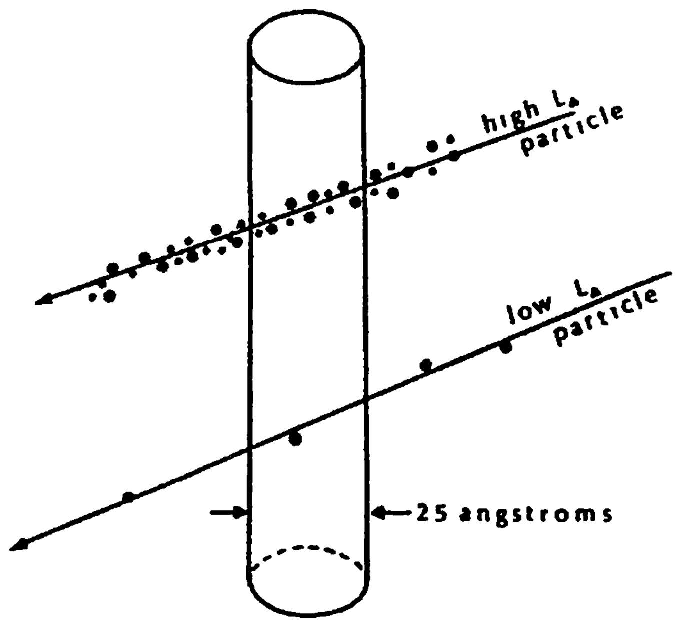

Figure 2.1. Ionization density near a DNA molecule for a low LET particle and a high LET particle. (7)

because it deposits more energy in one pass (7). Figure 2.1 depicts this difference between high and low LET particles as the particles interact with a DNA strand. The cylinder in this figure represents the DNA double helix.

The optimal value of LET (100 keV μm^{-1}) occurs when the average separation between ionizing events coincides to the diameter of the DNA double helix (6). Radiation with this value of LET has the ability to efficiently produce double-strand breaks in the DNA with a single track. More densely ionizing radiation, or those with a larger LET, will also cause double-strand breaks. As LET increases, the "complexity of DNA damage increases, while the total yield of strand breaks remain constant" (8).

However, because ionizing events are clustered together with high LET radiation, energy is wasted.

Table 2.2 gives a summary of the average yield of damage in a single cell after 1 Gray (100 rad) of radiation. The effects in this table are given as a function of low LET, electron track-ends and high LET (8).

Table 2.2. Average yield of damage in a single mammalian cell after 1 Gy of radiation. (8)

Radiation	Low-LET	Electron track-ends	High-LET
Tracks in nucleus	1000	1100	2
Ionization in nucleus	100,000	100,000	100,000
Ionization in DNA	1500	1500	1500
Excitation in DNA	1500	1500	1500
Base damage	10^4	10^4	10^4
DNA ssb[a]	850	500	450
8-Hydroxyadenine	700	--	--
Hydrogen peroxide	5×10^5	--	--
RBE[b] for DNA dsb[c]	~ 1	~ 1	~ 1
PCC[d] breaks: initial	6	--	12
8 h:	< 1	--	4
DNA protein crosslink	150	--	--
Chromosome aberration	0 3	--	2.5
Dicentric	0.1	--	0.8
Complex aberration	10%	20%	45%
Chromosome instability	< 10%	50%	40%
HPRT[e] mutation	10^{-6}	10^{-5}	10^{-5}
Lethal lesions	0.5	1.1	2.6
Cell inactivation	30%	60%	85%

[a]ssb – single-strand break
[b]RBE – relative biological effectiveness,
[c]dsb – double-strand break
[d]PCC – prematurely condensed chromosomes
[e]HPRT – hypoxanthine-guanine phosphoribosyl transferase

2.2.1. Linear Energy Transfer Versus Lineal Energy

At the microscopic level, LET is meaningless because the energy per unit track length varies over a wide range, and an average does not appropriately describe the energy transferred. Therefore, a different quantity was developed for microscopic volumes. Lineal energy is the microscopic quantity corresponding to the LET. According to ICRU Report 36, lineal energy is defined as the energy imparted to matter in a specified volume (ΔE) by a single energy deposition event per mean chord length (⟨x⟩) for that volume and is given as:

$$y = \frac{\Delta E}{\langle x \rangle}. \qquad (2.2)$$

Lineal energy is normally given in units of keV μm^{-1} (3). The mean chord length, as given by the Cauchy relation, is ⟨x⟩ = 4V/S, where V is the volume and S is the surface area For a sphere of radius R, ⟨x⟩ = 4R/3 (3).

Because LET is an average over an entire spatial region, it is sufficient for use with radiation effects on organs or large numbers of grouped cells. However, it is less applicable for damage to single cells. During irradiation, some cells endure lethal damage while other cells survive unharmed. In this situation, LET averages over all the cells and does not distinguish between those cells that survive and those cells that die, but lineal energy treats each cell separately.

2.3. CHARGED PARTICLE INTERACTIONS

Charged particles include electrons, positrons, protons, deuterons, alphas, and heavy ions. While traveling through matter, these charged particles can lose energy by one of the following four mechanisms:

1. Coulomb interactions with electrons and nuclei
2. emission of Bremsstrahlung
3. nuclear interactions
4. emission of Cerenkov radiation.

Bremsstrahlung is electromagnetic radiation that is emitted when a charged particle is accelerated or decelerated Nuclear interactions are only important for heavy incoming ions When a particle travels with a speed greater than the speed of light in a medium, visible electromagnetic radiation, called Cerenkov radiation, is emitted (5) Coulomb interactions are the only method that will be considered in this study.

2.3.1. Coulomb Interactions

Interactions may occur between a fast charged particle and an atomic electron or nucleus. Because the radius of the nucleus ($1x10^{-14}$ m) is smaller than the radius of the atom ($1x10^{-10}$ m), collisions with the atomic electrons occur more often and therefore have more importance than those with nuclei in depositing energy (5) Absorption of energy from a charged particle in biological material may lead to excitation or ionization An illustration of a charge-particle track is given in Figure 2.2 This figure includes excitation events, ionization events, and delta rays. A delta ray is a high-energy electron that has been released from an atom. It may have enough energy

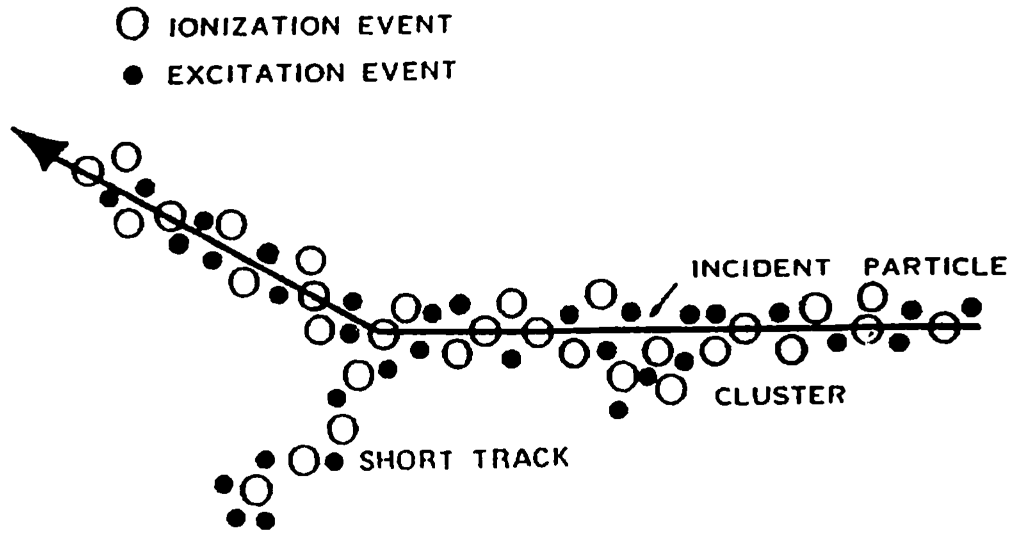

Figure 2.2. Ion path with examples of a cluster and a secondary short track. (7)

to produce its own short path of ionization and excitation. Delta rays are shown in Figure 2.2 as clusters near the incident particle path.

These clusters are also known as the penumbra region. This region is where the secondary electrons are the primary agents of energy dissipation. Although these electrons originate at the center of the core, or incident particle path, they travel along crooked tracks for considerable distances due to multiple scattering events. The tracks compose the "delta ray aura" which has a fuzzy appearance within emulsion in comparison to the solid black central region of the core (9). The radius of the core in water is given by

$$r_c(\mu m) = 0.0116\beta \tag{2.3}$$

where β = v/c, v = particle speed, and c = speed of light. The radius of the outer border of the penumbra in water is given by:

$$r_p(\mu m) = 0.768E - 1.925\sqrt{E} + 1.257 \quad (2\ 4)$$

where E is the kinetic energy of the particle in MeV $nucleon^{-1}$. This formulation of the penumbra radius holds only when E > 2 MeV $nucleon^{-1}$. The radii of the core and the penumbra as a function of particle speed and kinetic energy is given in Table 2.3.

Excitation occurs when the atomic electron obtains enough energy to move to a higher energy orbit without the ejection of an electron. When an electron obtains enough energy to leave the atom and become a free particle, ionization occurs Ionization will only occur if the charged particle has an initial energy high enough to excite the atomic electron to the continuum. This freed electron is a charged particle in motion and can cause other ionizations. The energy disseminated per ionizing event in tissue is about 33 eV, which is enough energy to break a strong chemical bond (6) These two types of collisions are inelastic collisions.

Table 2.3. Radii of core and penumbra for HZE particle tracks in tissue. (9)

Particle speed β = v/c	Kinetic energy (MeV/nucleon)	Core radius r_c (μm)	Penumbra radius r_p (μm)
0.2	19.3	0.0023	7.65
0.3	45.3	0.0035	23.1
0.4	85.4	0.0046	49.1
0.5	145.0	0.0058	89.5
0.6	234.5	0.0070	152.0
0.7	375.5	0.0081	252.0
0.8	625.0	0.0093	433.0
0.9	1214.0	0.0104	867 0
0.95	2066.0	0.0110	1500 0

Secondary electrons, which have been freed by interactions with radiation, become the primary particles in later collisions. These subsequent collisions can produce a variety of ionization products because as the electron energy increases, "the electron ionization process may proceed via different reaction channels" (10). Table 2.4 illustrates the channels for reactions between a diatomic molecule (AB) and an electron. As can be seen by this table, reaction products include: parent, fragment, multiply charged, excited, metastable, and rearrangement ions and ion pairs. A scattered incident electron is noted as e_s, and an ejected secondary electron is noted as e_e. After one of these ionizing events has taken place, it is impossible to distinguish between the scattered and ejected electrons. According to ICRU Report 55, it is customary to call the faster electron the "primary" electron and the slower electron the "secondary" electron (10). The one-step ionization reactions are normally classified as

Table 2.4. Reaction channels between a diatomic molecule and an electron. (10)

$AB + e$	$\rightarrow$	$AB^+ + e_s + e_e$		single ionization
	$\rightarrow$	$AB^{2+} + e_s + 2e_e$		double ionization
	$\rightarrow$	$AB^{z+} + e_s + ze_e$		multiple ionization
	$\rightarrow$	$AB^{K+} + e_s + e_e$		K-shell ionization
	$\rightarrow$	$AB^{**} + e_s$	$\rightarrow$ $AB^+ + e_s + e_e$	autoionization
	$\rightarrow$	$AB^{+*} + e_s + e_e$	$\rightarrow$ $A^+ + B + e_s + e_e$	fragmentation
			$\rightarrow$ $AB^{2+} + e_s + 2e_e$	autoionization
			$\rightarrow$ $AB^+ + e_s + e_e + h\nu$	radiative ionization
	$\rightarrow$	$A^+ + B + e_s + e_e$		dissociative ionization
	$\rightarrow$	$A^+ + B + e_s$		ion pair production
	$\rightarrow$	$AB^* + e_s$		excitation
	$\rightarrow$	AB^{-*}		attachment
	$\rightarrow$	$A^- + B$		dissociative attachment
	$\rightarrow$	$A + B + e_s$		dissociation into neutrals
	$\rightarrow$	$A^* + B + e_s$		dissociation into neutrals

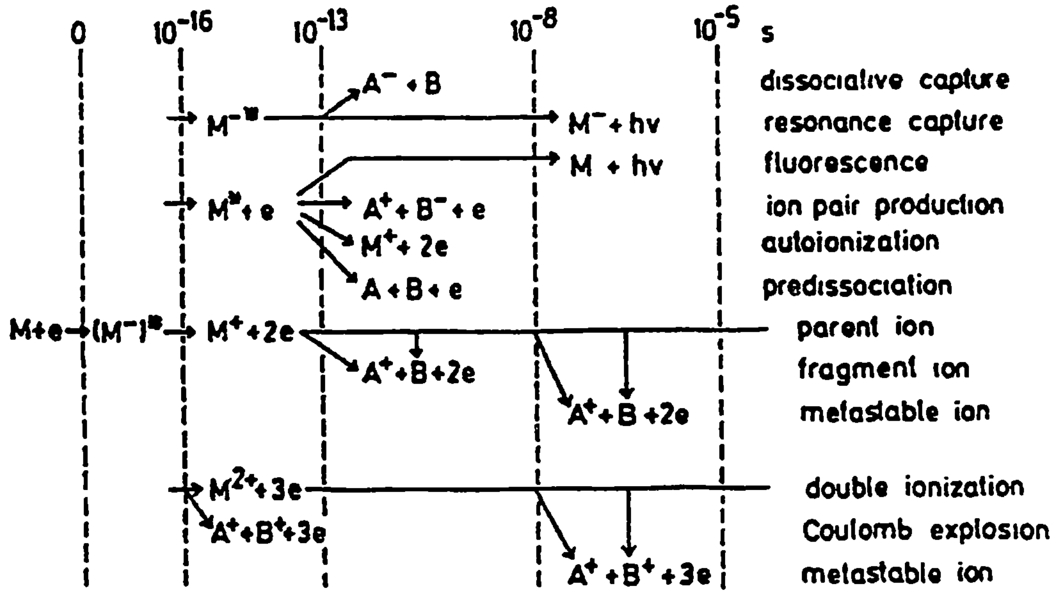

Figure 2.3. Time chart of electron reaction channels. (10)

direct ionization events and occur within 10^{-16} seconds. Figure 2.3 shows a time chart of these electron reaction channels in seconds As the ion moves through a medium, it begins to lose energy and will eventually pick up a free electron.

2.3.2. Stopping Power of Electrons

A charged particle moving through a medium interacts with a large number of atomic electrons. Each of these interactions has a probability of occurrence and probability for a certain energy loss. Stopping power (-dE/dx) is the average expected energy loss per unit distance of travel by a charged particle. Stopping power is LET_∞, or unrestricted LET. The rest of this section deals with an electron as the incoming charged particle.

An incoming electron has the ability to lose all of its energy in a single collision with an atomic electron because the collision involves two particles with the same mass In contrast to heavier charged particles, an incoming electron may lose a large fraction of energy in a single collision and may be easily scattered at large angles. The stopping power due to ionization and excitation for electrons is given by:

$$\frac{dE}{dx}\left(MeV/_{m}\right)=4\pi r_0^2\frac{mc^2}{\beta^2}NZ\left\{\begin{array}{l}\ln\left(\frac{\beta\gamma\sqrt{\gamma-1}}{I}mc^2\right)+\\ \frac{1}{2\gamma^2}\left[\frac{(\gamma-1)^2}{8}+1-(\gamma^2+2\gamma+1)\ln 2\right]\end{array}\right\} \quad (2\ 5)$$

where r_0 = classical electron radius = 2 828x10^{-15} m; mc^2 = 0.511 MeV; $\gamma = (T+Mc^2)/Mc^2$; T = kinetic energy of the particle; M = rest mass of the particle; β = v/c; N = $\rho(N_A/A)$ = number of atoms m^{-3} in the material; ρ = density of the material, N_A = Avogadro's number = 6.022x10^{23} atoms/mol; A = atomic weight of the material, Z = atomic number of the material; and I = mean excitation potential of the material (5). A table of total mass stopping powers (MeV cm^2 g^{-1}) for electrons in muscle-equivalent materials is given in Table 2 5 Several of these materials are used later in this study As a result of the many interactions with atomic electrons, charged particles lose energy nearly continuously and finally stop after traveling a finite distance, called the range.

Table 2.5. Total mass stopping power for electrons in muscle-equivalent materials. (3)

Electron energy MeV	ICRU Tissue MeV cm^2 g^{-1}	Ratio to ICRU Tissue		
		TE[a] Methane Gas	TE[a] Propane Gas	A-150 Plastic
0.010	22.34	1.037	1.045	1.027
0.015	16.31	1.034	1.041	1 025
0.020	13.05	1.032	1.039	1.024
0.030	9.563	1.030	1.037	1.022
0.040	7.705	1.029	1.035	1 021
0.050	6.543	1.028	1.034	1.020
0.060	5.745	1.027	1.033	1.019
0.070	5.161	1.027	1.033	1.019
0.080	4.715	1.026	1.032	1 019
0.100	4.080	1 025	1.031	1.018
0.150	3.211	1.024	1.029	1 017
0.200	2.771	1.023	1.028	1.016
0.300	2.338	1.022	1.027	1 015
0.400	2.134	1.021	1.026	1 015
0.500	2.020	1.021	1.026	1.013
0.600	1.951	1.022	1.027	1.011
0.700	1.907	1.024	1.028	1.009
0.800	1.878	1.026	1.030	1.007
1.00	1.846	1.030	1.034	1.005
1.50	1.832	1.039	1.043	1.002
2.00	1.846	1.048	1.052	0.999
3.00	1.891	1.063	1.066	0.996
4.00	1.936	1.074	1.077	0.994
5.00	1.978	1.084	1.086	0.992
6.00	2.015	1.093	1.095	0.991
7.00	2.053	1.098	1.101	0 988
8.00	2.087	1.104	1.106	0.987
10.00	2.153	1.113	1.114	0 984
15.00	2.303	1.127	1.127	0.978
20.00	2.444	1.134	1.133	0.973
30.00	2.717	1.129	1.122	0.965
40.00	2.984	1.120	1.110	0.957
60.00	3.515	1.100	1.085	0.950
80.00	4.045	1.082	1 064	0.937

[a]TE = Tissue Equivalent

2.3.3. Range of an Electron

Through interactions with atomic electrons or nuclei, charged particles lose kinetic energy. The total distance traveled by a charged particle without respect to direction is the pathlength of the particle. The pathlength is not necessarily a straight path. The pathlength includes the entire distance from the incidence of a charged particle on the medium's surface to the thermalization within the medium. After reaching thermal equilibrium with the medium, the charged particle may diffuse some distance or become absorbed (7). The range is "the thickness of material that just stops the charged particle" (5). For electrons of a certain kinetic energy, the range is less than the pathlength because electrons are easily scattered at large angles after a collision with an atomic electron The following approximates the range per unit density of a particular material for an electron within the energy range from 0.3 keV to 30 MeV·

$$R\left({kg}/{m^2}\right)=a_1\left(\frac{\ln[1+a_2(\gamma-1)]}{a_2}-\frac{a_3(\gamma-1)}{1+a_4(\gamma-1)^{a_5}}\right) \tag{2.6}$$

where $a_1 = 2.335A/Z^{1.209}$; $a_2 = (1.78 \times 10^{-4})Z$; $a_3 = 0.9891 - (3.01 \times 10^{-4})Z$; $a_4 = 1.4687 - (1.180 \times 10^{-2})Z$; $a_5 = 1.232/Z^{0.109}$; and γ, Z, and A are the same as given above for equation 2.5 (5). The range in meters, where the density of the material is ρ, is given by the following:

$$R(m)=\frac{R\left(kg/m^2\right)}{\rho\left(kg/m^3\right)}. \tag{2.7}$$

2.4. PROPORTIONAL COUNTERS

Along with ionization chambers and Geiger-Mueller counters, proportional counters are found in the gas-filled detector category. These detectors operate on the principles of gas ionization and amplification to produce detectable pulses Gas ionization exists when radiation interacts within the detector's sensitive volume with enough energy to eject one or more electrons from neutral gas molecules. This process results in an electron and a positively charged gas molecule, or an ion pair Proportional counters are different from the other detectors in this category because the size of a detectable pulse in a proportional counter is "proportional" to the initial number of electrons produced in the detector.

Under the influence of an applied electric field, the free electrons in the ion pairs drift towards the central anode. If free electrons have a sufficient amount of energy, secondary ionizations may result. This phenomenon is known as gas amplification The number of electrons collected by the anode is much greater than the initial number of electrons that were freed within the chamber. This is called a Townsend avalanche, or electron multiplication. The size of the avalanche at the anode, however, remains proportional to the initial number of ion pairs, or in other words, one ion pair equals one avalanche. For every initial electron produced by the incoming radiation, one hundred to one hundred thousand electrons may reach the anode This amplification factor is low in comparison to Geiger-Mueller counters, which have a gas amplification factor of a billion. This factor keeps the anode from becoming saturated with electrons, which allows for the possibility of energy discrimination between incoming particles (11).

Within the detector volume in a proportional counter, it is important to maintain vacuum conditions and not let air enter from the outside. If oxygen is present within the detector volume, an oxygen molecule may pick up an electron as it migrating toward the anode. However, the oxygen-electron pair will not be able to pick up enough energy to create an avalanche, and therefore, a useable signal will not be produced

Many different types of proportional counters are manufactured: gas flow, air-flow, and tissue equivalent proportional counters, which is the counter of interest in this study.

2.4.1. Tissue Equivalent Proportional Counters

A tissue equivalent proportional counter (TEPC) measures the energy deposition in simulated microscopic volumes of tissue that are approximately 1 μm in diameter. The microscopic volume is equivalent to a homogeneous, soft-tissue medium, i.e. the human cell. Energy is deposited in the volume, either directly or indirectly, in one of three ways:

1. the particle travels through the volume,
2. the particle passes near the volume and one of its secondaries enters the volume, and
3. the particle begins or ends its path within the volume (1).

Figure 2.4 illustrates these three examples of energy deposition. A much larger gas-filled chamber in a TEPC replaces the microscopic volume of the human cell.

Of the above three examples of energy deposition, the first and third are examples of direct events. A direct event describes the situation when the charged particle actually travels, or partially travels, through the volume. When the microscopic

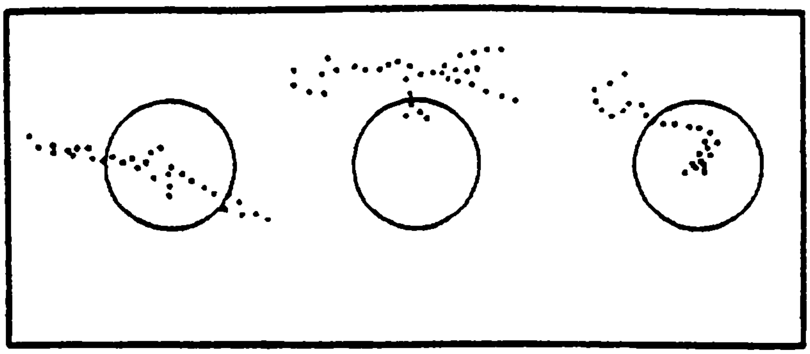

Figure 2.4. Events in small spherical volume elements in irradiated tissue. (1)

volume is replaced by a larger cavity, direct events are not affected The second example describes an indirect event, which is when a charged particle passes outside the volume but introduces one or more delta rays into the volume. However, when the microscopic volume is replaced by the gas-filled cavity, indirect events are greatly influenced. The number of delta rays injected into the cavity is greater than the number in the homogeneous medium (12). Examples of indirect and direct events are shown in Figure 2 5 and 2.6 for a homogeneous medium and a cavity, respectively.

When choosing the type of counter to use in experimental microdosimetry, it is important to look at several criteria. A counter lacking a solid interface around the sensitive volume is the most desirable choice since it closely simulates the uniform medium of a human cell. This is called a wall-less TEPC. However, this type of counter is harder to use. A counter using a tissue equivalent plastic wall to distinguish between the sensitive detector volume and the external surface is extremely convenient. This type of counter is rugged and easy to use. However, the presence of the solid wall distorts the detector results.

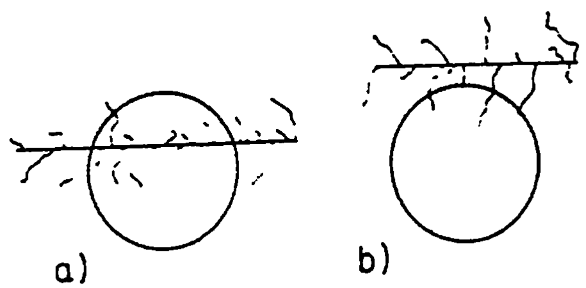

Figure 2.5. Representations of (a) direct and (b) indirect events in a homogeneous medium. (12)

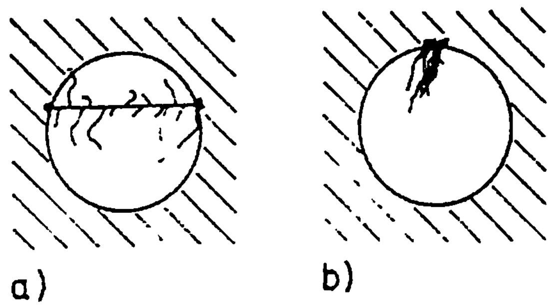

Figure 2.6. Representations of (a) direct and (b) indirect events in a cavity. (12)

The walls and gas used in the solid-wall TEPC are constructed of materials that are similar in atomic composition to human tissue. This is important because interaction cross sections and mass collision stopping powers of charged particles within the TEPC must be exactly the same as tissue in order to observe the appropriate response (3). Although both the walls and the gas simulate human cells or tissue, they respond to radiation differently. Microscopic measurements performed by solid-wall TEPCs exhibit distortions due to wall effects (12)

2.4.2. Wall Effects

Tissue equivalent proportional counters utilize tissue-equivalent walls and tissue equivalent gas to depict human tissue, but the differences between the densities of these two materials causes distortions in the measured spectra. These errors are commonly called "wall effects" The occurrence of wall effects was first described by Failla and Failla (13) and later by Rossi and Kellerer (2). Wall effects primarily occur when a change of density occurs at the boundary of the detector. Because a large, gas-filled volume replaces multiple separate microscopic volumes, the probability of more than one path from the same charged particle entering the detector volume becomes important. Paths that would normally be recorded as separate events in separate sites are now recorded as a large event in one site, thereby creating an error in the final result (14).

When radiation enters the wall, interactions can produce multiple, charged particles. Although only one particle entered the wall, multiple particles can enter the detector volume. Also, a particle leaving the gas is more likely to scatter in the wall and reenter the gas; therefore, the same particle will be counted twice. Because multiple particles enter the region of interest, the initial particle could account for a larger event than would be seen in a uniform medium, or human cell Four types of wall effects commonly occur: delta-ray effect, re-entry effect, V-effect, and scattering effect (3) All four lead to an increase in energy within the detector volume that would not normally occur if the walls and gas were of the same density Figure 2 7 illustrates each of these effects.

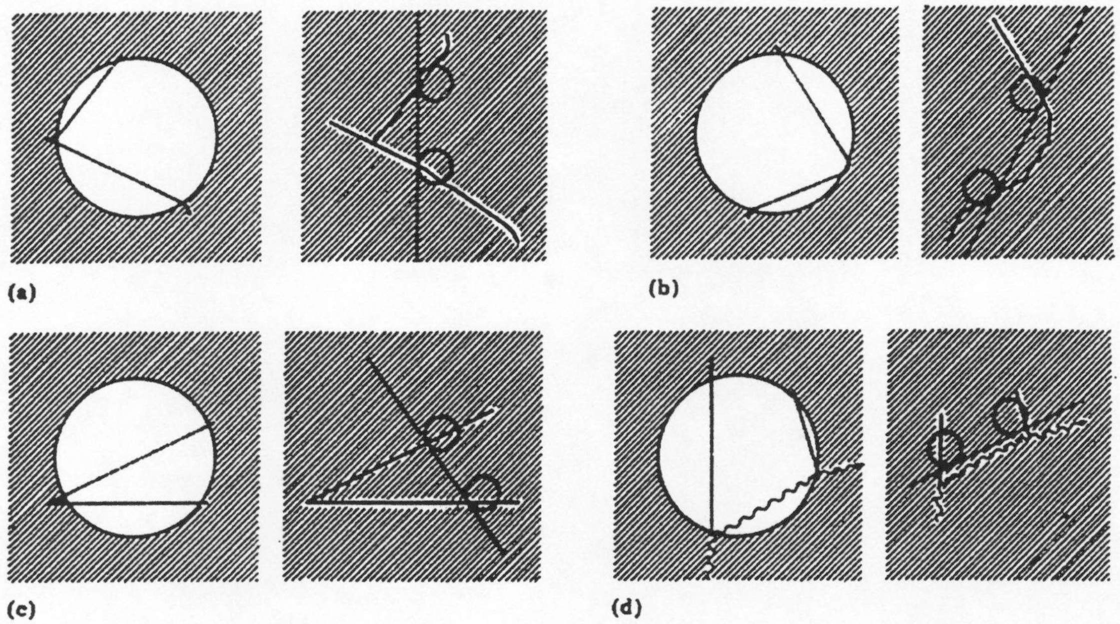

Figure 2.7. Diagrams of the four types of wall effects: (a) delta-ray effect; (b) re-entry effect; (c) V effect; and (d) scattering effect. (3)

Delta-ray effect

When a charged particle passes through the wall and has an interaction, there is a greater chance that multiple delta rays from the wall will enter the gas. This is called the delta-ray effect. The detector sees multiple separate events and counts them each although they are originally from the same event and would actually only contribute to the dose once. This effect is most common when the radiation in question is a high-energy, heavy charged particle or a high-energy electron (11). Figure 2.7(a.) illustrates the delta-ray effect.

Re-entry effect

Within a uniform medium, it is unlikely that the curved path of the electron will reenter the volume where it originated. The re-entry effect occurs when the electron passes out of the detector volume and because of the higher density of the walls, it re-enters the volume due to a bent track. Again, the detector sees and counts two separate events although the two events are actually the same electron that should only be counted once. This effect occurs only for electrons. The re-entry effect is more important for electrons in the energy range from 0.01 MeV to 1 MeV, while the delta-ray effect is more significant for electrons with energy greater than 1 MeV (5) The re-entry effect is illustrated in Figure 2.7(b).

V-effect

The V-effect occurs because of an increase in the number of nuclear collisions that occur within the wall as compared to the uniform medium (4). Figure 2.7(c.) illustrates the V-effect.

Scattering effect

The scattering effect occurs when uncharged primaries produce multiple, charged secondaries that enter the detector volume. This effect is most common for multiple scattering of neutrons and photons (11). Figure 2.7(d) depicts the scattering effect.

2.5. MONTE CARLO METHOD OF ELECTRON TRANSPORT

The Monte Carlo N-Particle (MCNP4B) transport code is used in this study to simulate the transport of electrons within a tissue equivalent proportional counter

MCNP transports electrons by moving the electron in predetermined step lengths depending on the energy of the electron and the composition/density of the material. These steps are long enough to include multiple collisions, but short enough so that a step's mean energy loss is small. At the end of the initial step, a new direction and energy loss are sampled from probability distribution tables derived from multiple-scattering theory and ionization energy loss theory. This is called the "condensed history Monte Carlo method" (15). When the electron energy drops below the cutoff, the track is terminated. Normally the length of the electron step is shorter than the distance to the cell boundary; therefore, MCNP calculates the distance to the nearest point on the cell boundary and then waits until the accumulated step lengths approach this distance.

2.5.1. Energy Loss

According to the MCNP4B manual (15), the energy loss for each step is calculated using an energy loss distribution, $f(s,\Delta)d\Delta$. The energy loss distribution describes the energy loss, Δ, for a particular step length, s, and is given by the following expression:

$$f(s,\Delta)d\Delta = \phi(\lambda)d\lambda \, . \tag{2.8}$$

The universal function of a single-scaled variable, $\phi(\lambda)$, is given by the following·

$$\phi(\lambda)=\frac{1}{2\pi i}\int_{x-i\infty}^{x+i\infty}\exp(\mu\log\mu+\lambda\mu)d\mu \tag{2 9}$$

where x is a positive real number specifying the line of integration The single-scaled variable, λ, is given by:

$$\lambda=\frac{\Delta}{\xi}-\log\left[\frac{2\xi mv^2}{(1-\beta^2)I^2}\right]+\delta+\beta^2-1+\gamma \tag{2.10}$$

where m is the mass of an electron, v is the speed of an electron, δ is the density effect correction, β = v/c, I is the mean excitation energy, γ is Euler's constant, and ξ is given by:

$$\xi=\frac{2\pi e^4 NZ}{mv^2}s \tag{2.11}$$

where e is the electron charge, and NZ is the number density of atomic electrons

2.5.2. Angular Deflection

The angular deflection of an electron is calculated, once per substep, using the following distribution (15):

$$F(s,\mu)=\sum_{j=0}^{\infty}(j+0.5)\exp(-sG_j)P_j(\mu) \tag{2.12}$$

where s is the length of the substep; $\mu = \cos(\theta)$, where θ is the angular deflection from the beginning of the substep; $P_j(\mu)$ is the j^{th} order Legendre polynomial; and G_j is given by the following expression

$$G_j = 2\pi N \int_{-1}^{1} \frac{d\sigma}{d\Omega}\left[1 - P_j(\mu)\right] d\mu \qquad (2\ 13)$$

where N is the atom density of the medium and $d\sigma/d\Omega$ is the microscopic cross-section For electron energies less than 0.256 MeV, the microscopic cross-section is computed using calculations performed by Riley (16). For larger energies, the cross-section is a combination of Mott and Rutherford cross-sections. This factored cross-section is given by:

$$\frac{d\sigma}{d\Omega} = \frac{Z^2 e^2}{p^2 v^2 (1 - \mu - 2\eta)^2}\left[\frac{(d\sigma/d\Omega)_{Mott}}{(d\sigma/d\Omega)_{Rutherford}}\right] \qquad (2.14)$$

where e, p, and v are the charge, momentum, and speed of the electron, respectively, and η is the screening correction. The value of η is given by:

$$\eta = \frac{1}{4}\left(\frac{\alpha mc}{0.885p}\right)^2 Z^{2/3}\left[1.13 + 3.76\left(\frac{\alpha Z}{\beta}\right)^2 \sqrt{\frac{\tau}{\tau + 1}}\right] \qquad (2.15)$$

where τ is the electron energy, $\beta = v/c$, α is the fine structure constant, and m is the rest mass of the electron.

3. METHODOLOGY

Modeling of the tissue equivalent proportional counter by MCNP4B was performed on a 160 MB Ultra 140 UNIX workstation maintained by the College of Engineering at the University of Tennessee. The MCNP input file used in this study is given in Figure 3.1. Unless otherwise noted, all references in this section to an MCNP input file will correspond to Figure 3.1. Other examples of input files, which were used in this study, are given in Appendix B. This section will look at the basic design of the tissue equivalent proportional counter and the MCNP model used in this study.

3.1. TISSUE EQUIVALENT PROPORTIONAL COUNTER DESIGN

The proportional counter modeled in the MCNP input file represents a spherical TEPC used by S.E. Rademacher et al (4). Lines 2 through 5 of the input file model the counter (internal gas cavity, A-150 plastic wall, aluminum shell, and stainless-steel 316 anode and helix). The internal gas cavity with a radius of 0.635 cm contains a propane-based tissue equivalent gas. The counter walls are composed of A-150 muscle equivalent plastic with a thickness of 0.127 cm. The stainless-steel 316 anode wire is surrounded by a stainless-steel 316 helix (0.05 cm radius). An electrical potential is created between the anode and helix that produces an electric field along the length of the anode. In other words, the anode/helix combination is the collecting electrode. A thin layer of aluminum (0.0018 cm thick) encases the entire configuration in order to maintain vacuum conditions. The above TEPC design is illustrated in Figure 3.2

```
Setup of tissue equivalent proportional counter to study wall effects
1 1 -7.87E-5          -1  4      IMP:E=1        $ propane gas (ICRU 36)
2 2 -1 1018            1 -2 4    IMP E=1        $ A-150 plastic wall (ICRU 36)
3 3 -2.702             2 -3 4    IMP E=1        $ aluminum shell
4 4 -7.861            -4 -3      IMP E=1        $ stainless steel 316 anode and helix
5 0                    3         IMP:E=0

c blank line above
c surface cards
c
1 SO         0.635               $ internal gas cavity (sphere radius is 6 35 mm)
2 SO         0 762               $ A-150 wall (sphere radius is 7.62 mm)
3 SO         0 7638              $ aluminum shell (sphere radius is 7.638 mm)
4 CZ         0 05                $ stainless steel 316 anode/helix (cylinder radius is 0 5 mm)

c blank line above
c source card – 250 MeV iron beam (arbitrary beam)
c Source has the energy distribution given in the SI1 and SP1 cards, is located on
c        surface 2, and has a normal of –1 (inward normal)
c
MODE E
SDEF ERG=D1 SUR=2 NRM=-1
SI1 H     1 0E-3 1 2E-3 1 4E-3 1.6E-3 1 8E-3 2.0E-3 2.2E-3 2 4E-3 2 6E-3 2.8E-3 3 0E-3 3 2E-3
          3 4E-3 3 6E-3 3.8E-3 4.0E-3 4.2E-3 4 4E-3 4 6E-3 4 8E-3 5 0E-3 5.5E-3 6.0E-3 6 5E-3
          7.0E-3 7 5E-3 8.0E-3 8 5E-3 9 0E-3 9.5E-3 1.0E-2 1.1E-2 1.2E-2 1.3E-2 1 4E-2 1 5E-2
          1.6E-2 1 7E-2 1 8E-2 1 9E-2 2 0E-2 2 1E-2 2.2E-2 2.3E-2 2.4E-2 2 5E-2 2.6E-2 2.7E-2
          2 8E-2 2.9E-2 3.0E-2 3.1E-2 3 2E-2 3.3E-2 3 4E-2 3 5E-2 3 6E-2 3.7E-2 3 8E-2 3.9E-2
          4 0E-2 4.1E-2 4 2E-2 4.3E-2 4.4E-2 4.5E-2 4 6E-2 4.7E-2 4 8E-2 4 9E-2 5.0E-2 5 5E-2
          6 0E-2 6 5E-2 7 0E-2 7.5E-2 8.0E-2 8.5E-2 9 0E-2 9 5E-2 1.0E-1 1.1E-1 1 2E-1 1.3E-1
          1 4E-1 1.5E-1 1.6E-1 1.7E-1 1.8E-1 1.9E-1 2.0E-1 2.1E-1 2 2E-1 2.3E-1 2.4E-1 2.5E-1
          2.6E-1 2 7E-1 2 8E-1 2.9E-1 3.0E-1 3.1E-1 3.2E-1 3.3E-1 3.4E-1 3.5E-1 3.6E-1 3 7E-1
          3.8E-1 3 9E-1 4 0E-1 4.1E-1 4.2E-1 4 3E-1 4.4E-1 4.5E-1 4.6E-1 4.7E-1 4.8E-1 4.9E-1
          5.0E-1 5 5E-1 6.0E-1 6.5E-1 7.0E-1 7.5E-1 8.0E-1 8.5E-1 9.0E-1 9.5E-1 1.0
SP1 D     0 1.2908E-1 9.6122E-2 7.4700E-2 5.9932E-2 4.9284E-2 4.1334E-2 3.5229E-2
          3.0429E-2 2.6583E-2 2.3448E-2 2 0858E-2 1.8690E-2 1.6856E-2 1.5290E-2 1.3941E-2
          1.2770E-2 1.1746E-2 1.0846E-2 1.0049E-2 9 3407E-3 2 0722E-2 1.7661E-2 1.5255E-2
          1.3326E-2 1.1755E-2 1.0456E-2 9.3697E-3 8.4504E-3 7.6653E-3 6.9889E-3 1 2290E-2
          1.0475E-2 9.0479E-3 7.9042E-3 6 9722E-3 6.2019E-3 5 5574E-3 5.0121E-3 4 5465E-3
          4.1453E-3 3.7970E-3 3.4926E-3 3 2249E-3 2 9880E-3 2.7774E-3 2.5891E-3 2.4202E-3
          2 2679E-3 2 1302E-3 2 0052E-3 1.8913E-3 1 7872E-3 1.6919E-3 1.6043E-3 1.5236E-3
          1 4492E-3 1.3803E-3 1.3163E-3 1 2570E-3 1.2017E-3 1.1501E-3 1.1020E-3 1.0569E-3
          1.0147E-3 9 7501E-4 9.3774E-4 9.0266E-4 8.6960E-4 8.3840E-4 8.0892E-4 3.6544E-3
          3.1146E-3 2.6903E-3 2 3502E-3 2.0731E-3 1.8441E-3 1.6524E-3 1.4903E-3 1 3519E-3
          1.2326E-3 2 1675E-3 1.8474E-3 1.5957E-3 1 3940E-3 1.2296E-3 1.0938E-3 9.8010E-4
          8.8394E-4 8.0181E-4 7.3106E-4 6.6965E-4 6.1596E-4 5.6874E-4 5.2697E-4 4 8982E-4
          4.5662E-4 4 2683E-4 3.9997E-4 3.7568E-4 3 5363E-4 3 3355E-4 3 1520E-4 2.9838E-4
          2.8294E-4 2.6871E-4 2.5558E-4 2.4342E-4 2.3215E-4 2.2168E-4 2.1193E-4 2.0284E-4
          1 9434E-4 1.8640E-4 1.7895E-4 1.7195E-4 1 6538E-4 1.5919E-4 1.5336E-4 1 4786E-4
          1.4266E-4 6 4450E-4 5.4930E-4 4.7446E-4 4 1449E-4 3 6562E-4 3 2523E-4 2 9143E-4
          2.6283E-4 2 3841E-4 2 1738E-4
```

Figure 3.1. MCNP input file for a 250 MeV nucleon^{-1} iron beam on a solid-wall TEPC – determination of the particle flux in the propane gas.

```
c
c matenal cards
c
M1      1000.    -0 103      $ hydrogen in propane gas (ICRU36)
        6000     -0 569      $ carbon
        7000     -0.035      $ nitrogen
        8000     -0 293      $ oxygen
M2      1000.    -0.1015     $ hydrogen ın A-150 plastic wall (ICRU36)
        6000     -0 7765     $ carbon
        7000.    -0.035      $ nitrogen
        8000.    -0 052      $ oxygen
        9000.    -0.017      $ fluorine
        20000    -0.018      $ calcium
M3      13000.   -1          $ aluminum ın shell (CRC handbook)
M4      24000.   -0.16       $ chromium in stainless-steel 316 (web pages)
        28000.   -0.10       $ nickel
        6000.    -0.0008     $ carbon
        25000    -0.02       $ manganese
        14000.   -0.01       $ silicon
        15000    -0.00045    $ phosphorus
        16000.   -0 0003     $ sulfur
        26000    -0.68845    $ iron
        42000.   -0 02       $ molybdenum
c
c tally cards
c
F4 E 1  $ flux averaged over cell 1 (particles/cm2/source electron)
E4        1.2908E-1 9 6122E-2 7.4700E-2 5.9932E-2 4.9284E-2 4 1334E-2 3 5229E-2 3 0429E-2
          2.6583E-2 2.3448E-2 2.0858E-2 1.8690E-2 1.6856E-2 1.5290E-2 1 3941E-2 1 2770E-2
          1.1746E-2 1.0846E-2 1.0049E-2 9.3407E-3 2.0722E-2 1.7661E-2 1.5255E-2 1.3326E-2
          1.1755E-2 1 0456E-2 9.3697E-3 8 4504E-3 7.6653E-3 6 9889E-3 1 2290E-2 1.0475E-2
          9.0479E-3 7.9042E-3 6 9722E-3 6 2019E-3 5.5574E-3 5 0121E-3 4.5465E-3 4.1453E-3
          3 7970E-3 3.4926E-3 3 2249E-3 2.9880E-3 2.7774E-3 2.5891E-3 2 4202E-3 2 2679E-3
          2.1302E-3 2.0052E-3 1.8913E-3 1 7872E-3 1 6919E-3 1.6043E-3 1 5236E-3 1.4492E-3
          1.3803E-3 1.3163E-3 1.2570E-3 1.2017E-3 1.1501E-3 1.1020E-3 1.0569E-3 1 0147E-3
          9.7501E-4 9.3774E-4 9.0266E-4 8.6960E-4 8 3840E-4 8 0892E-4 3 6544E-3 3.1146E-3
          2 6903E-3 2.3502E-3 2 0731E-3 1.8441E-3 1.6524E-3 1 4903E-3 1.3519E-3 1 2326E-3
          2.1675E-3 1 8474E-3 1.5957E-3 1.3940E-3 1 2296E-3 1.0938E-3 9 8010E-4 8.8394E-4
          8.0181E-4 7.3106E-4 6.6965E-4 6.1596E-4 5.6874E-4 5.2697E-4 4.8982E-4 4 5662E-4
          4 2683E-4 3 9997E-4 3 7568E-4 3.5363E-4 3 3355E-4 3 1520E-4 2.9838E-4 2 8294E-4
          2.6871E-4 2.5558E-4 2.4342E-4 2 3215E-4 2 2168E-4 2.1193E-4 2 0284E-4 1 9434E-4
          1.8640E-4 1.7895E-4 1.7195E-4 1 6538E-4 1.5919E-4 1.5336E-4 1 4786E-4 1.4266E-4
          6.4450E-4 5.4930E-4 4.7446E-4 4.1449E-4 3.6562E-4 3 2523E-4 2 9143E-4 2 6283E-4
          2.3841E-4 2 1738E-4
c
c cutoff card after a million histones
c
NPS 1000000
PRINT
```

Figure 3.1. (continued)

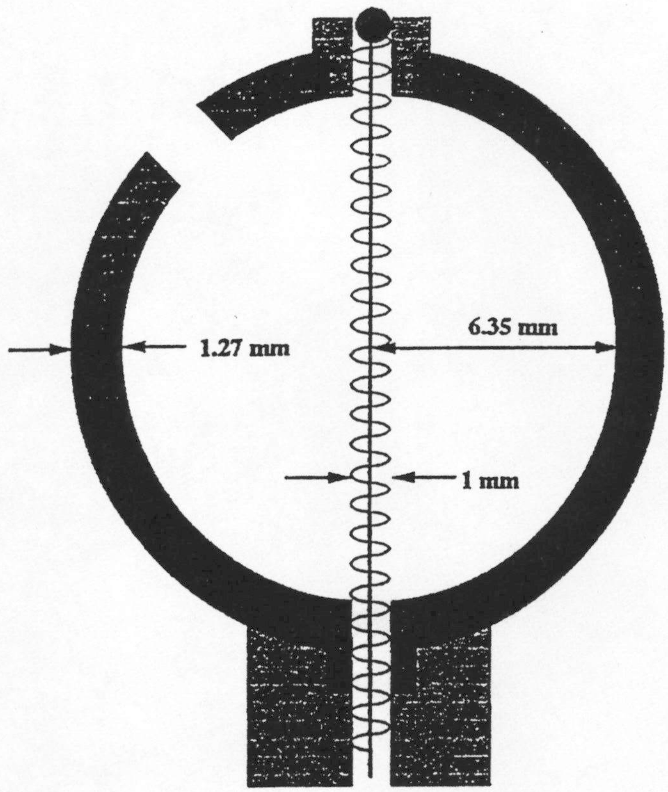

Figure 3.2. Diagram of a spherical TEPC. (4)

A few differences exist between the MCNP model and an actual TEPC. One difference is that the gas inlet and outlet regions are not included in the MCNP model. Also, the helix and central anode wire have been simplified. The two separate pieces are combined into one cylinder with the same radius as the original helix in the actual TEPC model. These deletions simplify the MCNP model geometry. The differences between the MCNP model and actual TEPC are not expected to significantly change the results of the study.

A second TEPC design was also modeled using MCNP. The second design is identical to the design described above, except the A-150 wall and aluminum shell have been excluded. This design is used to simulate the wall-less TEPC. Although in reality, the propane-based tissue equivalent gas has some type of shell to contain the gas, this design seeks to look at the interactions of the electrons only with the gas.

3.2. MCNP MODEL

To model the wall effects of the TEPC, the source is placed on the inner surface of the A-150 spherical walls, the outer surface of the wall, and the outer surface of the gas in the wall-less design. The configuration used to create the MCNP input for all materials in the solid-wall TEPC is illustrated in Figure 3.3 As shown in this figure, the configuration also includes a void region, or cell 5 (line 6 of the input file), which is beyond the outer surface of the aluminum casing, or beyond the outer surface of the gas in the case of the wall-less design. This ensures that particles that escape from the TEPC will be "killed." The inclusion of a void enables the computer run time, which would normally be used to chase these escaping particles, to be greatly reduced without degrading the results A second figure, Figure 3.4, shows the configuration used to create the MCNP input for the wall-less TEPC design.

3.2.1. Material Composition

The following sections discuss the elemental and chemical compositions of each of the materials modeled in this study: propane-based tissue equivalent gas, A-150 plastic wall, aluminum shell, and stainless-steel 316 anode wire and helix.

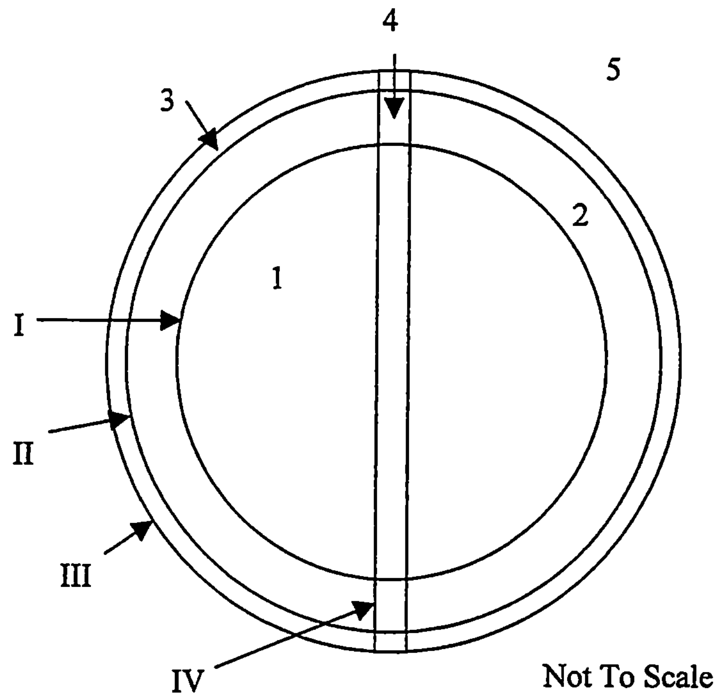

Cell 1 -- propane-based tissue-equivalent gas
Cell 2 -- A-150 tissue-equivalent plastic
Cell 3 -- aluminum shell
Cell 4 -- stainless-steel 316 anode/helix
Cell 5 -- void region outside TEPC

Surface I -- sphere with radius 0.635 cm
Surface II -- sphere with radius 0.762 cm
Surface III -- sphere with radius 0.7638 cm
Surface IV -- cylinder with radius 0.05 cm

Figure 3.3. MCNP configuration used for the solid-wall TEPC.

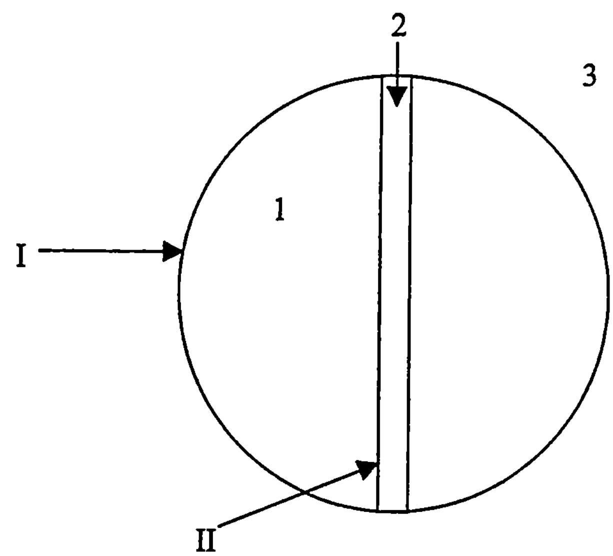

Not To Scale

Cell 1 -- propane-based tissue-equivalent gas
Cell 2 -- stainless-steel 316 anode/helix
Cell 3 -- void region outside TEPC

Surface I -- sphere with radius 0.635 cm
Surface II -- cylinder with radius 0.05 cm

Figure 3.4. MCNP configuration used for the wall-less TEPC.

Propane-Based Tissue Equivalent Gas

Two types of gases are commonly used in the design of a TEPC Although both are muscle equivalent gases, they are different in elemental composition; therefore, the choice of the gas material includes important criteria. These criteria include the similarity of the gas to tissue, homogeneity to A-150 plastic, and quality as a counter. Since neither gas meets all three criteria, the best gas to select is the one that meets the most criteria. For example, according to ICRU Report 36, the methane-based gas is closer to tissue in oxygen and carbon content, while the propane-based gas is more homogeneous with the A-150 plastic walls. Also, a higher gas gain is achievable with the propane-based gas (3). Since the propane-based gas is more homogeneous to the A-150 plastic wall, it was chosen for this study.

Propane-based tissue equivalent gas is a mixture of CO_2, N_2, C_3H_8 and a small quantity of isobutane. Mass fractions of these compounds are, respectively: 0.3939, 0.0564, 0.5485, and 0.0012. The density of the gas is 7.87×10^{-5} g cm^{-3}, which is equivalent to 1×10^{-6} g cm^{-2} in tissue (4). Table 3.1 gives the elemental compositions in percent by weight of the two gases and the ICRU muscle tissue. These chemical compositions are defined for the propane-based gas in lines 54 to 57 of the input file illustrated in Figure 3.1.

A-150 Wall Composition

The walls of the TEPC are composed of A-150 tissue equivalent plastic. This plastic is considered to be muscle equivalent. Francis Shonka and collaborators developed A-150 plastic (17). The chemical formula for A-150 plastic is $C_{471}H_{896}O_{81}N_{62}$. The elemental composition of A-150 plastic and ICRU muscle tissue in percent by

Table 3.1. Elemental composition of tissue equivalent materials in weight percent. (3)

	H	C	N	O	F	Na	Mg	P	S	K	Ca
ICRU muscle tissue	10.2	12.3	3.5	72.9	-	0 08	0 02	0.2	0.5	0 3	0 007
A-150 plastic	10.1	77.6	3.5	5.2	1.7	-	-	-	-	-	1 8
Methane-based gas	10.2	45.6	3.5	40.7	-	-	-	-	-	-	-
Propane-based gas	10.3	56.7	3.5	29.3	-	-	-	-	-	-	-

weight is given in Table 3 1. In the comparison between these two materials, it can be seen that they are similar in composition except for the carbon and oxygen percentages. According to ICRU Report 36, carbon is substituted for oxygen in the plastic because the concentration of oxygen found in tissue is not realistically found in an actual solid, and because a larger amount of carbon in the plastic is needed to provide better electrical conductivity (3).

A-150 tissue equivalent plastic is a homogeneous mixture of polyethylene ($(C_2H_4)_n$), nylon (Zytel 69), carbon and calcium fluoride (CaF_2) The weight percents of these compounds are 45.14%, 35.22%, 16.06%, and 3.58%, respectively (17). The density of the plastic wall is 1.1018 g cm^{-3} which is 14,000 times greater than the density of the propane-based tissue equivalent gas (4). These chemical compositions are defined for the A-150 plastic in lines 58 through 63 of the input file illustrated in Figure 3.1.

Aluminum Shell

The outer shell of the TEPC is composed of pure aluminum and is used to help maintain a vacuum within the counter. The density of aluminum is 2.702 g cm^{-3}, as found in the CRC Handbook of Chemistry and Physics (18). Pure aluminum is defined on line 64 in the input file (Figure 3.1).

Stainless-Steel 316

The central anode wire and helix are composed of stainless-steel 316, which is one of the more common of the stainless steels. The density of stainless-steel 316 is 7.861 g cm^{-3} (19). Stainless-steel 316 is a mixture of chromium, nickel, carbon, manganese, silicon, phosphorus, sulfur, iron and molybdenum. The weight percents of these elements are, respectively: 16%, 10%, 0.08%, 2%, 1%, 0.045%, 0.03%, 68.845%, and 2%. When a range of weight percents is given for an element (Cr, Ni, and Mo), the minimum value was chosen for this study (20). The chemical compositions are defined for stainless-steel 316 in lines 65 through 73 of the input file (Figure 3.1).

3.2.2. Electron Cross-Sections

The elemental identifiers given in lines 54 through 73 of the MCNP input file describe the different elements that comprise the four materials. The single electron interaction data library within MCNP only contains data on an element-by-element basis There is no distinction between isotopes for the elements. The energy range of the electron cross-section tables is from 1 keV to 1000 MeV However, because the energy range for photons is limited at the upper end to 100 MeV, electrons are also limited to 100 MeV. The library contains data that can be used to calculate electron stopping powers and ranges.

3.2.3. Source Description

The electron source is a spherical surface source located at one of two locations within the TEPC and at one location within the wall-less TEPC One of the two locations within the sold-wall TEPC is on the interior surface of the A-150 plastic wall. The source was positioned on this surface to represent the delta rays that enter the gas from the wall. The electron source is also positioned on the exterior surface of the A-150 plastic wall. This position represents the electrons that have been generated by the initial ion beam on the outside of the wall. In the case of the wall-less design, the electron source is a spherical source located on the exterior surface of the propane-based tissue equivalent gas Each source electron is sampled uniformly from the surface from a defined energy bin. Bin boundaries (SI1 H) and bin probabilities (SP D) describe the continuous energy distribution, which is depicted in the input The initial direction of the electron's flight is designated inwardly ("NRM=-1", line 22 of MCNP input) for the case in which the positive normal of a spherical surface is assumed to be directed outward. The position of the particle is sampled uniformly in area from the spherical surface. The source description is given on lines 21 through 50 of the input file shown in Figure 3.1. A further explanation of the determination of the secondary electron source is given in Section 3.3, later in this study

3.2.4. Tallies

Lines 77 through 94 define one of the two tallies of interest for this study The first tally is the track length estimate of the cell flux. The format "F4:E 1" (line 77 of the input file) specifies the electron flux averaged over cell one in particles per square centimeter. The format "E4 1.0E-3 ... 1.0E+0" (lines 78 through 94) describes the upper bounds of the energy bins where the tally results are displayed. The scoring for the F4 tally is the particle weight multiplied by the track length and divided by the cell volume. The second tally used in this study is the energy deposition tally in a cell in units of MeV. This tally is designated by "*F8:E 2", which specifies the energy deposited in cell two. The energy bins are not used for this tally. The scoring for the *F8 tally is the source weight multiplied by the particle energy. Both tallies are normalized per source electron after the scoring process.

3.2.5. Termination of MCNP Run

The input file shown in Figure 3.1 was terminated after 1,000,000 histories were evaluated (line 98 – "NPS 1000000"). A general rule of thumb is that as the source energy range and the geometry increases, the number of histories required to achieve statistically significant results also increases. For the case of the electron source placed on the outside of the A-150 plastic (surface 2) and the tally in the propane gas (cell 1), the MCNP run was terminated after 2,000,000 histories. For the MCNP inputs that involved the *F8 tally, the MCNP run was terminated after 500,000 histories.

3.2.6. Application of Variance Reduction Techniques

Splitting and Russian roulette variance reduction techniques as a function of input geometry are used in all cells These techniques are executed by "IMP:E=1" in all cells except cell 5. Cell five represents the region outside the detector that was shown in Figure 3.2. Electrons that exit the detector and have interactions outside the entire detector volume are not of interest to the detector response For this reason, the region outside the aluminum shell (cell 5) is given an importance of zero ("IMP.E=0") so that all electrons that enter this cell are immediately killed. A track will split from one cell to the next cell based on the number given after the IMP designation. If the track splits in half, each new track will receive half the weight of the original track. If a track moves in the opposite cell direction, half the cases will be terminated with the remaining half having twice the weight.

3.3. DETERMINATION OF THE ELECTRON SOURCE

The electron source used in the MCNP input file was based on the Rudd model The model is described in this section along with verification for the use of water instead of A-150 tissue equivalent plastic or propane-based tissue equivalent gas in this model.

3.3.1. Rudd Model

The Rudd model, developed by M.E Rudd, was devised to fit data for the singly differential cross-section (SDCS), or $\sigma(\varepsilon)$. The SDCS has units of area per unit energy and is obtained by integrating the doubly differential cross-section over all emission directions. The SDCS describes the energy spectrum of all secondary electrons regardless of ejection direction. The following model is a combination of many other methods in order to make accurate measurements at high impact energies, which are those where the projectile velocity is much greater than the orbital electron velocity

The Rudd model is based on the binary encounter approximation, the Born approximation at high energies, and the molecular promotion mechanism by Rudd (21) and fits well for all energies. The Rudd model was first created to describe the collision of protons with atoms and/or molecules; therefore the following equations only fit this case and will later be generalized to other incoming bare nuclei The Rudd model is based on theory, but it requires a set of parameters that have been determined by fitting experimental data (10).

The SDCS is given in terms of two dimensionless variables, the reduced secondary energy

$$w = \varepsilon / B \tag{3.1}$$

and the reduced projectile velocity,

$$v = (T/B)^{0.5} \tag{3.2}$$

where ε is the energy of the ejected secondary electron, B is the binding energy of electrons in a subshell, and T is the kinetic energy of the electron with the same velocity as the incident particle. The SDCS is given by:

$$\sigma(\varepsilon) = \frac{S}{B} \frac{F_1 + F_2 w}{(1+w)^3 \{1 + \exp[\alpha(w - w_c)/v]\}} \tag{3.3}$$

where the kinematic cutoff energy is:

$$w_c = 4v^2 - 2v - R/4B \tag{3.4}$$

and

$$S = 4\pi a_0^2 N(R/B)^2 \qquad (3.5)$$

where R = Rydberg energy = 13.6 eV, a_0 = Bohr radius = 5 29x10^{-11} m, N is the number of electrons in the target molecule, and F_1, F_2, and α are adjustable fitting parameters Equation 3.3 is useful when w >> w_c In this form the exponential dominates the cross section. When w << w_c, the following form of the SDCS is used (22):

$$\sigma(\varepsilon) = \frac{S}{B}\frac{F_1 + F_2 w}{(1+w)^3}. \qquad (3.6)$$

With the three adjustable parameters, the possibility exists to fit all SDCS's for a single proton energy at all electron energies. When more than one subshell exists, the partial cross sections with the binding energies for each subshell are calculated separately and then summed:

$$\sigma(\varepsilon) = \sum_i \frac{S_i}{B_i} \frac{F_{1i} + F_{2i} w_i}{(1+w_i)^3 \{1 + \exp[\alpha_i (w_i - w_{ci})/v_i]\}} \qquad (3\ 7)$$

where all variables are the same as for equation 3.3, except they are for the i^{th} subshell. The electrons positioned in the outermost subshell are the least tightly bound, and therefore dominate the SDCS However, at higher electron energies, the inner subshells become important (22). Table 3.2 gives the binding energy and number of electrons for water.

Table 3.2. Binding energies in eV (B) and occupation numbers (N) of water. (21)

Orbital	B	N
01s	540	2
$1a_1$	32.2	2
$1b_2$	18 4	2
$2a_1$	14.7	2
$1b_1$	12.6	2

The fitting parameter, α, is independent of initial energy, but is dependent on target material. The other two fitting parameters, F1 and F2, vary with initial energy and target material. These parameters are given by:

$$F_1(v) = L_1 + H_1 \tag{3 8}$$

and

$$F_2(v) = L_2 H_2 / (L_2 + H_2) \tag{3.9}$$

where

$$L_1(v) = C_1 v^{D_1} / \left[1 + E_1 v^{(D_1+4)}\right], \tag{3.10}$$

$$H_1(v) = A_1 \ln(1 + v^2) / (v^2 + B_1/v^2), \tag{3.11}$$

$$L_2 = C_2 v^{D_2}, \tag{3 12}$$

$$H_2 = A_2/v^2 + B_2/v^4 . \tag{3 13}$$

The values of $A_1,\ldots,E_1,A_2,\ldots,D_2$, and α are 0.97, 8.2, 0 4, -0 3, 0 38, 1.04, 17.3, 0.76, 0.04, 0.64, respectively for water.

The above Rudd model does not include Auger or autoionization electrons It also does not include contribution from electron capture, which would create a peak in the cross section where the electron velocity is equivalent to the proton velocity (22) The above model was initially developed for proton impact on particular target materials; however, it can be used for other bare ion projectiles. Multiplying the SDCS by Z^2 makes this modification, where Z is the atomic number of the projectile (10).

The Rudd model can also be implemented for electron impact on a target material. The above model becomes more simplified in comparison to the proton impact model because the exponential factor in the denominator, which arises from the molecular promotion mechanism, is not included (21) The electron impact model is given by:

$$\sigma(\varepsilon)=\frac{S}{B}\frac{[F_1+F_2(1+w)]}{(1+w)^2}. \tag{3 14}$$

For this version of the model, the fitting parameters (F_1 and F_2) are a little different and are only based on A_1, A_2, B_1 and B_2. The fitting parameters are given by:

$$F_1=A_1\left(1-e^{-B_1 t}\right)\ln(t)/t \tag{3 15}$$

and

$$F_2=A_2/(t+B_2) \tag{3.16}$$

where the reduced primary energy is.

$$t = T/B. \tag{3.17}$$

Water has been chosen to approximate the A-150 tissue equivalent plastic and the propane-based tissue equivalent gas for use in the Rudd model. The following section will discuss this approximation in more detail.

3.3.2. Comparison of Water to TEPC materials

Water was used in the above Rudd model to determine the SDCS because it is one of ten targets with previously calculated experimental values (10) Because water is an important constituent of biological cells, it can easily be compared to tissue, or in the case of a TEPC, A-150 tissue equivalent plastic and propane-based tissue equivalent gas. This comparison is illustrated in Figure 3.5 and 3.6, and includes the two TEPC materials, liquid water, and ICRU striated muscle These figures show collisional stopping power as a function of energy (Figure 3.5) and range as a function of energy (Figure 3.6) (23). As can be seen by these figures, water approximates the other three materials extremely well, except for the propane-based gas at very high energies. Even this discrepancy does not cause large errors in the determination of the SDCS.

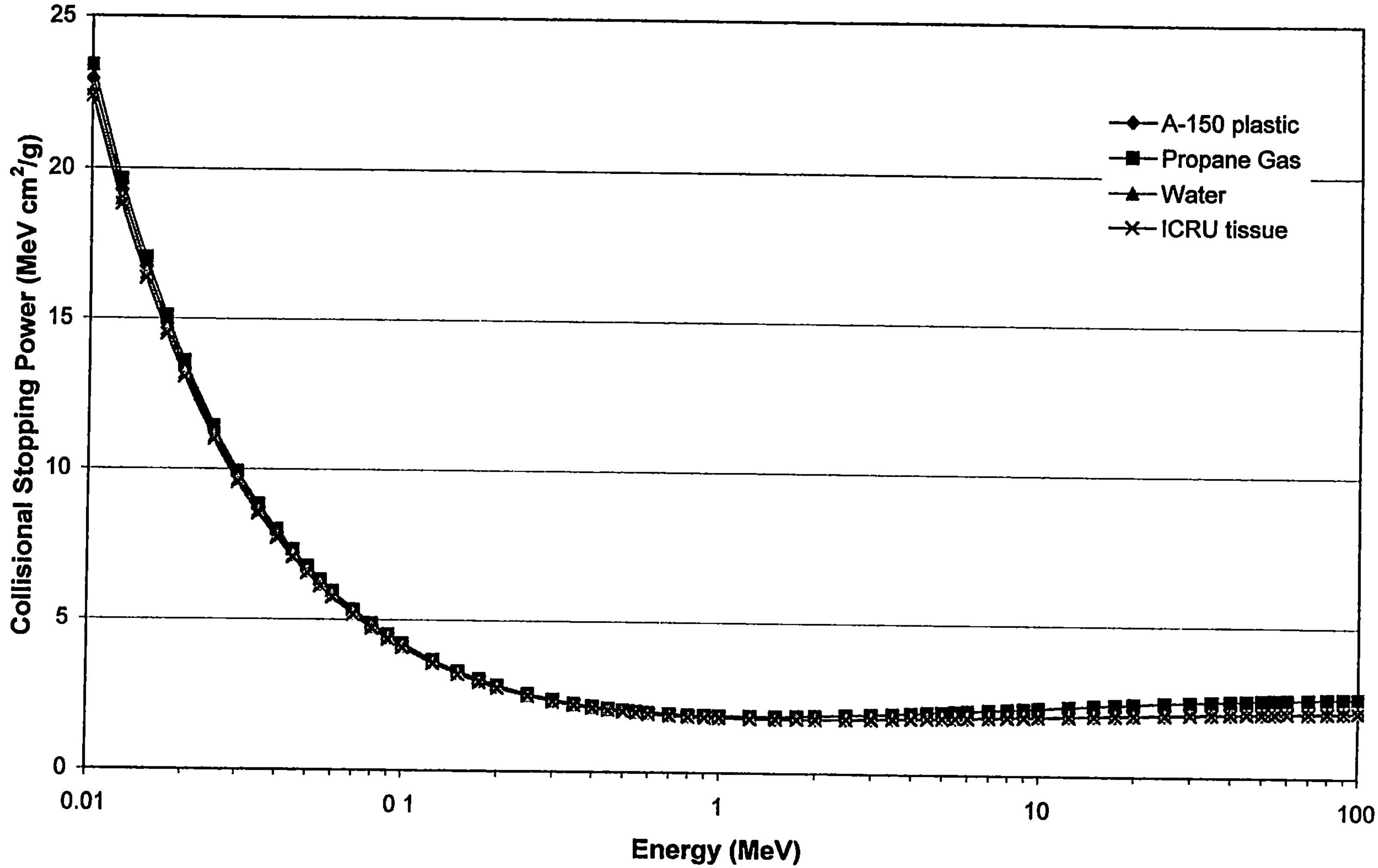

Figure 3.5. Energy versus collisional stopping power. Comparison of water, A-150 plastic, propane-based tissue equivalent gas, and ICRU tissue.

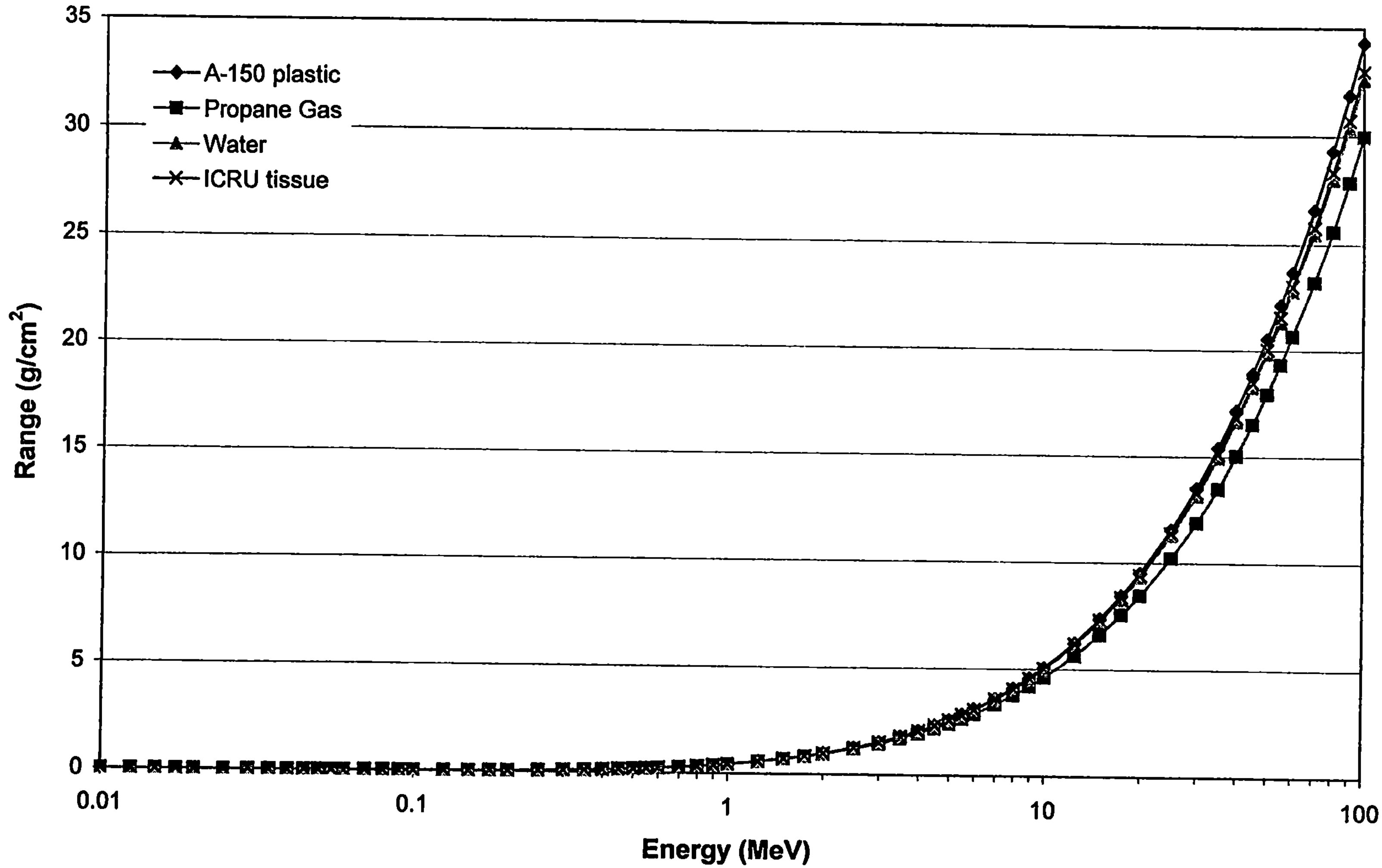

Figure 3.6. Energy versus range. Comparison of water, A-150 plastic, propane-based tissue equivalent gas, and ICRU tissue.

3.4. DATA COLLECTION

This section is divided into two sections The first section deals with the general implementation of the data collection, and the second section deals with the statistical interpretation of the collected data

3.4.1. General Implementation

For each of the two different beams selected for this study, forty-six MCNP runs were performed utilizing the previously mentioned TEPC design. Of these forty-six runs, seven provided flux results for various source and tally locations and the remaining provided energy deposition results for various impact parameter locations for both the solid-wall and the wall-less TEPCs.

The secondary electron source used for this study is based on the impact of one of two different beams on water. The first of these two beams, the 1050 MeV nucleon^{-1} iron beam, was chosen to facilitate a comparison with experimental work done by S.E Rademacher et al (4). Figure 3.7 illustrates the energy distribution of the secondary electrons, determined by the aforementioned Rudd model, from the impact of the iron beam on the water target. The SDCS was multiplied by the number density of water to yield units of particles cm^{-1} eV^{-1}. The power trend-line ($y = 14326x^{-1\ 8153}$), also shown in Figure 3.7, was integrated between energy points to generate a continuous distribution of energies and probabilities for the MCNP input.

The other beam, a 250 MeV nucleon^{-1} iron beam, was chosen in order to facilitate a comparison in the future with experimental work with TEPCs performed at the HIMAC facility in Japan by Dr. Thomas Borak. Figure 3 8 illustrates the energy

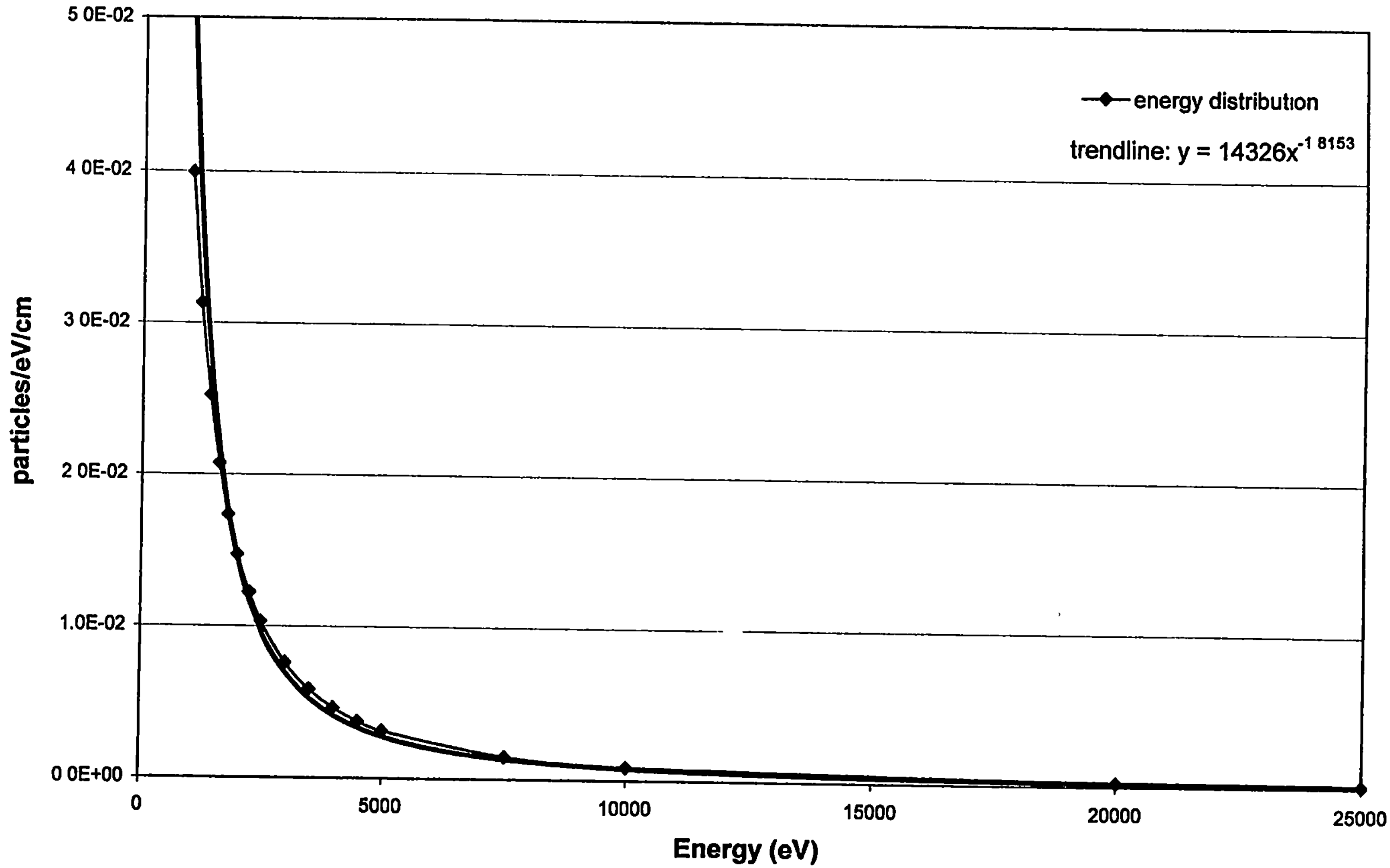

Figure 3.7. Energy distribution of secondary electrons from 1050 MeV nucleon^{-1} iron collisions with water molecules.

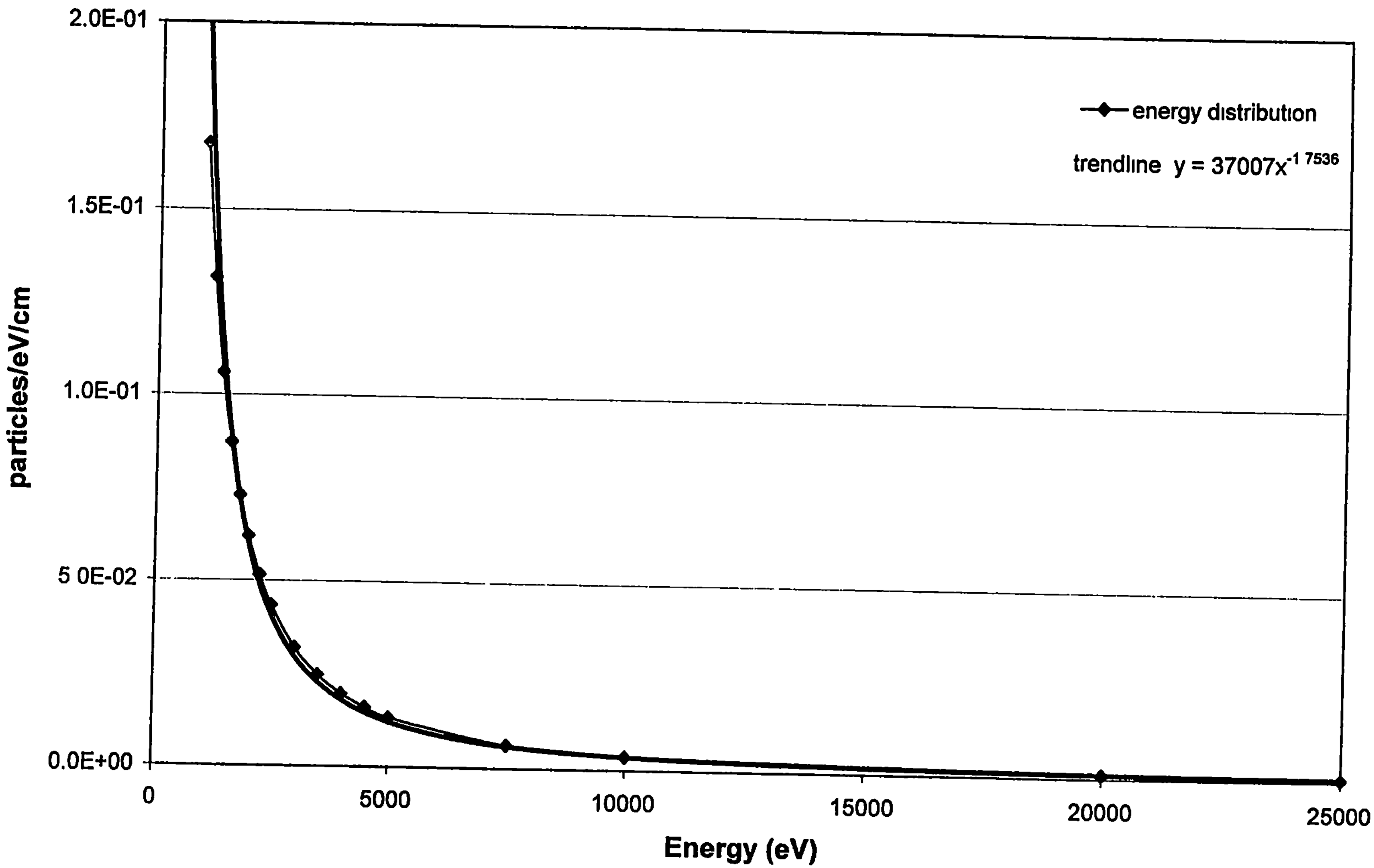

Figure 3.8. Energy distribution of secondary electrons from 250 MeV nucleon^{-1} iron collision with water molecules.

distribution of secondary electrons from the impact of the iron beam on the water target. The power trend-line ($y = 37007x^{-1.7536}$), also shown in this figure, was integrated between energy points to generate a continuous distribution of energies and probabilities for the MCNP input involving the 250 MeV nucleon^{-1} iron beam.

3.4.2. Statistical Interpretation

The relative error for each energy bin in a tally is provided alongside the tally result. These errors correspond to one standard deviation and are only reliable when the error is fairly low. The MCNP4B manual (15) states the following criteria for determining the usefulness of the errors:

- > 50% Useless
- 20 – 50% Believable within a factor of a few
- 10 – 20% Questionable
- < 10% Generally reliable except for point detectors
- < 5% Generally reliable for point detectors.

According to the Central Limit Theorem, the relative error should decrease proportionally to $1/\sqrt{N}$; however, the MCNP manual does not guarantee this decrease because of the "statistical nature of tallies" (15) Since point detector tallies were not chosen in this study, an error of less than ten percent is required.

Another check provided by MCNP is the figure of merit (FOM). The FOM is a tally reliability indicator "If the tally is well-behaved, the FOM should be approximately a constant with the possible exception of statistical fluctuations very early in the problem" (15). The FOM is equivalent to the inverse of the relative error squared multiplied by the computer run time. The FOM can be used to determine the number of histories that are necessary to achieve reliable results for a problem by checking that the FOM remains constant as a function of the number of histories.

Also provided in the MCNP output is the results of ten statistical checks for each tally performed during that run. These checks include the behavior of the mean, the value and behavior of the relative error, variance of the variance, and the figure of merit; and the slope of the pdf. An example of one of the ten statistical checks charts produced in MCNP is given in Table 3.3. If any of the ten statistical checks is not met, the true result may not be represented even if the relative error is considered reliable For all runs performed in this study, every run passed all ten statistical checks and had relative errors below ten percent The combination of these two checks indicates that the results are generally reliable.

Table 3.3. Results of 10 statistical checks for estimated answer for tally 4.

Statistical Checks		Desired	Observed	Passed?
Mean	Behavior	random	random	yes
Relative Error	Value	< 0.10	0.01	yes
	Decrease	yes	yes	yes
	Decrease Rate	1/√nps	yes	yes
Variance of the Variance	Value	< 0.10	0.00	yes
	Decrease	yes	yes	yes
	Decrease Rate	1/nps	yes	yes
FOM	Value	constant	constant	yes
	Behavior	random	random	yes
PDF	Slope	> 3 00	10 00	yes

4. RESULTS

The results for this study are given in two sections. The first section presents the results of the particle flux tally (F4) for both beam energies, and includes all source and cell tally locations This section also displays multiple comparisons between energy binned results. The second section presents the results of the energy deposition tally (*F8), and the corresponding lineal energy calculations. This final section also gives a comparison between the lineal energy results from the 1050 MeV nucleon^{-1} iron beam for this study and the experimental lineal energy results for the same beam energy by S.E. Rademacher et al (4).

4.1. F4 TALLY RESULTS

The flux results for the two iron beams and source/tally locations are given in Table 4.1. The flux results given in this table are the total particle fluxes in the particular cell of interest (the tally cell). Flux results displayed in energy bins, from 0.001 to 1.0 MeV, are given in Appendix C.

The seven cases, described below, are exactly the same for both beam energies; therefore, each case is only described once. When the secondary electron source is located on the outside of the A-150 plastic wall (surface 2), the following three cases can be studied. The letter notation correlates with the different cases in Table 4.1.

Table 4.1. **Flux results for the various beams and source/tally locations.**

Beam Type		Location of Source	Location of Tally	Cell 1 Importance	Cell 2 Importance	Flux (#/cm^2/se)[b]	Error (%)
250 MeV/n[a] iron	A.	Surface 2	Cell 2	0	1	2 804E-3	0.76
	B.	Surface 2	Cell 2	1	1	2.997E-3	0 75
	C.	Surface 2	Cell 1	1	1	1.309E-3	2.06
	D.	Surface 1	Cell 2	0	1	2.772E-3	0 75
	E.	Surface 1	Cell 2	1	1	2.959E-3	0 73
	F.	Surface 1	Cell 1	1	0	3.531E-1	0.10
	G.	Surface 1	Cell 1	1	1	3.855E-1	0.11
1050 MeV/n[a] iron	A.	Surface 2	Cell 2	0	1	2.140E-3	0 85
	B.	Surface 2	Cell 2	1	1	2.275E-3	0.90
	C.	Surface 2	Cell 1	1	1	9.413E-4	2.45
	D.	Surface 1	Cell 2	0	1	2.117E-3	0.84
	E.	Surface 1	Cell 2	1	1	2.263E-3	0.82
	F.	Surface 1	Cell 1	1	0	3.337E-1	0.11
	G.	Surface 1	Cell 1	1	1	3.629E-1	0.11

[a]nucleon
[b](particles/cm^2/source electron)

A. The contribution to the particle flux in the plastic wall is only from electrons that pass through the wall

B. The contribution to the particle flux in the plastic wall is from electrons that pass through the wall plus electrons that re-enter the wall from the gas.

C The contribution to the particle flux in the propane gas is from electrons that pass through the gas plus electrons that re-enter the gas from the wall.

When the secondary electron source is located on the outside of the propane-based tissue equivalent gas (surface 1), the following four cases can be studied.

D The contribution to the particle flux in the plastic wall is only from electrons that pass through the wall.

E. The contribution to the particle flux in the plastic wall is from electrons that pass through the wall plus electrons that re-enter the wall from the gas.

F. The contribution to the particle flux in the propane gas is only from electrons that pass through the gas This case also represents the wall-less situation

G. The contribution to the particle flux in the propane gas is from electrons that pass through the gas plus electrons that re-enter the gas from the wall.

With all seven cases, if either cell one or cell two has an importance of zero, particles that enter that cell will die immediately; therefore, the resultant flux does not include re-entrant particles.

As can be seen in Table 4.1, all errors for both beams, except those for case C, are under one percent, and the errors for case C are under three percent for both beams. According to the statistical interpretation described earlier in Section 3.4.2, these results are generally reliable Also notable in Table 4.1 is that the flux results are lower for the higher energy beam for all seven cases, especially for the cases in which the source is located on surface 2.

Multiple comparisons can be made between the energy binned flux results for all of the cases described in Table 4.1. The first comparison, when the source is on surface 2, is between the electrons that only enter the wall (case A) and the electrons that enter the wall plus the electrons that re-enter the wall from the gas (case B). Figure 4.1 shows the comparison for the 250 MeV nucleon^{-1} iron beam. The comparison for the 1050 MeV nucleon^{-1} iron beam is shown in Figure 4.2. The difference between the lines in both figures is the electrons that re-enter the wall from the gas (delta rays or re-entrant particles).

The second comparison, when the source is located on surface 1, is between the electrons that only enter the wall (case D) and the electrons that enter the wall plus the electrons that re-enter the wall from the gas (case E). The comparison for the 250

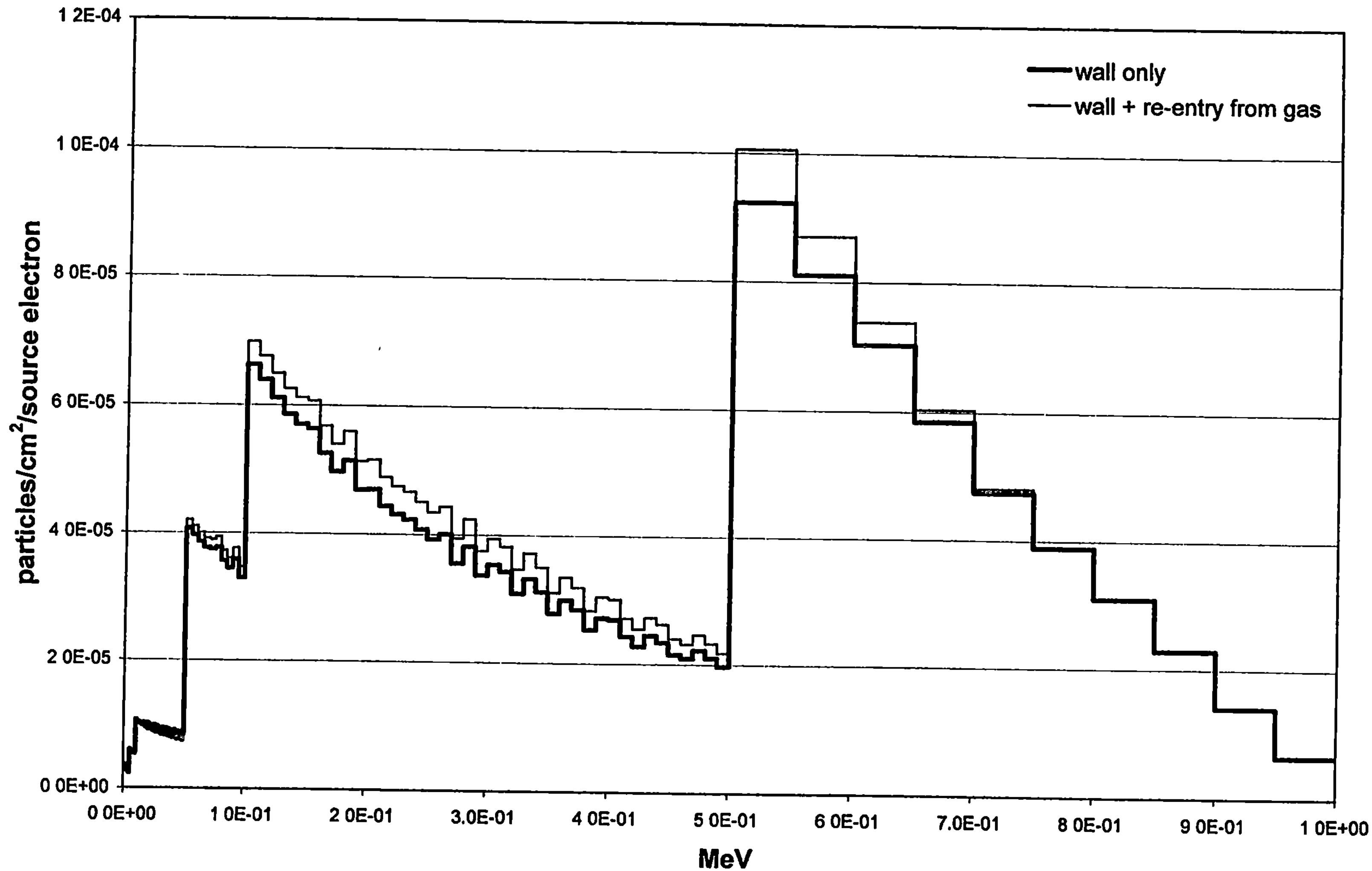

Figure 4.1. Electron flux in the A-150 plastic wall from the 250 MeV nucleon^{-1} iron beam given that the source is located on surface 2.

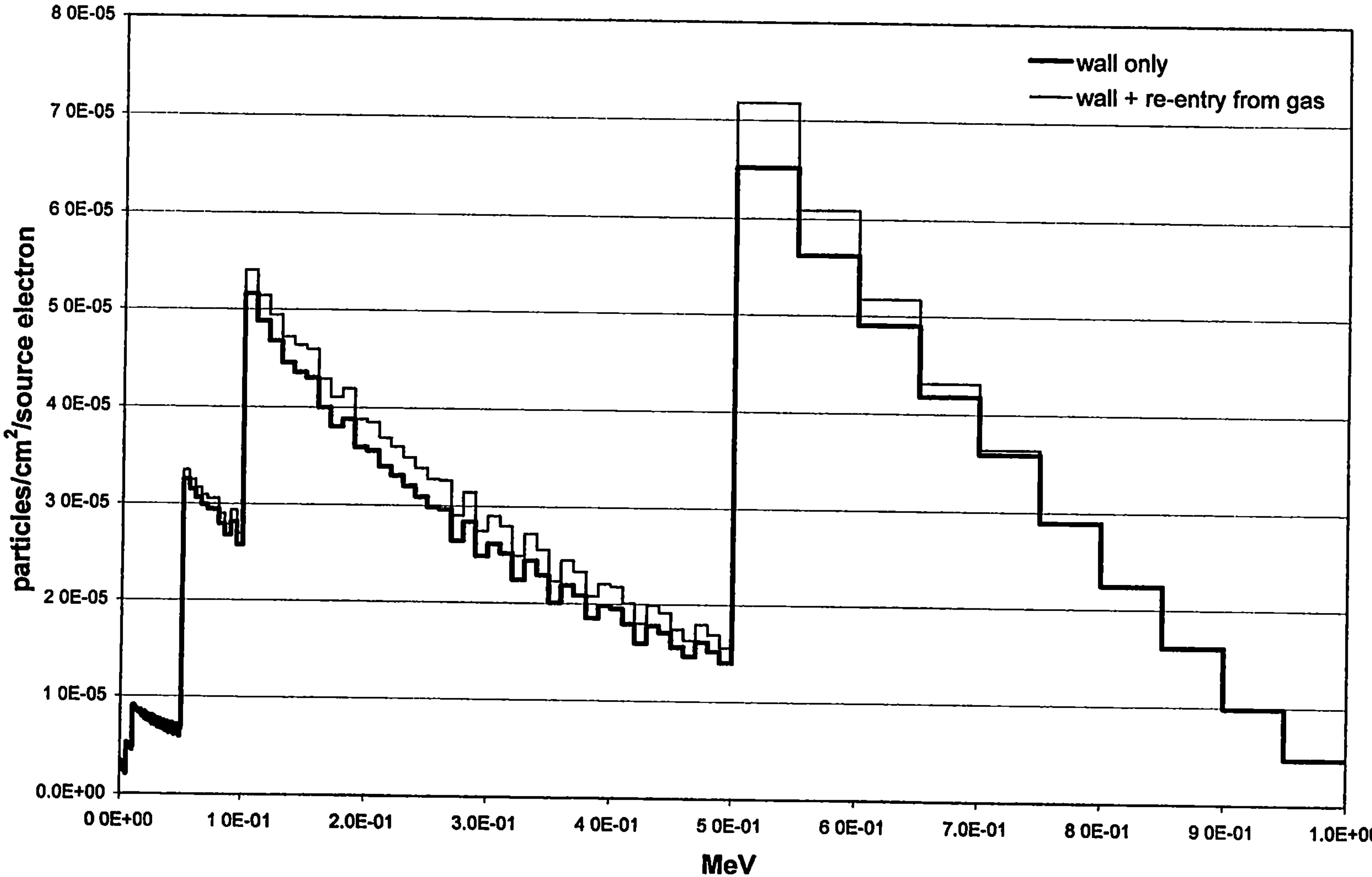

Figure 4.2. Electron flux in the A-150 plastic wall from the 1050 MeV nucleon^{-1} iron beam given that the source is located on surface 2.

MeV nucleon^{-1} iron beam is shown in Figure 4.3. Figure 4.4 shows the comparison for the 1050 MeV nucleon^{-1} iron beam As with the first comparison, the difference between the two lines in both figures is the electrons that re-enter the wall from the gas

The third comparison, when the source is located on surface 1, is between the electrons that only enter the gas (case F) and the electrons that enter the gas plus the electrons that re-enter the gas from the wall (case G). The comparison for the 250 MeV nucleon^{-1} iron beam is illustrated in Figure 4.5, and the comparison for the 1050 MeV nucleon^{-1} iron beam is shown in Figure 4.6. The difference between the two cases in both figures is the electrons that re-enter the gas from the wall.

As can be seen with these three comparisons, the case that includes re-entrant particles is always greater than the case that does not. This means that the density difference between the A-150 plastic wall and the propane gas causes problems in the resultant particle flux in either the wall or the gas

A final comparison of the electron flux in the propane gas is between the solid-wall and the wall-less TEPCs. Figure 4.7 shows the comparison for the 250 MeV nucleon^{-1} iron beam. The comparison for the 1050 MeV nucleon^{-1} iron beam is shown in Figure 4 8. For the solid-wall case, the secondary electron source is located on surface 2 and the particle flux tally is in cell 1 (case C) and includes electrons that enter the gas and those that re-enter the gas from the wall. The source is located on surface 1 for the wall-less case (case F). As can be seen from these two figures, the flux increases with energy for the solid-wall TEPC and decreases with energy for the wall-less TEPC until the two meet at approximately 0.5 MeV. This leads one to assume that the wall lowers the flux of the lower energy electrons.

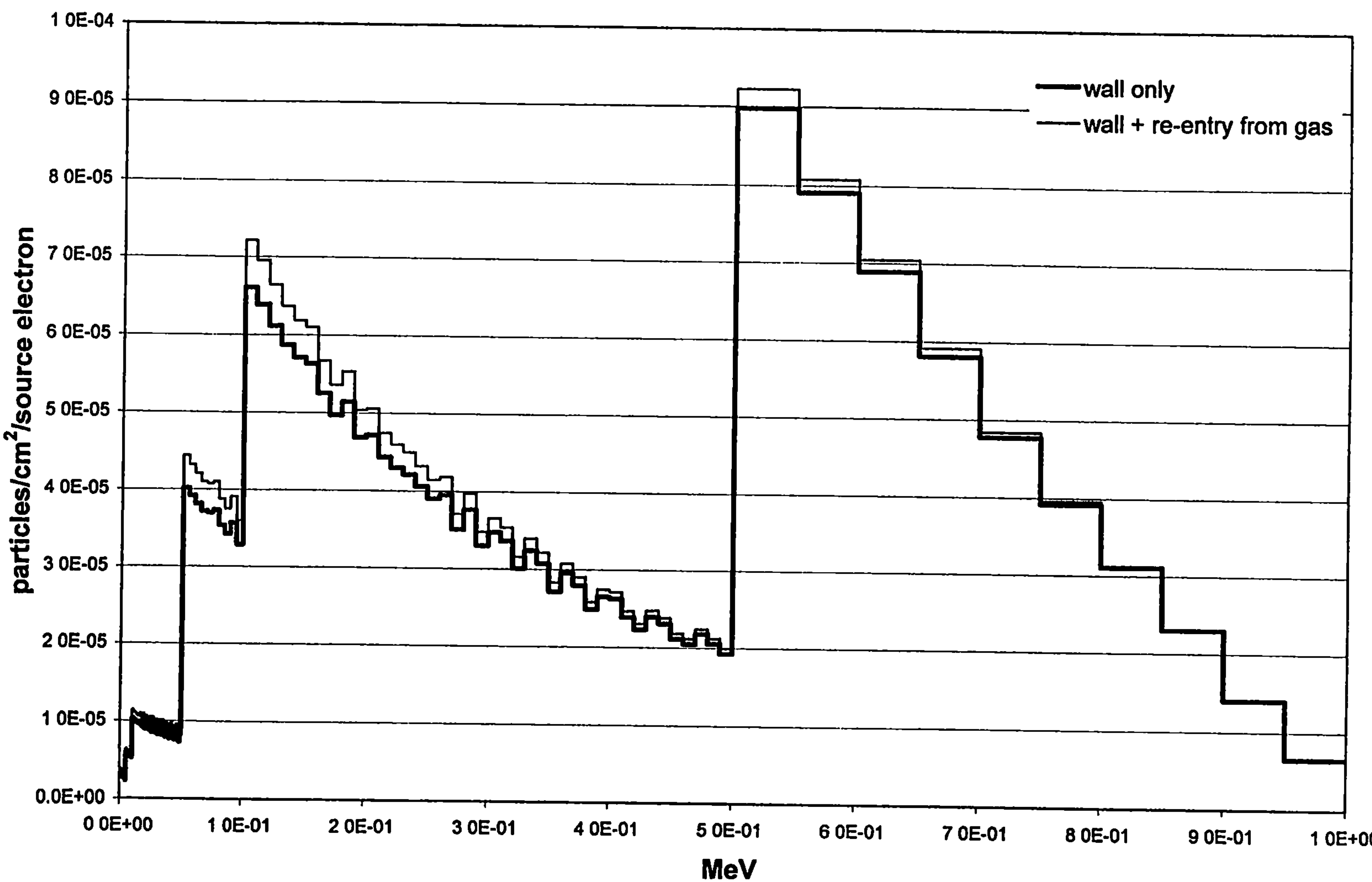

Figure 4.3. Electron flux in the A-150 plastic wall from the 250 MeV nucleon^{-1} iron beam given that the source is located on surface 1.

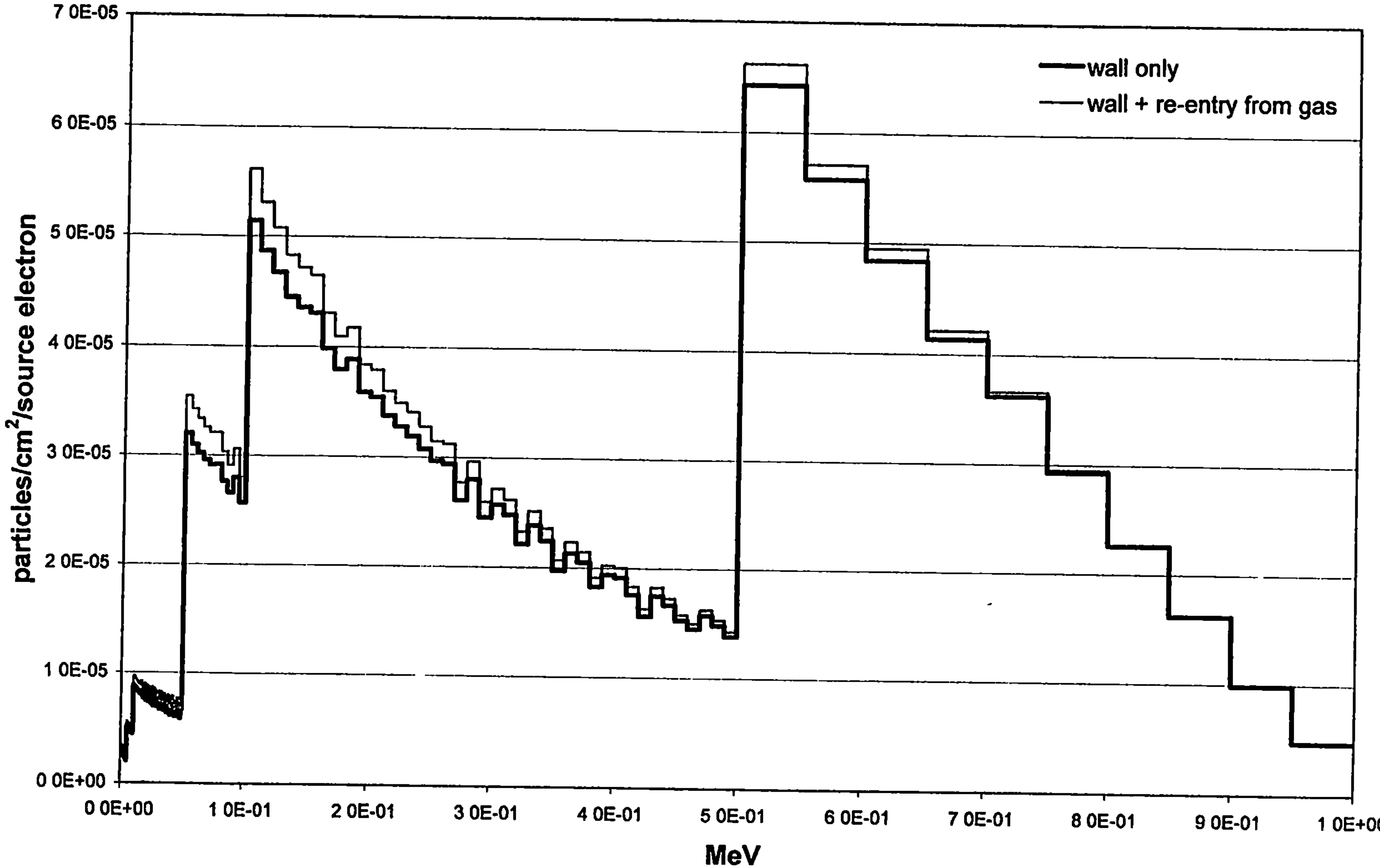

Figure 4.4. Electron flux in the A-150 plastic wall from the 1050 MeV nucleon^{-1} iron beam given that the source is located on surface 1.

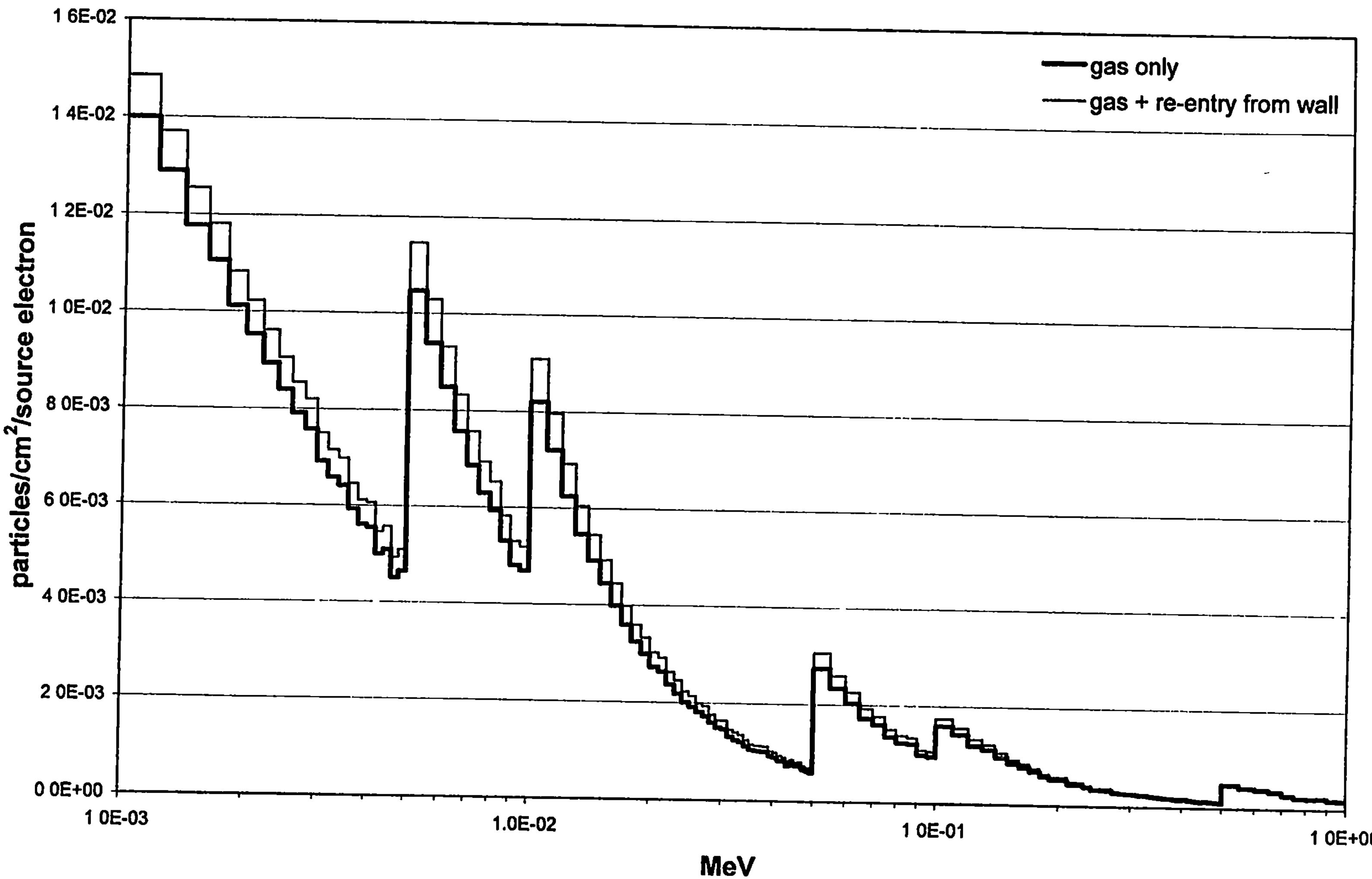

Figure 4.5. Electron flux in the propane gas from the 250 MeV nucleon^{-1} iron beam given that the source is located on surface 1.

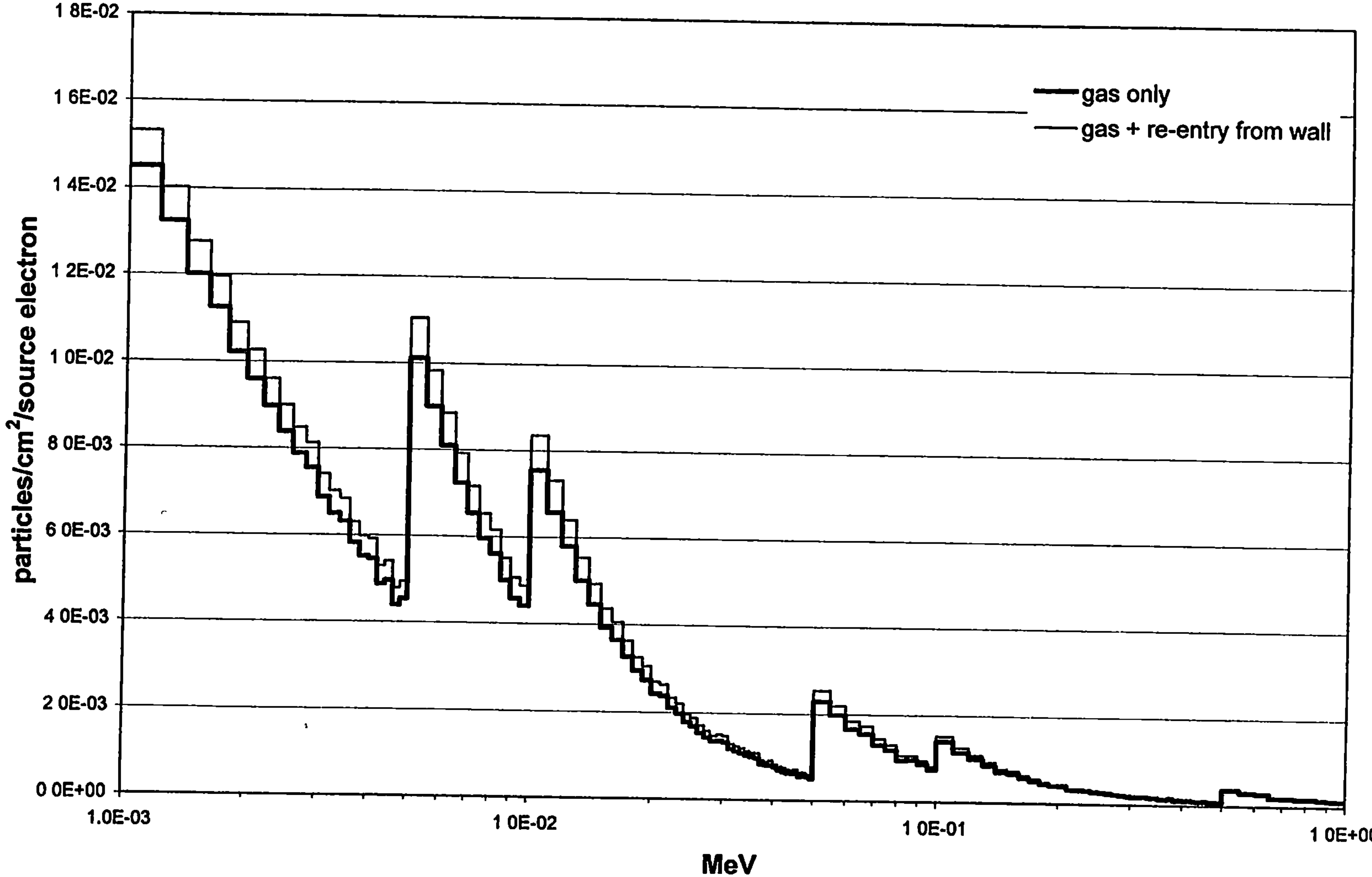

Figure 4.6. Electron flux in the propane gas from the 1050 MeV nucleon^{-1} iron beam given that the source is located on surface 1.

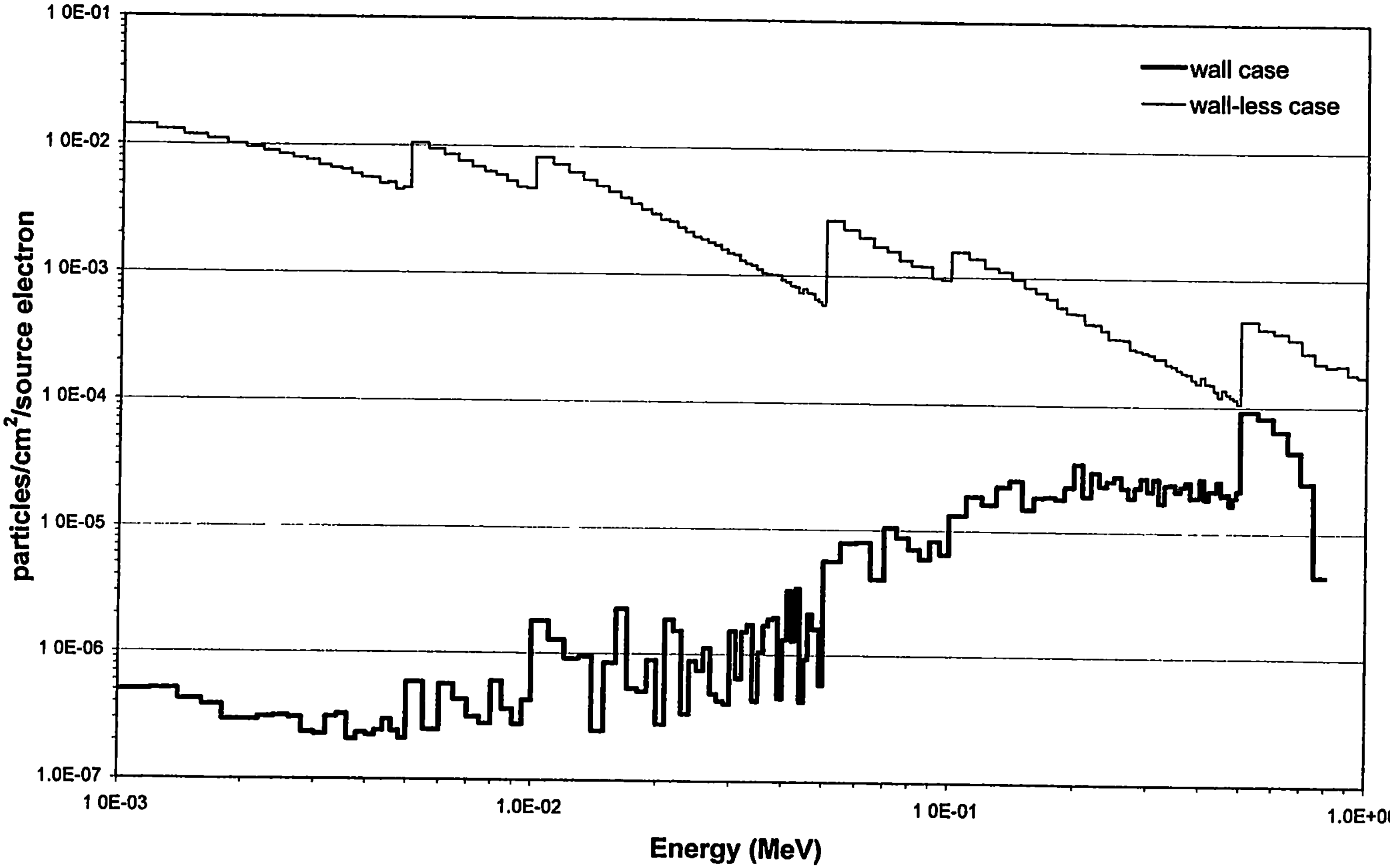

Figure 4.7. Comparison of electron flux for the solid-wall versus the wall-less TEPC in the propane gas from the 250 MeV nucleon^{-1} iron beam.

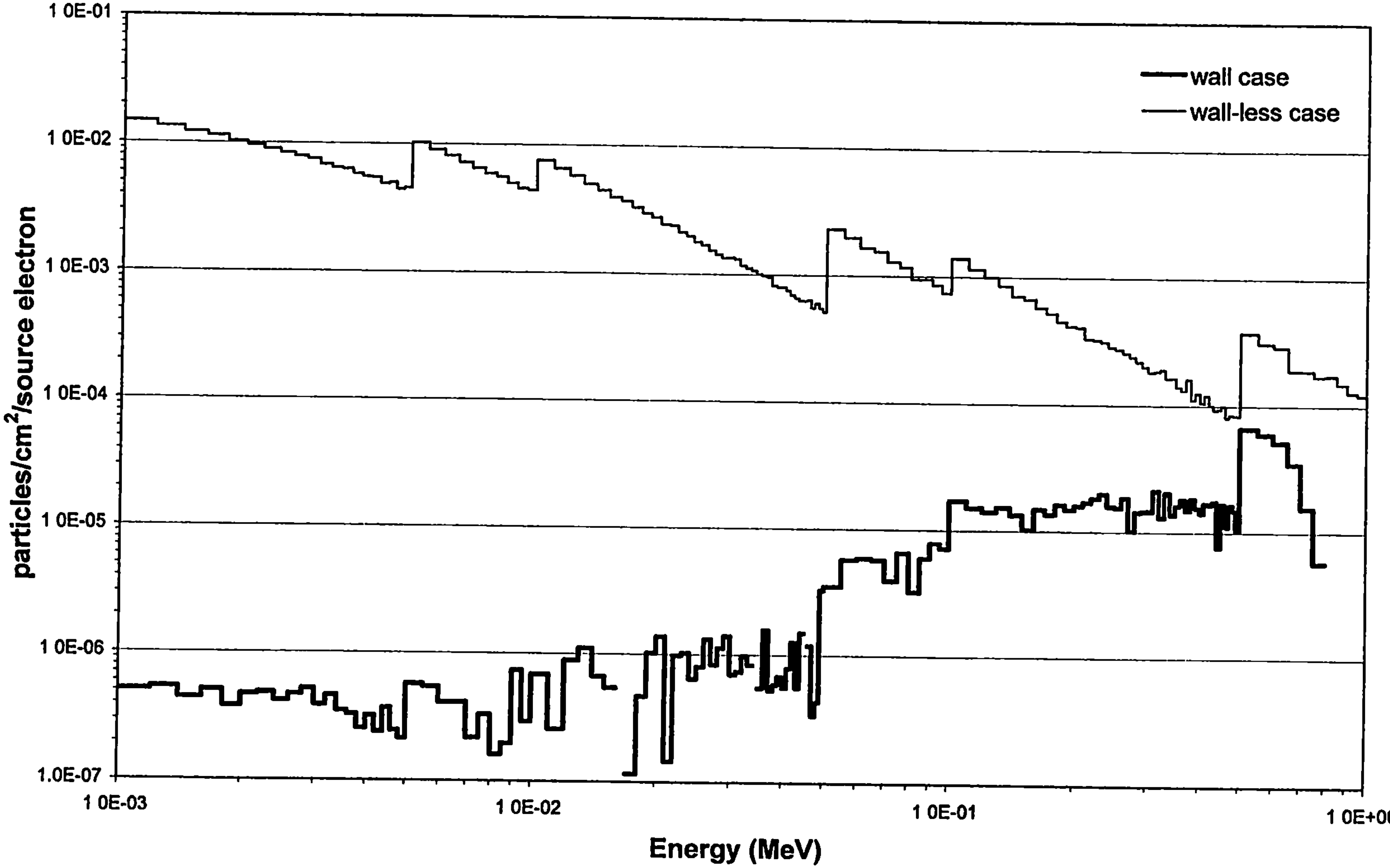

Figure 4.8. Comparison of electron flux for the solid-wall versus the wall-less TEPC in the propane gas from the 1050 MeV nucleon^{-1} iron beam.

4.2. *F8 TALLY RESULTS

The energy deposition results for the two beams for the solid-wall and wall-less TEPCS are given in Table 4 2. Also illustrated in this table are the impact parameter and lineal energy calculations for these four TEPC/beam combinations. The impact parameter is the perpendicular distance from the center of the sphere An impact parameter of 1 mm, is the closest to the center of the propane gas sphere, while an impact parameter of 6.3 mm is the closest to the interface between the propane gas and the plastic wall. The impact parameters that are within the solid plastic wall begin with 6.37 mm. The lineal energy is the energy absorbed in the cell of interest divided by the chord length in the gaseous volume (0.8414 cm), as given in Section 2.2.1.

As can be seen in Table 4.2, all errors for both beams are under ten percent Since the tally used for these cases is not for point detectors, these results are all generally reliable.

Two comparisons have been made between the impact parameter and the lineal energy – one for each beam. Figure 4.9 shows the comparison for the solid-wall and wall-less TEPCs for the 250 MeV nucleon^{-1} iron beam. Figure 4.10 shows this comparison for the 1050 MeV nucleon^{-1} iron beam. For both beam energies, the solid-wall TEPC has a smaller lineal energy than the wall-less TEPC for each corresponding impact parameter. The reason for the larger lineal energy in the wall-less TEPC is because the source is directly impinging on the gaseous volume and there is no attenuation of particles by the wall. This is even with the fact that the solid-wall has an increased number of delta rays released into the gas by the interaction between the A-150 plastic wall and the propane gas.

Table 4.2. Energy deposition and lineal energy results for the various beams and impact parameter locations.

Beam Type			Impact Parameter (mm)	Energy Deposition (MeV/se)[b]	Error (%)	Lineal Energy (keV/μm)
250 MeV/n[a] iron	Solid-wall Cases	A	1	2.991E-3	9.57	107.510
		B.	2	2.826E-3	9.98	101.585
		C.	3	2.682E-3	8.93	96.423
		D.	4	2.419E-3	9.19	86 969
		E.	5	1.571E-3	9.00	56.456
		F.	6	4.423E-4	9.01	31.796
		G.	6.1	3.219E-4	9.49	23.144
		H.	6.2	1.979E-4	9.02	14.225
		I.	6.3	6.886E-5	9.70	9.901
		J.	6.37	1.966E-3	5.53	116.822
		K.	6.39	1.852E-3	5.25	110.066
		L.	6.41	1.783E-3	5.17	105.949
		M	6.43	1.606E-3	5.17	95.417
		N.	6.45	1.433E-3	5.13	85.134
		O.	6.5	1.335E-3	4 33	79.318
		P.	6.55	1.011E-3	4.38	60.052
		Q.	6.6	8.834E-4	4.14	52 495
		R.	6.65	7.247E-4	4.09	43.063
		S.	6.7	3.807E-4	3.96	22.622
		T.	6.8	4.088E-4	3.31	24.291
		U.	6.9	3.719E-4	3.08	22.098
		V.	7.0	2.975E-4	2.87	17.680
		W	7.1	2.734E-4	2.62	16.249
		X.	7.2	2.012E-4	2.36	11.956
		Y.	7.3	1.522E-4	2.06	9.047
		Z.	7.4	1.703E-4	1.78	10.122
		a.	7.5	1.321E-4	1.40	7.850
		b.	7.62	9.220E-5	0.34	5.479
	Wall-less Cases	A.	1	1.633E-3	2.31	194.123
		B.	2	1.627E-3	2.22	193.386
		C.	3	1.568E-3	2.21	186.339
		D.	3.5	1.507E-3	2 18	179 125
		E.	4	1.424E-3	2.12	169.224
		F.	4.5	1.318E-3	2.12	156.671
		G.	5	1.157E-3	2.07	137.535
		H.	5.5	9.106E-4	2.26	108.224
		I.	6	5.558E-4	2.97	66.053
		J.	6.2	2.855E-4	4.36	33.930
		K.	6.3	1.008E-4	7.27	11.985

[a](MeV/nucleon); [b](MeV/source electron)

Table 4.2. (continued)

Beam Type			Impact Parameter (mm)	Energy Deposition (MeV/se)[b]	Error (%)	Lineal Energy (keV/μm)
1050 MeV/n[a] iron	Solid-wall Cases	A	1	2.117E-3	9.87	143 041
		B.	2	2.008E-3	9 23	144.338
		C.	3	1.966E-3	9.56	141.321
		D.	4	1.776E-3	8.96	127.660
		E.	5	1.252E-3	9.18	90.042
		F.	6	2.930E-4	9.78	21.069
		G.	6.1	2.461E-4	8.46	17.693
		H.	6.2	1.467E-4	9.49	10.549
		I.	6.3	5.242E-5	8.67	3.769
		J.	6.37	1.341E-3	6.73	79.657
		K.	6 39	1.273E-3	5.95	75.640
		L.	6.41	1.194E-3	5.94	70.975
		M	6.43	1.080E-3	5.96	64.171
		N	6.45	1.045E-3	5.71	62.086
		O.	6 5	8.614E-4	5.14	51.187
		P.	6.55	6 637E-4	5.14	39.439
		Q	6.6	7 020E-4	4.77	41 715
		R.	6.65	4.377E-4	4.76	26.010
		S	6.7	3.603E-4	4.71	21.410
		T.	6.8	3.159E-4	3.99	18.772
		U.	6.9	2.433E-4	3.57	14.458
		V.	7.0	2.302E-4	3.37	13.679
		W	7.1	1.792E-4	3.03	10.649
		X.	7.2	1.483E-4	2.69	8.812
		Y.	7.3	1.502E-4	2.38	8.925
		Z.	7.4	1.178E-4	2.02	7.000
		a.	7.5	8.500E-5	1.61	5.051
		b.	7 62	7.800E-5	0.34	4.635
	Wall-less cases	A.	1	1.638E-3	2.18	194.708
		B.	2	1.623E-3	2.17	192.936
		C.	3	1.579E-3	2.13	187.702
		D	3.5	1.533E-3	2.12	182.211
		E.	4	1.418E-3	2.04	168.506
		F.	4.5	1.312E-3	1.99	155.914
		G.	5	1.183E-3	2.05	140.549
		H.	5.5	9.432E-4	2.2	112 095
		I.	6	5 475E-4	2.96	65.065
		J.	6.2	2.867E-4	4.18	34.068
		K.	6.3	1.004E-4	7.19	11.935

[a](MeV/nucleon); [b](MeV/source electron)

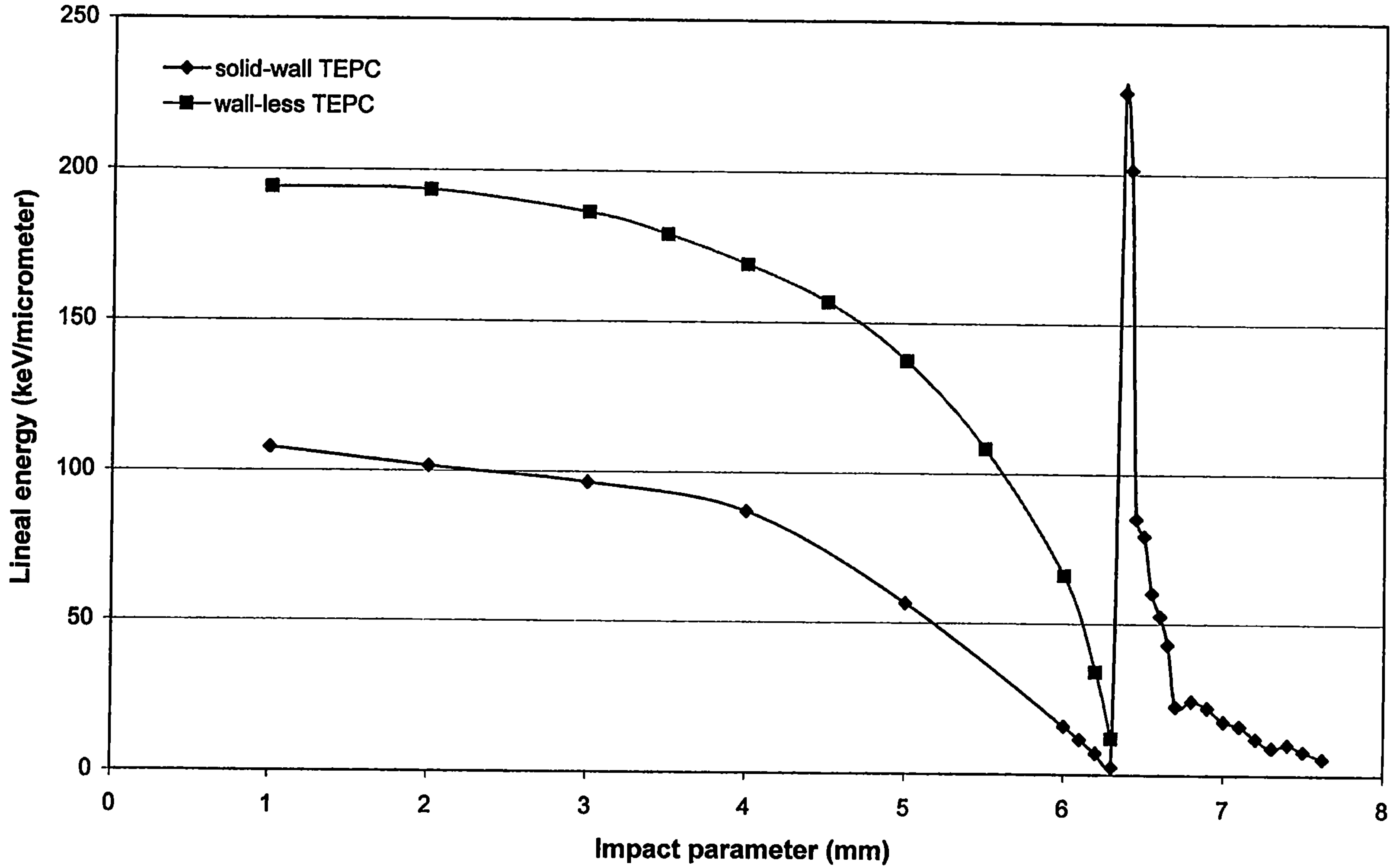

Figure 4.9. Impact parameter (mm) versus lineal energy (keV micrometer^{-1}) for the 250 MeV nucleon^{-1} iron beam.

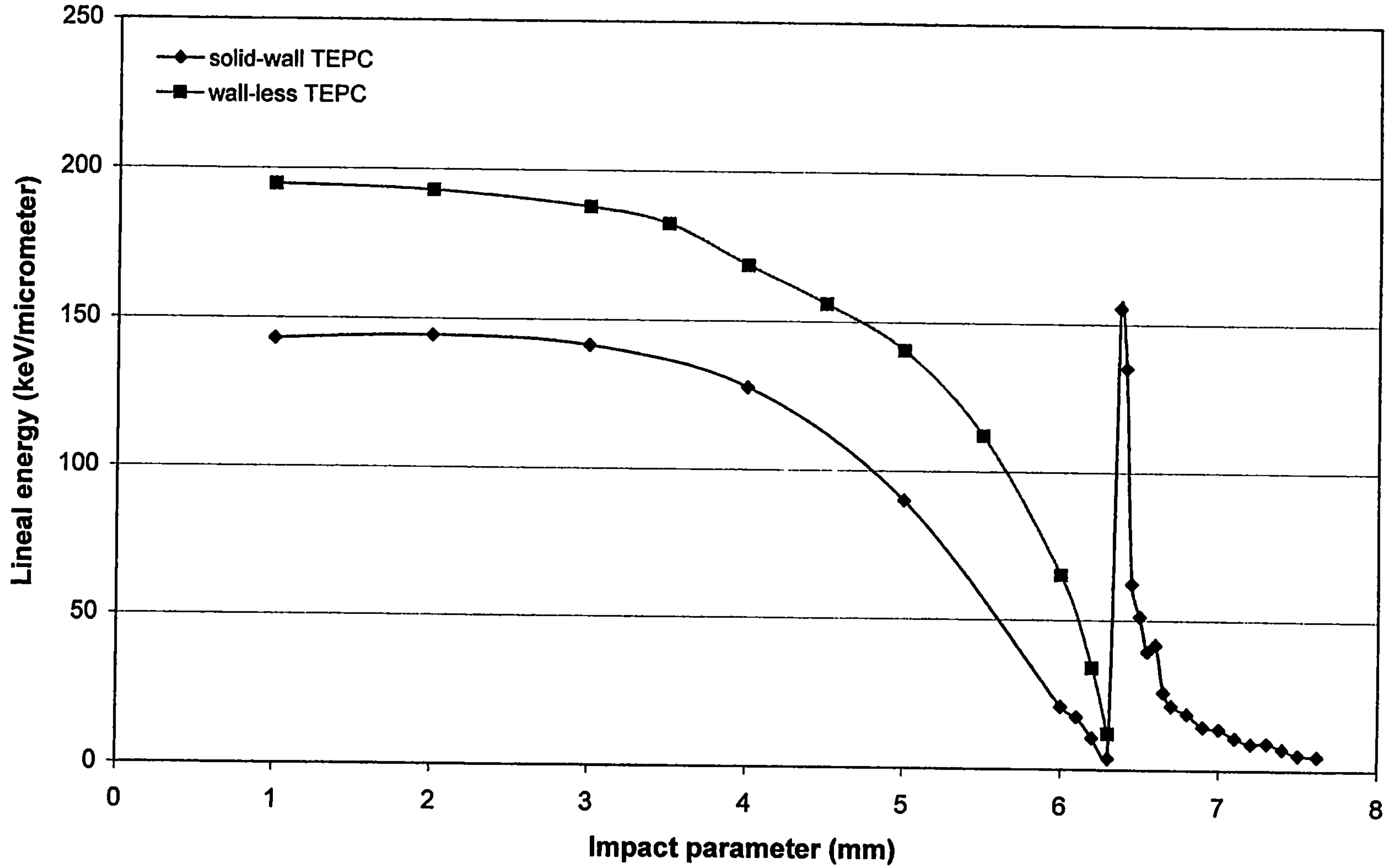

Figure 4.10. Impact parameter (mm) versus lineal energy (keV micrometer^{-1}) for the 1050 MeV nucleon^{-1} iron beam.

A final comparison can be performed for the lineal energy as a function of impact parameter between the results in this study for the 1050 MeV nucleon^{-1} iron beam on the solid-wall case (Figure 4.10) and the experimental results of S.E. Rademacher et al for the same beam energy (4). Figure 4.11 displays the results of S.E. Rademacher et al for the TEPC described in Section 3.1.

The open circles (o) in Figure 4.11 represent the experimental data. The solid line (—) represents the results of calculations with the Chatterjee et al (24) model that includes radial energy loss from delta rays. The solid circles (●) represent calculations for particles with LET equal to 149 keV μm^{-1}, but without radial energy loss.

The comparison between the solid line in Figure 4.11 and the solid-wall case in Figure 4.10 shows that the results from this study for lineal energy as a function of

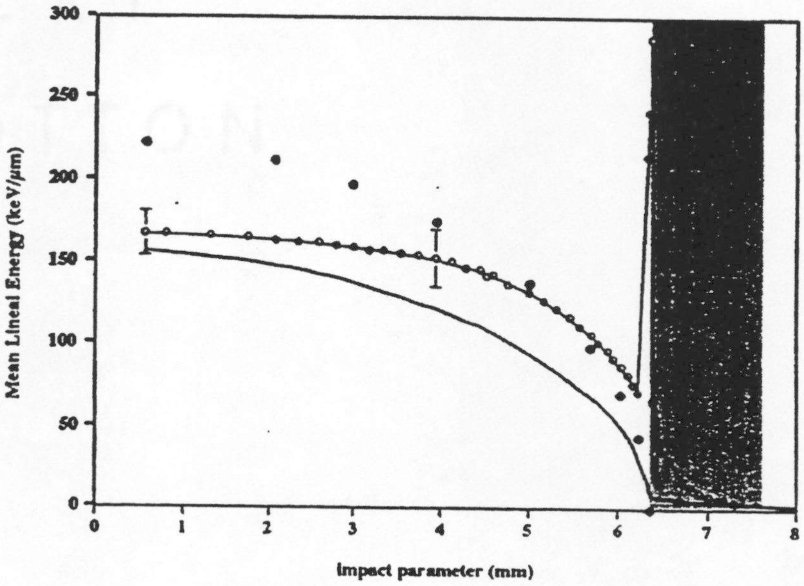

Figure 4.11. Mean values of lineal energy as a function of impact parameter. (4)

impact parameter are slightly lower in energy than the Chatterjee model calculations and the experimental results However, this study's results are only offset by a small fraction that actually is covered by the error bars from the experimental results and the relative errors from this study. This result implies that the model used in this study for the determination of energy deposition closely relates to the Chatterjee model, which is a well-known model.

As can be seen by Figures 4.10 and 4.11, the peak at the interface between the wall and the gas, which occurs in the experimental data, also occurs in the model used in this study, but not in the Chatterjee or LET model. The occurrence of this peak signifies that wall effects do occur in a TEPC mainly because of the density difference between the wall and gas.

The peak for the model in this study is approximately half of the peak for the experimental results. It is approximately the average between the experimental peak maximum and minimum. This difference arises from the fact that it is difficult to measure the energy deposition at extremely small intervals near the interface, and also, there is no way of knowing how accurate the lineal energy measurements for the experimental results were. Also, MCNP only calculates the energy deposited in a single cell, not in overlapping cells or on surfaces. The observance of a peak indicates that the MCNP model can offset the escape of delta rays created in the gas cavity with the added energy deposition of the delta rays created in the plastic wall, which is what is seen in the experimental results (4)

5. CONCLUSIONS

The MCNP transport code was used to evaluate the effect of the wall on the response of a tissue equivalent proportional counter (TEPC). This evaluation was implemented by modeling the TEPC and simulating the transport of secondary electrons produced by two different energetic iron beams through the TEPC. The results of forty-six runs from each iron beam were used to characterize the flux response of the TEPC in either the solid-wall or wall-less form for different source and tally locations. As expected, re-entrant particles in either the gas or the wall consistently directed the flux response for the gas or the wall much higher than would be normally seen in a microscopic volume of tissue.

Multiple comparisons were plotted between the electrons that only enter the wall or gas and the electrons that enter the wall and re-enter the wall or gas from the opposite material. The differences between these comparisons involved the location of the secondary electron source, the location of the cell tally, and the primary beam that produced the secondary electron source. These comparisons illustrate the increase in the flux response caused by delta rays or re-entrant particles. This leads to the conclusion that the density difference between the A-150 plastic wall and the propane gas causes increases in the resultant particle flux in either the wall or the gas that would not have occurred in a microscopic volume.

Another flux response comparison in the propane gas was made between the solid-wall and the wall-less TEPC. This comparison shows that the solid-wall causes the flux in the gas to decrease in magnitude for lower energies. However, this comparison also shows that the flux in the gas from the solid-wall TEPC rises to meet the flux response from the wall-less TEPC at approximately 0.5 MeV and then decreases again. In other words, the flux increases with energy for the solid-wall TEPC and decreases with energy for the wall-less TEPC. This leads one to conclude that the wall attenuates the lower energy electrons at a much higher rate than the higher energy electrons, therefore causing a lower initial flux of particles that enter the gaseous volume for the lower end of the secondary electron energy spectrum.

MCNP does an adequate job of modeling the flux of secondary electrons in different portions of the TEPC based on the source location. Results produced by MCNP are justified by the relatively small errors and passing rate of the ten statistical checks.

In addition to characterizing the flux response, the energy deposition as a function of impact parameter within the TEPC was evaluated. The wall-less TEPC has a higher lineal energy as a function of impact parameter than the solid-wall TEPC This leads to the conclusion that although the gas/wall interface increases the number of delta rays and re-entrant particles within the gas, it does not express all the particles that should reach the gas due to the attenuation within the wall. The wall-less TEPC gives a much better approximation of a microscopic volume.

The final comparison was between the lineal energy results for the MCNP model in this study and the experimental results from S.E. Rademacher et al. The lineal energy, which was calculated from the deposited energy in small spherical rings within the TEPC as a function of impact parameter for the 1050 MeV nucleon^{-1} iron beam, was slightly lower than the experimental results seen by S.E. Rademacher et al (4).

The most important conclusion to be drawn from this work is the fact that MCNP has the ability to model wall effects in a TEPC However, three negative conclusions can also be drawn from this comparison First, the model chosen to calculate the secondary electron energy spectrum, the Rudd model, was based on a singly-differential cross-section. This model took into account all angles. This is not a bad approximation; however, it would be better to choose a spectrum based on the Rudd model doubly differential cross-section This would allow all angles and energies to be taken into account – not just the radial distribution or the forward directions. Secondly, it was assumed that the source used in this study was isotropic on the outside of the solid-wall while the experimental results were for a beam hitting the TEPC. Lastly, the transport code chosen to perform this study, MCNP, might not be the best code needed to deal with such a small geometry and high energy electrons, therefore, to investigate wall effects it may be useful to use a different transport code, such as EGS4.

Finally, the main purpose of this study was to model the wall effects of a TEPC using MCNP. MCNP did a good job with the particle flux response calculations, and a reasonable job with the energy deposition, or lineal energy calculations. MCNP has the ability to see the wall effects; therefore, it is the conclusion of this study that MCNP can be used to model wall effects within a tissue equivalent proportional counter.

6. FUTURE WORK

Recommendations for future work include a continued modeling of the wall effects in MCNP by further developing the TEPC model – including the gas inlet and outlet openings and separating the anode wire and double helix. Also, additional modeling can be performed using additional codes, such as the Electron-Gamma Shower (EGS4) code or the PITS code. A comparison between the 250 MeV nucleon^{-1} iron beam results and the experimental results performed by Dr. Thomas Borak for that same beam energy need to be performed in order to check the MCNP results for this study. Finally, additional ion beams should be modeled to help in determining the efficiency of the MCNP model. These beams should include 400, 600, and 740 MeV nucleon^{-1} iron beams; 400 MeV nucleon^{-1} silicon, carbon, oxygen, and helium beams; and a 250 MeV nucleon^{-1} hydrogen beam. These eight beams were chosen because Dr. Thomas Borak has either completed the experiments with the TEPCs and the beam, or plans on performing the experiment in the recent future.

REFERENCES

REFERENCES

1. J.E. Turner, An Introduction to Microdosimetry *Radiation Protection Management* **9** (3), 25-58 (May/June 1992)
2. A.M. Kellerer, Fundamentals of Microdosimetry. In *The Dosimetry of Ionizing Radiation* (K.R. Kase, B. Bjärngard, and F.H. Attix, Eds.) Vol. 1. Academic Press, NY (1985).
3. ICRU, *Microdosimetry,* Report No. 36, International Commission on Radiation Units and Measurements, Bethesda, Maryland, 1983.
4. S.E. Rademacher, T.B. Borak, C. Zeitlin, L. Heilbronn and J Miller, Wall Effects Observed in Tissue-Equivalent Proportional Counters from 1 05 GeV/nucleon Iron-56 Particles. *Radiation Research* **149**, 387-395 (1998)
5. Tsoulfanidis, Nicholas, "Measurement and Detection of Radiation," Second Edition Taylor and Francis, 1995.
6. Hall, Eric J., "Radiobiology for the Radiologist," Fourth Edition. Lippincott-Raven Publishers, 1994.
7. Anderson, David W., "Absorption of Ionizing Radiation " University Park Press, 1984.
8. H. Nikjoo, S. Uehara, W.E. Wilson, M. Hoshi and D.T. Goodhead, Track structure in radiation biology: theory and applications. *International Journal of Radiation Biology* **73**(5), 355-364 (1998).
9. A Chatterjee and H.J. Schaefer, Microdosimetric Structure of Heavy Ions in Tissue *Radiation and Environmental Biophysics* **13**, 215-227 (1976).

10. ICRU, *Secondary Electron Spectra from Charged Particle Interactions*, Report No. 55, International Commission on Radiation Units and Measurements, Bethesda, Maryland, 1996.

11. Knoll, Glenn F., "Radiation Detection and Measurement," Second Edition. John Wiley and Sons, 1989.

12. A.M. Kellerer, An Assessment of Wall Effects in Microdosimetric Measurements *Radiation Research* **47**, 377-386 (1971).

13. P.M. Failla and G. Failla, Measurement of the Dose in Small Tissue Volumes Surrounding "Point" Sources of Radioisotopes. *Radiation Research* **13**, 61-91 (1960).

14. L.A. Braby and W.H Ellett, Ionization in Solid- and Grid-Walled Detectors. *Radiation Research* **51**, 569-580 (1972).

15. J.F. Briesmeister, ed. "MCNP™ – A General Monte Carlo N-Particle Transport Code," Los Alamos National Laboratory report LA-12625-M (March 1997).

16. M.E. Riley, C.J. MacCullum and F. Biggs, Theoretical Electron-Atom Elastic Scattering Cross Sections, Selected Elements, 1 keV to 256 keV. *Atomic Data and Nuclear Data Tables* **15**, 443 (1975).

17. J.B. Smathers et al, Composition of A-150 tissue-equivalent plastic. *Medical Physics* **4** (1), 74-77 (Jan./Feb. 1977).

18. Weast, Robert C., editor, "CRC Handbook of Chemistry and Physics – A Ready-Reference Book of Chemical and Physical Data," 54th Edition. CRC Press, 1973.

19 Density of Various Materials. [web page]; www.mtgloans.com/~thelen/1density.html. [Accessed 11/3/1999]

20 Nominal Compositions of Stainless Steels for Lock, Dam and Hydroelectric Plant Applications. [web page],owww.cecer.army.mil/corrosion/table2.htm. [Accessed 11/3/1999]

21. M.E. Rudd, User-Friendly Model for the Energy Distribution of Electrons from Proton or Electron Collisions. *International Journal of Radiation Applications and Instrumentation, Part D: Nuclear Tracks and Radiation Measurements* **16** (2-3), 213-218 (1989).

22. M.E. Rudd, Differential cross sections for secondary electron production by proton impact. *Physical Review A* **38** (13), 6129-6137 (December 15, 1988).

23. M.J. Berger and S.M. Seltzer, "Stopping Power and Ranges of Electrons and Positrons." Second Edition Report NBSIR 82-2550, National Bureau of Standards, Gaithersburg, MD (1982).

24. A. Chatterjee, H D. Maccabee and C.A. Tobias, Radial cutoff dose calculations for heavy charged particles in water. *Radiation Research* **54**, 479-494 (1973).

APPENDICES

APPENDIX A – RUDD MODEL CALCULATIONS

CONTENTS:

A.1. Rudd model -- Excel spreadsheet set-up

sigma = S/B * (F1+F2w)/(1+w)^3 / {1+exp[alpha(w-wc)/v]} — units = m^2/eV
sigma*(ion) = sigma * Z^2 — units = m^2/eV
sigma(ion) = sigma*(ion) * ND(H2O) * 100^2 — units = particles/eV/cm

F1(v)= L1+H1
L1= C1v^D1/[1+E1v^(D1+4)]
H1= A1ln((1+v^2)/(v^2+B1/v^2))

F2(v)= L2H2/(L2+H2)
L2= C2v^D2
H2= A2/v^2+B2/v^4

wc= 4v^2-2v-R/4B
S= 4(pi)a0^2N(R/B)^2
w= E/B
v= (T/B)^ 5

A1(H2O)=	0.97
B1(H2O)=	8.2
C1(H2O)=	0.4
D1(H2O)=	-0 3
E1(H2O)=	0 38
A2(H2O)=	1.04
B2(H2O)=	17.3
C2(H2O)=	0 76
D2(H2O)=	0.04
alpha=	0.64

	B (eV)
H2O1b1=	12.6
H2O2a1=	14 7
H2O1b2=	18.4
H2O1a1=	32 2
H2O01s=	540

ND(H2O) = 3 35E22 g/cm^3

N = 2

a0 = 5.29x10^-11 m
R = 13 6 eV

T = K.E./lambda
K E. = (MeV/nucleon) * (10^6 eV/MeV) * (# of nucleons)
lambda = 1836

Z = atomic number

A.1. (continued)

Incoming 250 MeV/nucleon iron beam for H2O01s shell:

T=250/1836 MeV= 7625272 eV

NU -- no units

This set-up is the same for the other four shells

E (MeV)	E (eV)	w (NU)	v (NU)	sigma (m^2/eV)	sigma (#/eV/cm)
0 001	1000	1.851851852	118 8312867	4.9406E-28	1.6551E-01
0 0012	1200	2 222222222		3 8811E-28	1.3002E-01
0.0014	1400	2.592592593	wc (NU)	3.1291E-28	1.0483E-01
0 0016	1600	2.962962963	56245 82358	2.5763E-28	8 6305E-02
0 0018	1800	3.333333333		2.1580E-28	7.2292E-02
0.002	2000	3.703703704	S (m^2)	1.8338E-28	6.1433E-02
0 00225	2250	4.166666667	4.4611E-23	1 5219E-28	5 0985E-02
0 0025	2500	4.62962963		1 2833E-28	4 2992E-02
0.003	3000	5.555555556	S/B (m^2/eV)	9 4807E-29	3 1760E-02
0 0035	3500	6.481481481	8.26129E-26	7 2888E-29	2 4417E-02
0 004	4000	7 407407407		5 7776E-29	1.9355E-02
0.0045	4500	8.333333333	L1 (NU)	4.6920E-29	1 5718E-02
0 005	5000	9.259259259	5 27902E-09	3 8859E-29	1 3018E-02
0.0075	7500	13 88888889		1 8489E-29	6 1937E-03
0.01	10000	18.51851852	H1 (NU)	1.0770E-29	3 6079E-03
0.02	20000	37.03703704	6 86503E-05	2.8408E-30	9 5167E-04
0 025	25000	46 2962963		1.8380E-30	6 1574E-04
0 05	50000	92 59259259	F1(v) (NU)	4.6972E-31	1 5736E-04
0.075	75000	138 8888889	6 86556E-05	2 1031E-31	7.0454E-05
0.1	100000	185.1851852		1 1874E-31	3 9777E-05
0 2	200000	370.3703704	L2 (NU)	2 9850E-32	9.9998E-06
0 25	250000	462.962963	0.920048717	1.9125E-32	6.4070E-06
0 5	500000	925.9259259		4.7920E-33	1 6053E-06
0.75	750000	1388.888889	H2 (NU)	2 1314E-33	7 1401E-07
1	1000000	1851 851852	7 37366E-05	1 1993E-33	4 0178E-07
2	2000000	3703.703704		3.0000E-34	1 0050E-07
2.5	2500000	4629.62963	F2(v) (NU)	1 9202E-34	6 4328E-08
5	5000000	9259.259259	7 37307E-05	4.8017E-35	1 6086E-08
7.5	7500000	13888.88889		2 1342E-35	7 1497E-09
10	10000000	18518 51852		1.2006E-35	4 0219E-09

A.2. Source energies and probabilities (250 and 1050 MeV nucleon^{-1} iron beams).

Source energies for 250 and 1050 MeV nucleon^{-1} iron beams

1.0E-3 1 2E-3 1 4E-3 1.6E-3 1.8E-3 2.0E-3 2 2E-3 2 4E-3 2 6E-3 2 8E-3 3 0E-3 3 2E-3
3.4E-3 3.6E-3 3 8E-3 4.0E-3 4 2E-3 4.4E-3 4 6E-3 4 8E-3 5 0E-3 5.5E-3 6 0E-3 6 5E-3
7.0E-3 7 5E-3 8.0E-3 8.5E-3 9.0E-3 9.5E-3 1.0E-2 1.1E-2 1.2E-2 1.3E-2 1.4E-2 1 5E-2
1.6E-2 1.7E-2 1 8E-2 1.9E-2 2 0E-2 2.1E-2 2.2E-2 2 3E-2 2 4E-2 2 5E-2 2.6E-2 2 7E-2
2.8E-2 2.9E-2 3 0E-2 3 1E-2 3.2E-2 3.3E-2 3.4E-2 3 5E-2 3.6E-2 3 7E-2 3.8E-2 3 9E-2
4.0E-2 4.1E-2 4.2E-2 4.3E-2 4.4E-2 4.5E-2 4 6E-2 4.7E-2 4.8E-2 4.9E-2 5.0E-2 5 5E-2
6 0E-2 6 5E-2 7.0E-2 7.5E-2 8.0E-2 8.5E-2 9.0E-2 9 5E-2 1.0E-1 1.1E-1 1 2E-1 1.3E-1
1.4E-1 1.5E-1 1.6E-1 1.7E-1 1.8E-1 1.9E-1 2.0E-1 2 1E-1 2.2E-1 2.3E-1 2.4E-1 2 5E-1
2.6E-1 2.7E-1 2.8E-1 2.9E-1 3.0E-1 3.1E-1 3 2E-1 3 3E-1 3 4E-1 3 5E-1 3 6E-1 3 7E-1
3.8E-1 3 9E-1 4 0E-1 4 1E-1 4.2E-1 4.3E-1 4.4E-1 4 5E-1 4 6E-1 4 7E-1 4.8E-1 4.9E-1
5.0E-1 5.5E-1 6.0E-1 6.5E-1 7 0E-1 7.5E-1 8.0E-1 8 5E-1 9.0E-1 9 5E-1 1 0

Source probabilities for 250 MeV nucleon^{-1} iron beam

0 1.2908E-1 9.6122E-2 7 4700E-2 5.9932E-2 4 9284E-2 4.1334E-2 3.5229E-2
3 0429E-2 2.6583E-2 2.3448E-2 2.0858E-2 1.8690E-2 1 6856E-2 1 5290E-2 1 3941E-2
1.2770E-2 1.1746E-2 1.0846E-2 1 0049E-2 9.3407E-3 2 0722E-2 1.7661E-2 1.5255E-2
1 3326E-2 1 1755E-2 1.0456E-2 9.3697E-3 8.4504E-3 7.6653E-3 6 9889E-3 1 2290E-2
1.0475E-2 9.0479E-3 7.9042E-3 6.9722E-3 6.2019E-3 5 5574E-3 5 0121E-3 4.5465E-3
4 1453E-3 3.7970E-3 3 4926E-3 3.2249E-3 2.9880E-3 2 7774E-3 2 5891E-3 2 4202E-3
2 2679E-3 2.1302E-3 2.0052E-3 1.8913E-3 1.7872E-3 1 6919E-3 1 6043E-3 1.5236E-3
1.4492E-3 1.3803E-3 1.3163E-3 1.2570E-3 1.2017E-3 1 1501E-3 1.1020E-3 1.0569E-3
1.0147E-3 9.7501E-4 9.3774E-4 9.0266E-4 8.6960E-4 8.3840E-4 8.0892E-4 3.6544E-3
3.1146E-3 2.6903E-3 2.3502E-3 2.0731E-3 1.8441E-3 1.6524E-3 1 4903E-3 1.3519E-3
1 2326E-3 2.1675E-3 1.8474E-3 1 5957E-3 1 3940E-3 1.2296E-3 1.0938E-3 9.8010E-4
8.8394E-4 8.0181E-4 7.3106E-4 6.6965E-4 6.1596E-4 5.6874E-4 5.2697E-4 4 8982E-4
4.5662E-4 4.2683E-4 3.9997E-4 3.7568E-4 3.5363E-4 3.3355E-4 3.1520E-4 2.9838E-4
2 8294E-4 2.6871E-4 2.5558E-4 2.4342E-4 2 3215E-4 2.2168E-4 2.1193E-4 2 0284E-4
1.9434E-4 1.8640E-4 1.7895E-4 1.7195E-4 1.6538E-4 1 5919E-4 1.5336E-4 1 4786E-4
1 4266E-4 6.4450E-4 5.4930E-4 4.7446E-4 4.1449E-4 3.6562E-4 3 2523E-4 2 9143E-4
2 6283E-4 2.3841E-4 2.1738E-4

A.2. (continued)

Source probabilities for 1050 MeV nucleon^{-1} iron beam

0 1 3862E-1 1 0216E-1 7 8686E-2 6.2640E-2 5 1158E-2 4 2640E-2 3 6138E-2
3.1054E-2 2 7000E-2 2.3711E-2 2.1005E-2 1.8749E-2 1 6848E-2 1 5231E-2 1.3842E-2
1.2640E-2 1.1592E-2 1 0674E-2 9 8631E-3 9.1442E-3 2.0201E-2 1.7121E-2 1 4712E-2
1.2791E-2 1.1233E-2 9.9513E-3 8.8827E-3 7.9822E-3 7 2157E-3 6.5577E-3 1.1480E-2
9.7295E-3 8.3608E-3 7 2692E-3 6 3839E-3 5 6552E-3 5.0480E-3 4.5362E-3 4 1006E-3
3.7267E-3 3.4031E-3 3 1210E-3 2.8737E-3 2 6555E-3 2 4619E-3 2.2894E-3 2 1350E-3
1.9961E-3 1.8707E-3 1.7572E-3 1.6540E-3 1 5599E-3 1.4738E-3 1.3949E-3 1.3224E-3
1.2555E-3 1.1938E-3 1.1366E-3 1.0836E-3 1 0343E-3 9.8837E-4 9.4555E-4 9.0555E-4
8.6811E-4 8.3302E-4 8 0008E-4 7.6911E-4 7.3997E-4 7.1251E-4 6.8659E-4 3.0909E-3
2.6195E-3 2.2510E-3 1 9571E-3 1.7188E-3 1 5226E-3 1.3591E-3 1.2213E-3 1 1040E-3
1.0033E-3 1.7565E-3 1 4886E-3 1 2792E-3 1 1122E-3 9.7675E-4 8.6527E-4 7 7236E-4
6.9405E-4 6.2741E-4 5.7019E-4 5.2068E-4 4.7753E-4 4 3968E-4 4.0630E-4 3.7668E-4
3.5029E-4 3.2665E-4 3 0541E-4 2 8623E-4 2 6885E-4 2.5306E-4 2.3866E-4 2.2550E-4
2.1342E-4 2.0233E-4 1.9210E-4 1 8265E-4 1.7390E-4 1 6579E-4 1.5825E-4 1.5122E-4
1.4467E-4 1.3855E-4 1 3282E-4 1 2745E-4 1.2241E-4 1.1768E-4 1.1322E-4 1.0902E-4
1.0505E-4 4.7291E-4 4 0079E-4 3 4441E-4 2 9945E-4 2 6297E-4 2.3296E-4 2 0794E-4
1 8686E-4 1.6892E-4 1 5351E-4

APPENDIX B – EXAMPLES OF OTHER INPUT FILES

CONTENTS:

```
Setup of tissue equivalent proportional counter to study wall effects
1 1 -7.87E-5          -1 2      IMP:E=1        $ propane gas (ICRU 36)
2 2 -7.861            -2 -1     IMP E=1        $ stainless steel 316 anode and helix
3 0                   1         IMP E=0

c blank line above
c surface cards
c
1 SO            0 635           $ internal gas cavity (sphere radius is 6 35 mm)
2 CZ            0.05            $ stainless steel 316 anode/helix (cylinder radius is 0 5 mm)

c blank line above
c source card – 250 MeV iron beam (arbitrary beam)
c Source has the energy distribution given in the SI1 and SP1 cards, is located on
c       surface 1, and has a normal of –1 (inward normal)
c
MODE E
SDEF ERG=D1 SUR=1 NRM=-1
SI1 H     1.0E-3 1.2E-3 1.4E-3 1.6E-3 1.8E-3 2.0E-3 2.2E-3 2 4E-3 2.6E-3 2.8E-3 3 0E-3 3 2E-3
          3.4E-3 3.6E-3 3.8E-3 4 0E-3 4 2E-3 4 4E-3 4 6E-3 4 8E-3 5 0E-3 5.5E-3 6 0E-3 6.5E-3
          7.0E-3 7.5E-3 8 0E-3 8.5E-3 9.0E-3 9 5E-3 1.0E-2 1.1E-2 1 2E-2 1.3E-2 1 4E-2 1 5E-2
          1.6E-2 1.7E-2 1.8E-2 1.9E-2 2.0E-2 2 1E-2 2.2E-2 2.3E-2 2.4E-2 2.5E-2 2.6E-2 2.7E-2
          2.8E-2 2.9E-2 3.0E-2 3.1E-2 3.2E-2 3 3E-2 3.4E-2 3.5E-2 3 6E-2 3.7E-2 3 8E-2 3.9E-2
          4.0E-2 4.1E-2 4.2E-2 4.3E-2 4.4E-2 4 5E-2 4.6E-2 4.7E-2 4 8E-2 4.9E-2 5.0E-2 5.5E-2
          6.0E-2 6.5E-2 7 0E-2 7 5E-2 8 0E-2 8 5E-2 9 0E-2 9.5E-2 1.0E-1 1 1E-1 1.2E-1 1 3E-1
          1.4E-1 1.5E-1 1.6E-1 1.7E-1 1.8E-1 1 9E-1 2.0E-1 2 1E-1 2 2E-1 2.3E-1 2 4E-1 2 5E-1
          2.6E-1 2 7E-1 2 8E-1 2.9E-1 3.0E-1 3.1E-1 3.2E-1 3 3E-1 3.4E-1 3.5E-1 3 6E-1 3 7E-1
          3.8E-1 3 9E-1 4.0E-1 4 1E-1 4 2E-1 4 3E-1 4 4E-1 4.5E-1 4 6E-1 4 7E-1 4 8E-1 4.9E-1
          5.0E-1 5.5E-1 6.0E-1 6.5E-1 7 0E-1 7 5E-1 8.0E-1 8 5E-1 9.0E-1 9.5E-1 1 0
SP1 D     0 1.2908E-1 9.6122E-2 7.4700E-2 5.9932E-2 4 9284E-2 4.1334E-2 3.5229E-2
          3.0429E-2 2 6583E-2 2 3448E-2 2.0858E-2 1.8690E-2 1.6856E-2 1.5290E-2 1 3941E-2
          1.2770E-2 1.1746E-2 1.0846E-2 1 0049E-2 9 3407E-3 2 0722E-2 1.7661E-2 1.5255E-2
          1.3326E-2 1 1755E-2 1.0456E-2 9 3697E-3 8.4504E-3 7.6653E-3 6.9889E-3 1.2290E-2
          1.0475E-2 9 0479E-3 7.9042E-3 6.9722E-3 6.2019E-3 5.5574E-3 5.0121E-3 4 5465E-3
          4.1453E-3 3.7970E-3 3.4926E-3 3 2249E-3 2 9880E-3 2 7774E-3 2.5891E-3 2.4202E-3
          2.2679E-3 2 1302E-3 2 0052E-3 1.8913E-3 1.7872E-3 1.6919E-3 1.6043E-3 1.5236E-3
          1.4492E-3 1.3803E-3 1.3163E-3 1 2570E-3 1.2017E-3 1.1501E-3 1.1020E-3 1 0569E-3
          1.0147E-3 9 7501E-4 9 3774E-4 9.0266E-4 8 6960E-4 8.3840E-4 8.0892E-4 3 6544E-3
          3.1146E-3 2 6903E-3 2 3502E-3 2.0731E-3 1.8441E-3 1 6524E-3 1.4903E-3 1 3519E-3
          1.2326E-3 2 1675E-3 1.8474E-3 1.5957E-3 1.3940E-3 1.2296E-3 1 0938E-3 9.8010E-4
          8.8394E-4 8.0181E-4 7.3106E-4 6.6965E-4 6 1596E-4 5 6874E-4 5.2697E-4 4 8982E-4
          4.5662E-4 4 2683E-4 3.9997E-4 3 7568E-4 3.5363E-4 3 3355E-4 3.1520E-4 2.9838E-4
          2.8294E-4 2 6871E-4 2.5558E-4 2.4342E-4 2.3215E-4 2.2168E-4 2 1193E-4 2.0284E-4
          1.9434E-4 1.8640E-4 1.7895E-4 1.7195E-4 1.6538E-4 1.5919E-4 1.5336E-4 1 4786E-4
          1 4266E-4 6 4450E-4 5 4930E-4 4.7446E-4 4 1449E-4 3 6562E-4 3 2523E-4 2 9143E-4
          2.6283E-4 2.3841E-4 2.1738E-4
```

Figure B.1. MCNP input file for a 250 MeV nucleon^{-1} iron beam on a wall-less TEPC – determination of the particle flux in the propane gas.

```
c
c material cards
c
M1        1000.     -0.103      $ hydrogen in propane gas (ICRU36)
          6000.     -0.569      $ carbon
          7000.     -0.035      $ nitrogen
          8000      -0.293      $ oxygen
M2        24000     -0.16       $ chromium in stainless-steel 316 (web pages)
          28000.    -0.10       $ nickel
          6000.     -0.0008     $ carbon
          25000.    -0.02       $ manganese
          14000.    -0.01       $ silicon
          15000.    -0.00045    $ phosphorus
          16000     -0.0003     $ sulfur
          26000.    -0.68845    $ iron
          42000     -0 02       $ molybdenum
c
c tally cards
c
F4:E 1  $ flux averaged over cell 1 (particles/cm2/source electron)
E4        1.2908E-1 9.6122E-2 7.4700E-2 5.9932E-2 4.9284E-2 4.1334E-2 3.5229E-2 3 0429E-2
          2.6583E-2 2 3448E-2 2.0858E-2 1.8690E-2 1.6856E-2 1.5290E-2 1 3941E-2 1.2770E-2
          1.1746E-2 1.0846E-2 1 0049E-2 9.3407E-3 2 0722E-2 1 7661E-2 1.5255E-2 1.3326E-2
          1.1755E-2 1 0456E-2 9 3697E-3 8.4504E-3 7 6653E-3 6 9889E-3 1.2290E-2 1 0475E-2
          9.0479E-3 7.9042E-3 6.9722E-3 6.2019E-3 5.5574E-3 5 0121E-3 4 5465E-3 4 1453E-3
          3 7970E-3 3.4926E-3 3 2249E-3 2.9880E-3 2 7774E-3 2.5891E-3 2.4202E-3 2.2679E-3
          2 1302E-3 2.0052E-3 1.8913E-3 1 7872E-3 1.6919E-3 1.6043E-3 1.5236E-3 1 4492E-3
          1.3803E-3 1.3163E-3 1 2570E-3 1.2017E-3 1.1501E-3 1.1020E-3 1.0569E-3 1 0147E-3
          9.7501E-4 9.3774E-4 9.0266E-4 8.6960E-4 8.3840E-4 8 0892E-4 3 6544E-3 3 1146E-3
          2.6903E-3 2.3502E-3 2.0731E-3 1.8441E-3 1 6524E-3 1.4903E-3 1.3519E-3 1.2326E-3
          2 1675E-3 1 8474E-3 1.5957E-3 1.3940E-3 1.2296E-3 1 0938E-3 9 8010E-4 8.8394E-4
          8 0181E-4 7.3106E-4 6 6965E-4 6 1596E-4 5.6874E-4 5.2697E-4 4 8982E-4 4 5662E-4
          4.2683E-4 3.9997E-4 3.7568E-4 3.5363E-4 3 3355E-4 3.1520E-4 2 9838E-4 2 8294E-4
          2 6871E-4 2.5558E-4 2.4342E-4 2 3215E-4 2.2168E-4 2 1193E-4 2.0284E-4 1.9434E-4
          1.8640E-4 1.7895E-4 1.7195E-4 1 6538E-4 1.5919E-4 1.5336E-4 1 4786E-4 1 4266E-4
          6.4450E-4 5 4930E-4 4.7446E-4 4.1449E-4 3 6562E-4 3 2523E-4 2 9143E-4 2 6283E-4
          2.3841E-4 2 1738E-4
c
c cutoff card after a million histories
c
NPS 1000000
PRINT
```

Figure B.1. (continued)

```
Setup of tissue equivalent proportional counter to study wall effects
1 1 -7.87E-5        -1 5       IMP:E=1      $ propane gas (ICRU 36)
2 1 -7.87E-5         1 -2 5    IMP:E=1
3 2 -1.1018          2 -3 5    IMP:E=1      $ A-150 plastic wall (ICRU 36)
4 3 -2.702           3 -4 5    IMP:E=1      $ aluminum shell
5 4 -7.861          -5 -4      IMP:E=1      $ stainless steel 316 anode and helix
6 0                  4         IMP:E=0

c blank line above
c surface cards
c
1 SO          0.3         $ impact parameter (variable between 1 – 6.3 mm)
2 SO          0.635       $ internal gas cavity (sphere radius is 6.35 mm)
2 SO          0.762       $ A-150 wall (sphere radius is 7.62 mm)
3 SO          0.7638      $ aluminum shell (sphere radius is 7.638 mm)
4 CZ          0.05        $ stainless steel 316 anode/helix (cylinder radius is 0.5 mm)

c blank line above
c source card – 250 MeV iron beam (arbitrary beam)
c Source has the energy distribution given in the SI1 and SP1 cards, is located on
c       surface 2, and has a normal of –1 (inward normal)
c
MODE E
SDEF ERG=D1 SUR=2 NRM=-1
SI1 H     1.0E-3 1.2E-3 1.4E-3 1.6E-3 1.8E-3 2.0E-3 2.2E-3 2.4E-3 2.6E-3 2.8E-3 3.0E-3 3.2E-3
          3.4E-3 3.6E-3 3.8E-3 4.0E-3 4.2E-3 4.4E-3 4.6E-3 4.8E-3 5.0E-3 5.5E-3 6.0E-3 6.5E-3
          7.0E-3 7.5E-3 8.0E-3 8.5E-3 9.0E-3 9.5E-3 1.0E-2 1.1E-2 1.2E-2 1.3E-2 1.4E-2 1.5E-2
          1.6E-2 1.7E-2 1.8E-2 1.9E-2 2.0E-2 2.1E-2 2.2E-2 2.3E-2 2.4E-2 2.5E-2 2.6E-2 2.7E-2
          2.8E-2 2.9E-2 3.0E-2 3.1E-2 3.2E-2 3.3E-2 3.4E-2 3.5E-2 3.6E-2 3.7E-2 3.8E-2 3.9E-2
          4.0E-2 4.1E-2 4.2E-2 4.3E-2 4.4E-2 4.5E-2 4.6E-2 4.7E-2 4.8E-2 4.9E-2 5.0E-2 5.5E-2
          6.0E-2 6.5E-2 7.0E-2 7.5E-2 8.0E-2 8.5E-2 9.0E-2 9.5E-2 1.0E-1 1.1E-1 1.2E-1 1.3E-1
          1.4E-1 1.5E-1 1.6E-1 1.7E-1 1.8E-1 1.9E-1 2.0E-1 2.1E-1 2.2E-1 2.3E-1 2.4E-1 2.5E-1
          2.6E-1 2.7E-1 2.8E-1 2.9E-1 3.0E-1 3.1E-1 3.2E-1 3.3E-1 3.4E-1 3.5E-1 3.6E-1 3.7E-1
          3.8E-1 3.9E-1 4.0E-1 4.1E-1 4.2E-1 4.3E-1 4.4E-1 4.5E-1 4.6E-1 4.7E-1 4.8E-1 4.9E-1
          5.0E-1 5.5E-1 6.0E-1 6.5E-1 7.0E-1 7.5E-1 8.0E-1 8.5E-1 9.0E-1 9.5E-1 1.0
SP1 D     0 1.2908E-1 9.6122E-2 7.4700E-2 5.9932E-2 4.9284E-2 4.1334E-2 3.5229E-2
          3.0429E-2 2.6583E-2 2.3448E-2 2.0858E-2 1.8690E-2 1.6856E-2 1.5290E-2 1.3941E-2
          1.2770E-2 1.1746E-2 1.0846E-2 1.0049E-2 9.3407E-3 2.0722E-2 1.7661E-2 1.5255E-2
          1.3326E-2 1.1755E-2 1.0456E-2 9.3697E-3 8.4504E-3 7.6653E-3 6.9889E-3 1.2290E-2
          1.0475E-2 9.0479E-3 7.9042E-3 6.9722E-3 6.2019E-3 5.5574E-3 5.0121E-3 4.5465E-3
          4.1453E-3 3.7970E-3 3.4926E-3 3.2249E-3 2.9880E-3 2.7774E-3 2.5891E-3 2.4202E-3
          2.2679E-3 2.1302E-3 2.0052E-3 1.8913E-3 1.7872E-3 1.6919E-3 1.6043E-3 1.5236E-3
          1.4492E-3 1.3803E-3 1.3163E-3 1.2570E-3 1.2017E-3 1.1501E-3 1.1020E-3 1.0569E-3
          1.0147E-3 9.7501E-4 9.3774E-4 9.0266E-4 8.6960E-4 8.3840E-4 8.0892E-4 3.6544E-3
          3.1146E-3 2.6903E-3 2.3502E-3 2.0731E-3 1.8441E-3 1.6524E-3 1.4903E-3 1.3519E-3
          1.2326E-3 2.1675E-3 1.8474E-3 1.5957E-3 1.3940E-3 1.2296E-3 1.0938E-3 9.8010E-4
          8.8394E-4 8.0181E-4 7.3106E-4 6.6965E-4 6.1596E-4 5.6874E-4 5.2697E-4 4.8982E-4
          4.5662E-4 4.2683E-4 3.9997E-4 3.7568E-4 3.5363E-4 3.3355E-4 3.1520E-4 2.9838E-4
          2.8294E-4 2.6871E-4 2.5558E-4 2.4342E-4 2.3215E-4 2.2168E-4 2.1193E-4 2.0284E-4
          1.9434E-4 1.8640E-4 1.7895E-4 1.7195E-4 1.6538E-4 1.5919E-4 1.5336E-4 1.4786E-4
          1.4266E-4 6.4450E-4 5.4930E-4 4.7446E-4 4.1449E-4 3.6562E-4 3.2523E-4 2.9143E-4
          2.6283E-4 2.3841E-4 2.1738E-4
```

Figure B.2. MCNP input file for a 250 MeV nucleon^{-1} iron beam on a solid-wall TEPC – determination of the energy deposition depending on the impact parameter.

```
c
c material cards
c
M1        1000.      -0.103       $ hydrogen in propane gas (ICRU36)
          6000.      -0.569       $ carbon
          7000.      -0.035       $ nitrogen
          8000.      -0.293       $ oxygen
M2        1000       -0.1015      $ hydrogen in A-150 plastic wall (ICRU36)
          6000.      -0.7765      $ carbon
          7000.      -0.035       $ nitrogen
          8000.      -0.052       $ oxygen
          9000       -0.017       $ fluorine
          20000.     -0.018       $ calcium
M3        13000      -1           $ aluminum in shell (CRC handbook)
M4        24000.     -0.16        $ chromium in stainless-steel 316 (web pages)
          28000.     -0.10        $ nickel
          6000.      -0.0008      $ carbon
          25000.     -0.02        $ manganese
          14000.     -0.01        $ silicon
          15000.     -0.00045     $ phosphorus
          16000.     -0.0003      $ sulfur
          26000.     -0.68845     $ iron
          42000.     -0.02        $ molybdenum
c
c tally cards
c
*F8:E 2   $ energy deposition in cell 2 (MeV/source electron)
c
c cutoff card after a thousand histories
c
NPS 1000
PRINT
```

Figure B.2. (continued)

```
Setup of tissue equivalent proportional counter to study wall effects
1 1 -7.87E-5        -1  3        IMP:E=1      $ propane gas (ICRU 36)
2 1 -7.87E-5         1 -2 3      IMP E=1
5 2 -7 861          -3 -2        IMP.E=1      $ stainless steel 316 anode and helix
6 0                  2           IMP E=0

c blank line above
c surface cards
c
1 SO            0.3              $ impact parameter (variable between 1 – 6.3 mm)
2 SO            0 635            $ internal gas cavity (sphere radius is 6.35 mm)
3 CZ            0 05             $ stainless steel 316 anode/helix (cylinder radius is 0 5 mm)

c blank line above
c source card – 250 MeV iron beam (arbitrary beam)
c Source has the energy distribution given in the SI1 and SP1 cards, is located on
c       surface 2, and has a normal of –1 (inward normal)
c
MODE E
SDEF ERG=D1 SUR=2 NRM=-1
SI1 H      1.0E-3 1.2E-3 1.4E-3 1.6E-3 1.8E-3 2 0E-3 2.2E-3 2 4E-3 2.6E-3 2.8E-3 3 0E-3 3.2E-3
           3 4E-3 3.6E-3 3.8E-3 4 0E-3 4.2E-3 4 4E-3 4 6E-3 4.8E-3 5.0E-3 5.5E-3 6 0E-3 6 5E-3
           7 0E-3 7.5E-3 8 0E-3 8.5E-3 9 0E-3 9.5E-3 1.0E-2 1.1E-2 1.2E-2 1 3E-2 1 4E-2 1 5E-2
           1 6E-2 1 7E-2 1.8E-2 1.9E-2 2 0E-2 2 1E-2 2 2E-2 2.3E-2 2 4E-2 2.5E-2 2.6E-2 2 7E-2
           2.8E-2 2 9E-2 3 0E-2 3 1E-2 3.2E-2 3 3E-2 3 4E-2 3.5E-2 3 6E-2 3.7E-2 3.8E-2 3 9E-2
           4 0E-2 4 1E-2 4 2E-2 4.3E-2 4 4E-2 4.5E-2 4.6E-2 4 7E-2 4.8E-2 4 9E-2 5.0E-2 5 5E-2
           6 0E-2 6.5E-2 7.0E-2 7.5E-2 8 0E-2 8.5E-2 9 0E-2 9.5E-2 1 0E-1 1 1E-1 1.2E-1 1 3E-1
           1.4E-1 1.5E-1 1.6E-1 1 7E-1 1.8E-1 1 9E-1 2 0E-1 2.1E-1 2 2E-1 2.3E-1 2 4E-1 2 5E-1
           2.6E-1 2 7E-1 2 8E-1 2.9E-1 3 0E-1 3 1E-1 3 2E-1 3 3E-1 3 4E-1 3.5E-1 3 6E-1 3 7E-1
           3.8E-1 3 9E-1 4.0E-1 4.1E-1 4.2E-1 4.3E-1 4 4E-1 4.5E-1 4 6E-1 4.7E-1 4 8E-1 4 9E-1
           5.0E-1 5.5E-1 6.0E-1 6.5E-1 7.0E-1 7 5E-1 8 0E-1 8 5E-1 9.0E-1 9 5E-1 1 0
SP1 D      0 1 2908E-1 9.6122E-2 7.4700E-2 5 9932E-2 4 9284E-2 4.1334E-2 3 5229E-2
           3 0429E-2 2.6583E-2 2.3448E-2 2.0858E-2 1 8690E-2 1.6856E-2 1.5290E-2 1.3941E-2
           1.2770E-2 1.1746E-2 1.0846E-2 1.0049E-2 9 3407E-3 2 0722E-2 1.7661E-2 1 5255E-2
           1.3326E-2 1 1755E-2 1.0456E-2 9.3697E-3 8 4504E-3 7 6653E-3 6 9889E-3 1 2290E-2
           1.0475E-2 9.0479E-3 7.9042E-3 6.9722E-3 6 2019E-3 5.5574E-3 5 0121E-3 4 5465E-3
           4.1453E-3 3.7970E-3 3.4926E-3 3.2249E-3 2 9880E-3 2 7774E-3 2.5891E-3 2 4202E-3
           2.2679E-3 2.1302E-3 2.0052E-3 1.8913E-3 1 7872E-3 1.6919E-3 1.6043E-3 1.5236E-3
           1.4492E-3 1.3803E-3 1.3163E-3 1.2570E-3 1.2017E-3 1.1501E-3 1.1020E-3 1.0569E-3
           1.0147E-3 9.7501E-4 9 3774E-4 9.0266E-4 8 6960E-4 8.3840E-4 8.0892E-4 3 6544E-3
           3.1146E-3 2.6903E-3 2.3502E-3 2.0731E-3 1.8441E-3 1 6524E-3 1 4903E-3 1 3519E-3
           1.2326E-3 2 1675E-3 1.8474E-3 1.5957E-3 1.3940E-3 1.2296E-3 1.0938E-3 9 8010E-4
           8.8394E-4 8.0181E-4 7.3106E-4 6.6965E-4 6.1596E-4 5.6874E-4 5.2697E-4 4.8982E-4
           4.5662E-4 4 2683E-4 3.9997E-4 3.7568E-4 3.5363E-4 3.3355E-4 3 1520E-4 2 9838E-4
           2 8294E-4 2.6871E-4 2.5558E-4 2 4342E-4 2 3215E-4 2.2168E-4 2 1193E-4 2 0284E-4
           1.9434E-4 1 8640E-4 1 7895E-4 1 7195E-4 1 6538E-4 1.5919E-4 1.5336E-4 1 4786E-4
           1.4266E-4 6 4450E-4 5.4930E-4 4.7446E-4 4 1449E-4 3 6562E-4 3.2523E-4 2.9143E-4
           2.6283E-4 2 3841E-4 2.1738E-4
```

Figure B.3. MCNP input file for a 250 MeV nucleon^{-1} iron beam on a wall-less TEPC – determination of the energy deposition depending on the impact parameter.

```
c
c material cards
c
M1      1000.     -0.103      $ hydrogen in propane gas (ICRU36)
        6000.     -0.569      $ carbon
        7000      -0.035      $ nitrogen
        8000.     -0 293      $ oxygen
M2      24000.    -0.16       $ chromium in stainless-steel 316 (web pages)
        28000.    -0 10       $ nickel
        6000      -0.0008     $ carbon
        25000.    -0.02       $ manganese
        14000.    -0 01       $ silicon
        15000     -0 00045    $ phosphorus
        16000.    -0.0003     $ sulfur
        26000.    -0 68845    $ iron
        42000     -0 02       $ molybdenum
c
c tally cards
c
*F8:E 2  $ energy deposition in cell 2 (MeV/source electron)
c
c cutoff card after a thousand histories
c
NPS 1000
PRINT
```

Figure B.3. (continued)

APPENDIX C – OUTPUT FILES

CONTENTS:

Table C.1. Flux results for the 250 MeV nucleon^{-1} iron beam with the source on surface 2, tally in cell 2, and cell 1 having zero importance.

MeV	#/cm²/se	MeV	#/cm²/se	MeV	#/cm²/se
1.0E-3	0	2.4E-2	9 5971E-6	1 8E-1	4 9703E-5
1.2E-3	3 6758E-6	2.5E-2	8.8689E-6	1.9E-1	5 1406E-5
1.4E-3	3.4739E-6	2.6E-2	9 6368E-6	2 0E-1	4 6910E-5
1 6E-3	3.2702E-6	2 7E-2	8.5927E-6	2 1E-1	4.6965E-5
1.8E-3	3 1753E-6	2.8E-2	9.5801E-6	2.2E-1	4 4422E-5
2.0E-3	3.0057E-6	2.9E-2	8.5651E-6	2.3E-1	4.3128E-5
2.2E-3	2 9387E-6	3 0E-2	9.1956E-6	2 4E-1	4 2287E-5
2.4E-3	2.8673E-6	3.1E-2	9.3024E-6	2.5E-1	4.0744E-5
2.6E-3	2.8065E-6	3.2E-2	8.2845E-6	2.6E-1	3.9161E-5
2.8E-3	2.7506E-6	3.3E-2	9.2837E-6	2.7E-1	4 0031E-5
3.0E-3	2.7519E-6	3.4E-2	8.9072E-6	2.8E-1	3.5430E-5
3 2E-3	2.6073E-6	3.5E-2	8.2213E-6	2.9E-1	3.8100E-5
3.4E-3	2.5857E-6	3.6E-2	9.1993E-6	3.0E-1	3.3618E-5
3.6E-3	2.6341E-6	3.7E-2	8.8099E-6	3.1E-1	3 5261E-5
3.8E-3	2.5236E-6	3.8E-2	7.9826E-6	3.2E-1	3 4185E-5
4 0E-3	2.4809E-6	3.9E-2	9.0082E-6	3.3E-1	3.0815E-5
4.2E-3	2.5734E-6	4 0E-2	8 8665E-6	3 4E-1	3.3075E-5
4.4E-3	2.3739E-6	4.1E-2	7.7797E-6	3 5E-1	3.1088E-5
4.6E-3	2.5438E-6	4.2E-2	8.5685E-6	3.6E-1	2.7748E-5
4.8E-3	2.3170E-6	4 3E-2	8 9562E-6	3 7E-1	2 9836E-5
5.0E-3	2.5022E-6	4.4E-2	8.4105E-6	3.8E-1	2.8337E-5
5.5E-3	5.9379E-6	4.5E-2	7.5680E-6	3.9E-1	2.5218E-5
6 0E-3	5.8349E-6	4.6E-2	8.5901E-6	4.0E-1	2.7048E-5
6.5E-3	5.7492E-6	4.7E-2	8.7723E-6	4.1E-1	2 6823E-5
7.0E-3	5.6109E-6	4 8E-2	8.2036E-6	4.2E-1	2 4245E-5
7.5E-3	5.5109E-6	4.9E-2	7.3826E-6	4.3E-1	2.2732E-5
8.0E-3	5.4904E-6	5.0E-2	8.3611E-6	4.4E-1	2.4431E-5
8.5E-3	5 6385E-6	5.5E-2	4 0655E-5	4.5E-1	2.3365E-5
9.0E-3	5.3259E-6	6.0E-2	3.9593E-5	4.6E-1	2.1485E-5
9.5E-3	5.2551E-6	6.5E-2	3.8541E-5	4.7E-1	2.0915E-5
1 0E-2	5.5405E-6	7.0E-2	3.7589E-5	4.8E-1	2.2172E-5
1 1E-2	1 0526E-5	7 5E-2	3.7340E-5	4.9E-1	2.0971E-5
1.2E-2	1.0382E-5	8.0E-2	3.7645E-5	5.0E-1	1.9707E-5
1.3E-2	1.0248E-5	8.5E-2	3.5515E-5	5.5E-1	9.2332E-5
1.4E-2	1 0064E-5	9.0E-2	3.4375E-5	6.0E-1	8.1089E-5
1.5E-2	9.8468E-6	9.5E-2	3.5772E-5	6.5E-1	7.0350E-5
1.6E-2	9.7607E-6	1.0E-1	3.2878E-5	7.0E-1	5.8481E-5
1 7E-2	1 0092E-5	1.1E-1	6.6259E-5	7.5E-1	4.7464E-5
1.8E-2	9 6020E-6	1.2E-1	6 3914E-5	8.0E-1	3.8846E-5
1 9E-2	9.3908E-6	1.3E-1	6.1128E-5	8 5E-1	3.0900E-5
2.0E-2	1.0026E-5	1.4E-1	5 8580E-5	9.0E-1	2.2849E-5
2 1E-2	9.1187E-6	1.5E-1	5.7045E-5	9.5E-1	1.4006E-5
2 2E-2	9 7896E-6	1.6E-1	5.6342E-5	1.0E+0	6.4863E-6
2 3E-2	9.0459E-6	1.7E-1	5.2551E-5	TOTAL	2.8040E-3

Table C.2. Flux results for the 1050 MeV nucleon^{-1} iron beam with the source on surface 2, tally in cell 2, and cell 1 having zero importance.

MeV	#/cm^2/se	MeV	#/cm^2/se	MeV	#/cm^2/se
1 0E-3	0	2.4E-2	7.9737E-6	1.8E-1	3.8033E-5
1.2E-3	3.3474E-6	2.5E-2	7.3374E-6	1.9E-1	3.8785E-5
1.4E-3	3 1512E-6	2 6E-2	7.9687E-6	2.0E-1	3 5886E-5
1.6E-3	2.9618E-6	2.7E-2	7.0972E-6	2.1E-1	3.5523E-5
1.8E-3	2.8682E-6	2.8E-2	7.8989E-6	2.2E-1	3.3912E-5
2.0E-3	2 7079E-6	2.9E-2	7.0307E-6	2.3E-1	3.3029E-5
2 2E-3	2.6442E-6	3 0E-2	7.5855E-6	2.4E-1	3.1963E-5
2 4E-3	2.5762E-6	3.1E-2	7.6273E-6	2.5E-1	3.0877E-5
2.6E-3	2.5168E-6	3.2E-2	6.7734E-6	2.6E-1	2.9830E-5
2.8E-3	2.4665E-6	3.3E-2	7.5890E-6	2 7E-1	2 9592E-5
3.0E-3	2.4589E-6	3.4E-2	7.2699E-6	2.8E-1	2 6369E-5
3.2E-3	2.3343E-6	3.5E-2	6.6671E-6	2.9E-1	2.8354E-5
3.4E-3	2.3013E-6	3.6E-2	7.4257E-6	3.0E-1	2.4854E-5
3.6E-3	2.3430E-6	3.7E-2	7.1500E-6	3.1E-1	2.6102E-5
3.8E-3	2.2395E-6	3.8E-2	6 4594E-6	3.2E-1	2.5125E-5
4.0E-3	2.2032E-6	3.9E-2	7.2909E-6	3.3E-1	2 2425E-5
4.2E-3	2.2765E-6	4 0E-2	7 2187E-6	3.4E-1	2.4400E-5
4 4E-3	2.1031E-6	4 1E-2	6.2385E-6	3.5E-1	2.2901E-5
4.6E-3	2.2492E-6	4.2E-2	6.9557E-6	3 6E-1	2 0055E-5
4.8E-3	2.0395E-6	4.3E-2	7 1963E-6	3.7E-1	2.1871E-5
5 0E-3	2.2052E-6	4.4E-2	6.8014E-6	3 8E-1	2.0831E-5
5.5E-3	5 2257E-6	4.5E-2	6.0730E-6	3 9E-1	1.8503E-5
6.0E-3	5.1122E-6	4.6E-2	6.8961E-6	4.0E-1	1.9754E-5
6 5E-3	5.0245E-6	4 7E-2	7 0598E-6	4 1E-1	1.9488E-5
7.0E-3	4.8840E-6	4.8E-2	6.5992E-6	4 2E-1	1.7909E-5
7.5E-3	4.7978E-6	4.9E-2	5.9207E-6	4 3E-1	1.5994E-5
8.0E-3	4.7610E-6	5 0E-2	6 7523E-6	4 4E-1	1 7749E-5
8 5E-3	4.8710E-6	5 5E-2	3.2485E-5	4 5E-1	1.7061E-5
9.0E-3	4.5967E-6	6.0E-2	3 1460E-5	4.6E-1	1.5640E-5
9.5E-3	4.5305E-6	6.5E-2	3 0620E-5	4.7E-1	1.4692E-5
1.0E-2	4.7542E-6	7.0E-2	2.9878E-5	4.8E-1	1.6154E-5
1 1E-2	8.9925E-6	7.5E-2	2 9428E-5	4.9E-1	1.5222E-5
1.2E-2	8 8637E-6	8.0E-2	2.9396E-5	5.0E-1	1.4073E-5
1 3E-2	8.7321E-6	8.5E-2	2.7890E-5	5.5E-1	6.5202E-5
1.4E-2	8.5014E-6	9.0E-2	2 6759E-5	6.0E-1	5.6237E-5
1.5E-2	8.3260E-6	9.5E-2	2.8135E-5	6.5E-1	4 9020E-5
1 6E-2	8.2533E-6	1 0E-1	2 5739E-5	7.0E-1	4.1783E-5
1.7E-2	8.5329E-6	1.1E-1	5 1581E-5	7.5E-1	3 5846E-5
1.8E-2	8.0793E-6	1.2E-1	4 8796E-5	8 0E-1	2 8914E-5
1.9E-2	7.8744E-6	1.3E-1	4.6764E-5	8.5E-1	2.2430E-5
2 0E-2	8 3407E-6	1.4E-1	4.4525E-5	9.0E-1	1.6104E-5
2.1E-2	7.5903E-6	1.5E-1	4 3568E-5	9.5E-1	9.8456E-6
2.2E-2	8.1467E-6	1.6E-1	4.3008E-5	1.0E+0	4.7332E-6
2.3E-2	7 4904E-6	1.7E-1	3.9977E-5	TOTAL	2.1402E-3

Table C.3. Flux results for the 250 MeV nucleon^{-1} iron beam with the source on surface 2 and tally in cell 2.

MeV	#/cm^2/se	MeV	#/cm^2/se	MeV	#/cm^2/se
1.0E-3	0	2.4E-2	9.8132E-6	1 8E-1	5.3974E-5
1.2E-3	3 7553E-6	2.5E-2	9.0630E-6	1.9E-1	5.5971E-5
1.4E-3	3.5473E-6	2.6E-2	9.8527E-6	2.0E-1	5 1287E-5
1.6E-3	3.3383E-6	2.7E-2	8.7932E-6	2.1E-1	5.1576E-5
1 8E-3	3.2401E-6	2.8E-2	9.7990E-6	2.2E-1	4.8863E-5
2.0E-3	3.0671E-6	2.9E-2	8 7679E-6	2.3E-1	4.7530E-5
2.2E-3	2.9980E-6	3 0E-2	9 4162E-6	2.4E-1	4.6678E-5
2.4E-3	2.9247E-6	3.1E-2	9.5271E-6	2.5E-1	4 5116E-5
2.6E-3	2.8620E-6	3.2E-2	8.4865E-6	2.6E-1	4.3464E-5
2.8E-3	2 8055E-6	3.3E-2	9.5118E-6	2.7E-1	4.4361E-5
3.0E-3	2.8058E-6	3.4E-2	9.1294E-6	2.8E-1	3.9404E-5
3.2E-3	2.6582E-6	3.5E-2	8.4345E-6	2.9E-1	4.2449E-5
3 4E-3	2.6363E-6	3.6E-2	9.4405E-6	3.0E-1	3.7438E-5
3.6E-3	2.6849E-6	3.7E-2	9.0440E-6	3.1E-1	3.9387E-5
3.8E-3	2.5718E-6	3.8E-2	8.2009E-6	3.2E-1	3.8167E-5
4.0E-3	2.5281E-6	3.9E-2	9.2535E-6	3 3E-1	3.4599E-5
4.2E-3	2.6225E-6	4 0E-2	9.1170E-6	3.4E-1	3.7137E-5
4 4E-3	2 4186E-6	4 1E-2	7 9971E-6	3.5E-1	3.4934E-5
4.6E-3	2 5914E-6	4.2E-2	8.8180E-6	3.6E-1	3 0993E-5
4.8E-3	2.3595E-6	4.3E-2	9.2207E-6	3.7E-1	3.3425E-5
5.0E-3	2.5487E-6	4.4E-2	8 6619E-6	3.8E-1	3 1828E-5
5.5E-3	6.0453E-6	4.5E-2	7.7866E-6	3.9E-1	2.8224E-5
6.0E-3	5.9397E-6	4 6E-2	8 8370E-6	4.0E-1	3.0375E-5
6.5E-3	5.8547E-6	4.7E-2	9.0355E-6	4.1E-1	3.0034E-5
7.0E-3	5.7143E-6	4.8E-2	8.4576E-6	4.2E-1	2.7082E-5
7.5E-3	5 6125E-6	4.9E-2	7.6047E-6	4.3E-1	2.5446E-5
8.0E-3	5.5909E-6	5.0E-2	8 6420E-6	4.4E-1	2.7214E-5
8 5E-3	5.7395E-6	5.5E-2	4.1987E-5	4.5E-1	2.6190E-5
9.0E-3	5.4229E-6	6.0E-2	4.0988E-5	4.6E-1	2.3945E-5
9 5E-3	5.3494E-6	6.5E-2	3.9994E-5	4.7E-1	2.3149E-5
1.0E-2	5.6411E-6	7.0E-2	3.9076E-5	4.8E-1	2.4577E-5
1.1E-2	1.0712E-5	7.5E-2	3.8876E-5	4.9E-1	2.3221E-5
1.2E-2	1 0577E-5	8.0E-2	3.9286E-5	5.0E-1	2.1780E-5
1.3E-2	1 0435E-5	8.5E-2	3.7173E-5	5 5E-1	1.0057E-4
1.4E-2	1.0252E-5	9 0E-2	3.6008E-5	6.0E-1	8.7120E-5
1.5E-2	1 0035E-5	9.5E-2	3.7616E-5	6 5E-1	7.3833E-5
1 6E-2	9.9536E-6	1 0E-1	3.4617E-5	7.0E-1	6.0350E-5
1 7E-2	1.0289E-5	1.1E-1	6.9906E-5	7.5E-1	4.8120E-5
1.8E-2	9.7965E-6	1.2E-1	6.7640E-5	8.0E-1	3.8938E-5
1 9E-2	9.5778E-6	1.3E-1	6.4972E-5	8.5E-1	3.0900E-5
2.0E-2	1.0232E-5	1.4E-1	6.2560E-5	9.0E-1	2.2849E-5
2 1E-2	9.3100E-6	1 5E-1	6.1198E-5	9 5E-1	1.4006E-5
2.2E-2	1.0002E-5	1.6E-1	6.0704E-5	1.0E+0	6 4863E-6
2 3E-2	9 2432E-6	1 7E-1	5.6819E-5	TOTAL	2 9974E-3

Table C.4. Flux results for the 1050 MeV nucleon^{-1} iron beam with the source on surface 2 and tally in cell 2.

MeV	#/cm²/se	MeV	#/cm²/se	MeV	#/cm²/se
1.0E-3	0	2 4E-2	8.1182E-6	1.8E-1	4.1046E-5
1.2E-3	3.4021E-6	2.5E-2	7.4660E-6	1.9E-1	4.1935E-5
1 4E-3	3.2023E-6	2 6E-2	8 1221E-6	2.0E-1	3.8785E-5
1.6E-3	3.0089E-6	2 7E-2	7.2342E-6	2.1E-1	3 8461E-5
1 8E-3	2 9129E-6	2 8E-2	8 0585E-6	2.2E-1	3.6850E-5
2.0E-3	2.7504E-6	2.9E-2	7.1767E-6	2.3E-1	3.5955E-5
2.2E-3	2 6853E-6	3.0E-2	7.7436E-6	2.4E-1	3 4869E-5
2.4E-3	2.6155E-6	3.1E-2	7 7907E-6	2 5E-1	3.3785E-5
2.6E-3	2.5550E-6	3 2E-2	6.9171E-6	2.6E-1	3.2672E-5
2.8E-3	2 5038E-6	3 3E-2	7.7489E-6	2.7E-1	3.2574E-5
3.0E-3	2 4960E-6	3.4E-2	7.4260E-6	2.8E-1	2.9009E-5
3.2E-3	2.3692E-6	3.5E-2	6.8151E-6	2.9E-1	3.1389E-5
3.4E-3	2.3360E-6	3.6E-2	7.6041E-6	3.0E-1	2 7432E-5
3.6E-3	2.3778E-6	3.7E-2	7 3176E-6	3 1E-1	2.8965E-5
3 8E-3	2.2731E-6	3 8E-2	6 6194E-6	3.2E-1	2.7951E-5
4.0E-3	2.2355E-6	3.9E-2	7.4674E-6	3.3E-1	2 4895E-5
4.2E-3	2 3106E-6	4.0E-2	7 3972E-6	3.4E-1	2 7162E-5
4 4E-3	2 1338E-6	4.1E-2	6 3973E-6	3 5E-1	2.5540E-5
4.6E-3	2.2805E-6	4.2E-2	7.1278E-6	3.6E-1	2.2314E-5
4.8E-3	2.0692E-6	4 3E-2	7 3765E-6	3.7E-1	2.4476E-5
5.0E-3	2.2364E-6	4.4E-2	6.9752E-6	3.8E-1	2.3290E-5
5.5E-3	5 3003E-6	4.5E-2	6.2284E-6	3.9E-1	2.0744E-5
6.0E-3	5.1872E-6	4.6E-2	7 0717E-6	4 0E-1	2.2056E-5
6.5E-3	5.0979E-6	4.7E-2	7.2419E-6	4 1E-1	2.1763E-5
7 0E-3	4.9542E-6	4.8E-2	6.7890E-6	4.2E-1	2.0037E-5
7.5E-3	4.8674E-6	4 9E-2	6.0798E-6	4.3E-1	1 8007E-5
8 0E-3	4.8288E-6	5 0E-2	6.9290E-6	4.4E-1	1.9867E-5
8.5E-3	4.9424E-6	5 5E-2	3.3407E-5	4.5E-1	1.9093E-5
9.0E-3	4.6629E-6	6 0E-2	3.2431E-5	4.6E-1	1 7413E-5
9 5E-3	4.5999E-6	6 5E-2	3.1627E-5	4.7E-1	1.6308E-5
1.0E-2	4.8260E-6	7.0E-2	3.0886E-5	4.8E-1	1.7931E-5
1.1E-2	9 1266E-6	7 5E-2	3.0505E-5	4 9E-1	1.6891E-5
1.2E-2	9.0006E-6	8 0E-2	3.0523E-5	5 0E-1	1 5592E-5
1.3E-2	8 8655E-6	8.5E-2	2 8973E-5	5 5E-1	7.1729E-5
1.4E-2	8.6329E-6	9.0E-2	2.7868E-5	6.0E-1	6.0848E-5
1.5E-2	8 4625E-6	9 5E-2	2 9335E-5	6 5E-1	5 1712E-5
1.6E-2	8 3880E-6	1 0E-1	2.6901E-5	7 0E-1	4 3141E-5
1.7E-2	8.6717E-6	1 1E-1	5 4046E-5	7.5E-1	3.6325E-5
1.8E-2	8 2139E-6	1.2E-1	5.1404E-5	8.0E-1	2.9006E-5
1 9E-2	8 0094E-6	1 3E-1	4 9400E-5	8.5E-1	2.2430E-5
2.0E-2	8 4840E-6	1 4E-1	4.7182E-5	9.0E-1	1.6104E-5
2.1E-2	7 7218E-6	1.5E-1	4.6346E-5	9 5E-1	9 8456E-6
2.2E-2	8 2907E-6	1 6E-1	4 5918E-5	1.0E+0	4.7332E-6
2.3E-2	7 6292E-6	1.7E-1	4.2908E-5	TOTAL	2 2753E-3

Table C.5. Flux results for the 250 MeV nucleon^{-1} iron beam with the source on surface 2 and tally in cell 1.

MeV	#/cm^2/se	MeV	#/cm^2/se	MeV	#/cm^2/se
1.0E-3	0	2.4E-2	3.3605E-7	1.8E-1	1 8943E-5
1.2E-3	5 0279E-7	2.5E-2	8.7128E-7	1.9E-1	1 8176E-5
1.4E-3	5.0942E-7	2 6E-2	7.3779E-7	2.0E-1	2.2573E-5
1.6E-3	4.2104E-7	2.7E-2	1.1101E-6	2.1E-1	3 4346E-5
1.8E-3	3.8228E-7	2.8E-2	4.8321E-7	2.2E-1	1.9165E-5
2.0E-3	2.9156E-7	2 9E-2	4.2727E-7	2.3E-1	2.9282E-5
2.2E-3	2.9176E-7	3.0E-2	4.0657E-7	2.4E-1	2.3152E-5
2.4E-3	3.0674E-7	3.1E-2	1.5171E-6	2.5E-1	2.5224E-5
2.6E-3	3.1387E-7	3.2E-2	6.4211E-7	2.6E-1	2.7437E-5
2.8E-3	3.0419E-7	3.3E-2	1.5014E-6	2.7E-1	2.2489E-5
3.0E-3	2.3283E-7	3.4E-2	1.7162E-6	2.8E-1	1.8840E-5
3.2E-3	2.2492E-7	3.5E-2	4.2821E-7	2.9E-1	2 2618E-5
3.4E-3	3.0783E-7	3 6E-2	1.0388E-6	3.0E-1	2.6791E-5
3.6E-3	3.2311E-7	3.7E-2	1.6968E-6	3.1E-1	2 1234E-5
3.8E-3	2.0638E-7	3.8E-2	1 8941E-6	3.2E-1	2.6594E-5
4.0E-3	2.2982E-7	3.9E-2	1.9529E-6	3.3E-1	1.7166E-5
4.2E-3	2.2119E-7	4 0E-2	4 5291E-7	3.4E-1	2.3558E-5
4.4E-3	2.3938E-7	4.1E-2	1.3078E-6	3.5E-1	2 4035E-5
4.6E-3	2 9436E-7	4 2E-2	3.1970E-6	3.6E-1	2.1205E-5
4.8E-3	2.3896E-7	4.3E-2	1.2898E-6	3 7E-1	2 3100E-5
5.0E-3	2 0923E-7	4.4E-2	3.3224E-6	3.8E-1	2 5067E-5
5.5E-3	5.8154E-7	4.5E-2	4.2613E-7	3.9E-1	1 8948E-5
6.0E-3	2.4509E-7	4.6E-2	9.1828E-7	4.0E-1	1.9131E-5
6 5E-3	5 6059E-7	4.7E-2	2.1058E-6	4.1E-1	2.6573E-5
7.0E-3	4.2481E-7	4 8E-2	1.5904E-6	4.2E-1	1.8510E-5
7.5E-3	3.1093E-7	4.9E-2	1.6135E-6	4.3E-1	2.1418E-5
8.0E-3	2 7672E-7	5.0E-2	5.7962E-7	4.4E-1	2.1426E-5
8.5E-3	5.9450E-7	5.5E-2	5.5088E-6	4.5E-1	2.5463E-5
9.0E-3	3.6009E-7	6 0E-2	7.7639E-6	4.6E-1	1.9827E-5
9.5E-3	2.7387E-7	6.5E-2	7.8819E-6	4.7E-1	2.0408E-5
1.0E-2	4.2275E-7	7.0E-2	3.9789E-6	4.8E-1	1.6700E-5
1.1E-2	1.7934E-6	7.5E-2	1.0508E-5	4.9E-1	1.9124E-5
1.2E-2	1.2723E-6	8.0E-2	8.6904E-6	5.0E-1	2.1583E-5
1.3E-2	9 0042E-7	8.5E-2	6.9368E-6	5 5E-1	9.1607E-5
1 4E-2	9.3692E-7	9.0E-2	5.8359E-6	6.0E-1	8.1569E-5
1.5E-2	2.4293E-7	9 5E-2	8.1482E-6	6.5E-1	6.3800E-5
1.6E-2	8.3868E-7	1.0E-1	6 3757E-6	7.0E-1	4.3854E-5
1.7E-2	2.2562E-6	1 1E-1	1.3240E-5	7.5E-1	2 4824E-5
1.8E-2	5.3212E-7	1.2E-1	1.8827E-5	8 0E-1	4 4443E-6
1.9E-2	5.0285E-7	1.3E-1	1.6319E-5	8 5E-1	0
2.0E-2	8 8249E-7	1.4E-1	2.2429E-5	9.0E-1	0
2.1E-2	2.7746E-7	1 5E-1	2.5118E-5	9.5E-1	0
2.2E-2	1 8608E-6	1.6E-1	1.5089E-5	1 0E+0	0
2.3E-2	1 5192E-6	1.7E-1	1.8620E-5	TOTAL	1 3090E-3

Table C.6. Flux results for the 1050 MeV nucleon[-1] iron beam with the source on surface 2 and tally in cell 1.

MeV	#/cm²/se	MeV	#/cm²/se	MeV	#/cm²/se
1.0E-3	0	2.4E-2	1.0185E-6	1.8E-1	1.3535E-5
1.2E-3	5.0949E-7	2.5E-2	6.4106E-7	1.9E-1	1.6095E-5
1.4E-3	5.3263E-7	2.6E-2	7.9717E-7	2.0E-1	1.4729E-5
1.6E-3	4.4059E-7	2.7E-2	1.3087E-6	2.1E-1	1.5857E-5
1.8E-3	5.0495E-7	2.8E-2	8.2951E-7	2.2E-1	1.6829E-5
2.0E-3	3.7964E-7	2.9E-2	1.1192E-6	2.3E-1	1.8119E-5
2.2E-3	4.7073E-7	3.0E-2	1.3893E-6	2.4E-1	1.9726E-5
2.4E-3	4.8502E-7	3.1E-2	6.9690E-7	2.5E-1	1.5770E-5
2.6E-3	4.1765E-7	3.2E-2	7.3121E-7	2.6E-1	1.5412E-5
2.8E-3	4.6862E-7	3.3E-2	9.6744E-7	2.7E-1	1.8343E-5
3.0E-3	5.1739E-7	3.4E-2	8.2539E-7	2.8E-1	1.0144E-5
3.2E-3	3.8844E-7	3.5E-2	0	2.9E-1	1.4257E-5
3.4E-3	4.5944E-7	3.6E-2	5.4833E-7	3.0E-1	1.4492E-5
3.6E-3	3.4990E-7	3.7E-2	1.5612E-6	3.1E-1	1.4543E-5
3.8E-3	3.2977E-7	3.8E-2	5.2776E-7	3.2E-1	2.1026E-5
4.0E-3	2.5419E-7	3.9E-2	5.8391E-7	3.3E-1	1.2954E-5
4.2E-3	3.1917E-7	4.0E-2	6.7527E-7	3.4E-1	2.0213E-5
4.4E-3	2.3938E-7	4.1E-2	5.5471E-7	3.5E-1	1.3683E-5
4.6E-3	3.6795E-7	4.2E-2	7.8413E-7	3.6E-1	1.6024E-5
4.8E-3	2.4539E-7	4.3E-2	1.2523E-6	3.7E-1	1.8005E-5
5.0E-3	2.1430E-7	4.4E-2	5.5521E-7	3.8E-1	1.4823E-5
5.5E-3	5.6942E-7	4.5E-2	1.4870E-6	3.9E-1	1.8253E-5
6.0E-3	5.4048E-7	4.6E-2	0	4.0E-1	1.5411E-5
6.5E-3	4.1031E-7	4.7E-2	1.1793E-6	4.1E-1	1.4095E-5
7.0E-3	4.1253E-7	4.8E-2	3.3668E-7	4.2E-1	1.6700E-5
7.5E-3	2.1746E-7	4.9E-2	4.3075E-7	4.3E-1	1.6498E-5
8.0E-3	3.3001E-7	5.0E-2	3.2445E-6	4.4E-1	1.7258E-5
8.5E-3	1.6138E-7	5.5E-2	3.4797E-6	4.5E-1	7.5589E-6
9.0E-3	1.9697E-7	6.0E-2	5.6664E-6	4.6E-1	1.6620E-5
9.5E-3	7.3302E-7	6.5E-2	5.8393E-6	4.7E-1	1.1099E-5
1.0E-2	2.9282E-7	7.0E-2	5.6648E-6	4.8E-1	1.6207E-5
1.1E-2	6.8224E-7	7.5E-2	3.9110E-6	4.9E-1	1.4743E-5
1.2E-2	2.5624E-7	8.0E-2	6.5128E-6	5.0E-1	1.0401E-5
1.3E-2	8.8250E-7	8.5E-2	3.2049E-6	5.5E-1	6.6162E-5
1.4E-2	1.0956E-6	9.0E-2	5.9227E-6	6.0E-1	5.9549E-5
1.5E-2	6.6509E-7	9.5E-2	7.8155E-6	6.5E-1	5.1415E-5
1.6E-2	5.4268E-7	1.0E-1	7.1416E-6	7.0E-1	3.4765E-5
1.7E-2	0	1.1E-1	1.7001E-5	7.5E-1	1.5471E-5
1.8E-2	1.1494E-7	1.2E-1	1.5068E-5	8.0E-1	5.6815E-6
1.9E-2	4.6691E-7	1.3E-1	1.4007E-5	8.5E-1	0
2.0E-2	1.0169E-6	1.4E-1	1.5225E-5	9.0E-1	0
2.1E-2	1.3695E-6	1.5E-1	1.3353E-5	9.5E-1	0
2.2E-2	1.4571E-7	1.6E-1	1.0242E-5	1.0E+0	0
2.3E-2	9.7470E-7	1.7E-1	1.4779E-5	TOTAL	9.4132E-4

Table C.7. Flux results for the 250 MeV nucleon^{-1} iron beam with the source on surface 1, tally in cell 2, and cell 1 having zero importance.

MeV	#/cm²/se	MeV	#/cm²/se	MeV	#/cm²/se
1.0E-3	0	2.4E-2	9.3837E-6	1.8E-1	4.9626E-5
1.2E-3	3.5687E-6	2.5E-2	8.6776E-6	1.9E-1	5.1368E-5
1.4E-3	3.3728E-6	2.6E-2	9.4316E-6	2.0E-1	4.6832E-5
1.6E-3	3.1778E-6	2.7E-2	8.4103E-6	2.1E-1	4 7122E-5
1 8E-3	3 0849E-6	2.8E-2	9.3908E-6	2.2E-1	4.4296E-5
2.0E-3	2.9222E-6	2.9E-2	8.3780E-6	2.3E-1	4.2960E-5
2.2E-3	2.8579E-6	3.0E-2	9.0269E-6	2.4E-1	4.2098E-5
2.4E-3	2.7888E-6	3.1E-2	9.1273E-6	2.5E-1	4.0551E-5
2.6E-3	2.7283E-6	3.2E-2	8.1232E-6	2.6E-1	3.9013E-5
2.8E-3	2.6772E-6	3 3E-2	9.1111E-6	2.7E-1	3.9508E-5
3.0E-3	2.6765E-6	3.4E-2	8.7236E-6	2.8E-1	3.5000E-5
3.2E-3	2.5355E-6	3.5E-2	8.0641E-6	2.9E-1	3.7614E-5
3.4E-3	2 5134E-6	3.6E-2	9.0407E-6	3.0E-1	3.2969E-5
3.6E-3	2.5620E-6	3.7E-2	8.6582E-6	3.1E-1	3.4683E-5
3.8E-3	2.4566E-6	3.8E-2	7.8476E-6	3.2E-1	3.3592E-5
4.0E-3	2.4132E-6	3.9E-2	8 8610E-6	3.3E-1	3.0087E-5
4.2E-3	2 5027E-6	4.0E-2	8.7454E-6	3.4E-1	3.2393E-5
4.4E-3	2 3097E-6	4.1E-2	7.6465E-6	3.5E-1	3.0717E-5
4.6E-3	2.4720E-6	4.2E-2	8 4519E-6	3.6E-1	2 7105E-5
4.8E-3	2.2532E-6	4.3E-2	8.8210E-6	3.7E-1	2.9526E-5
5.0E-3	2.4343E-6	4 4E-2	8.2839E-6	3.8E-1	2 7901E-5
5.5E-3	5.7825E-6	4.5E-2	7.4856E-6	3.9E-1	2 4839E-5
6 0E-3	5.6778E-6	4.6E-2	8.4616E-6	4.0E-1	2.6442E-5
6.5E-3	5.5989E-6	4.7E-2	8.6499E-6	4.1E-1	2.6191E-5
7.0E-3	5.4631E-6	4.8E-2	8 1028E-6	4.2E-1	2.3810E-5
7.5E-3	5.3683E-6	4.9E-2	7.2684E-6	4.3E-1	2.2307E-5
8 0E-3	5.3443E-6	5 0E-2	8.2288E-6	4.4E-1	2.3907E-5
8 5E-3	5.4899E-6	5.5E-2	4.0144E-5	4.5E-1	2 3019E-5
9.0E-3	5 1877E-6	6.0E-2	3.9127E-5	4.6E-1	2.1112E-5
9.5E-3	5.1191E-6	6.5E-2	3.8108E-5	4.7E-1	2.0492E-5
1.0E-2	5.3994E-6	7.0E-2	3.7139E-5	4.8E-1	2.1746E-5
1.1E-2	1.0261E-5	7.5E-2	3.6946E-5	4.9E-1	2.0536E-5
1.2E-2	1.0115E-5	8.0E-2	3.7250E-5	5.0E-1	1.9258E-5
1.3E-2	9.9956E-6	8.5E-2	3.5308E-5	5.5E-1	8 9772E-5
1.4E-2	9.8078E-6	9.0E-2	3.4200E-5	6.0E-1	7 9079E-5
1.5E-2	9.6104E-6	9.5E-2	3.5612E-5	6.5E-1	6.8898E-5
1.6E-2	9 5329E-6	1.0E-1	3.2797E-5	7.0E-1	5 8064E-5
1.7E-2	9 8540E-6	1.1E-1	6 6070E-5	7.5E-1	4.7714E-5
1.8E-2	9.3929E-6	1.2E-1	6.3881E-5	8.0E-1	3 9143E-5
1.9E-2	9.1746E-6	1.3E-1	6.1145E-5	8 5E-1	3.1080E-5
2 0E-2	9.7915E-6	1.4E-1	5.8693E-5	9.0E-1	2.2957E-5
2 1E-2	8.9281E-6	1.5E-1	5 7068E-5	9.5E-1	1 4020E-5
2.2E-2	9.5806E-6	1.6E-1	5.6287E-5	1.0E+0	6.4815E-6
2 3E-2	8.8566E-6	1.7E-1	5.2468E-5	TOTAL	2 7721E-3

Table C.8. Flux results for the 1050 MeV nucleon^{-1} iron beam with the source on surface 1, tally in cell 2, and cell 1 having zero importance.

MeV	#/cm^2/se	MeV	#/cm^2/se	MeV	#/cm^2/se
1.0E-3	0	2.4E-2	7.8023E-06	1 8E-1	3 7970E-05
1.2E-3	3.2446E-06	2 5E-2	7.1651E-06	1 9E-1	3 8844E-05
1.4E-3	3.0560E-06	2.6E-2	7.7913E-06	2 0E-1	3.5876E-05
1.6E-3	2.8719E-06	2.7E-2	6 9282E-06	2 1E-1	3.5424E-05
1.8E-3	2.7829E-06	2.8E-2	7 7097E-06	2.2E-1	3 3718E-05
2.0E-3	2.6281E-06	2 9E-2	6 8833E-06	2.3E-1	3.2737E-05
2 2E-3	2.5655E-06	3.0E-2	7 4223E-06	2 4E-1	3.1890E-05
2 4E-3	2.5013E-06	3.1E-2	7.4747E-06	2 5E-1	3.0736E-05
2.6E-3	2.4439E-06	3.2E-2	6 6249E-06	2 6E-1	2.9649E-05
2.8E-3	2 3976E-06	3.3E-2	7.4350E-06	2.7E-1	2.9407E-05
3.0E-3	2.3913E-06	3.4E-2	7 1190E-06	2.8E-1	2.6082E-05
3.2E-3	2.2670E-06	3.5E-2	6.5374E-06	2.9E-1	2 8022E-05
3.4E-3	2.2358E-06	3.6E-2	7.2815E-06	3.0E-1	2 4556E-05
3.6E-3	2.2733E-06	3.7E-2	7.0133E-06	3.1E-1	2.5706E-05
3 8E-3	2.1773E-06	3.8E-2	6 3376E-06	3.2E-1	2.4794E-05
4.0E-3	2.1410E-06	3 9E-2	7 1566E-06	3.3E-1	2.2134E-05
4.2E-3	2.2117E-06	4 0E-2	7.1012E-06	3 4E-1	2 3857E-05
4.4E-3	2.0454E-06	4.1E-2	6 1280E-06	3.5E-1	2.2446E-05
4 6E-3	2.1878E-06	4 2E-2	6.8306E-06	3.6E-1	1 9681E-05
4.8E-3	1.9850E-06	4.3E-2	7 0711E-06	3 7E-1	2.1307E-05
5.0E-3	2 1471E-06	4.4E-2	6 6703E-06	3 8E-1	2.0512E-05
5 5E-3	5.0837E-06	4 5E-2	5.9837E-06	3 9E-1	1 8269E-05
6.0E-3	4 9735E-06	4.6E-2	6.7919E-06	4 0E-1	1.9365E-05
6 5E-3	4.8836E-06	4 7E-2	6.9436E-06	4 1E-1	1.9112E-05
7.0E-3	4.7550E-06	4.8E-2	6.5137E-06	4.2E-1	1.7580E-05
7.5E-3	4.6661E-06	4 9E-2	5 8337E-06	4 3E-1	1.5633E-05
8.0E-3	4.6299E-06	5 0E-2	6.6362E-06	4.4E-1	1.7473E-05
8.5E-3	4.7415E-06	5.5E-2	3.1983E-05	4 5E-1	1.6662E-05
9.0E-3	4 4733E-06	6.0E-2	3.0954E-05	4.6E-1	1.5261E-05
9.5E-3	4.4110E-06	6 5E-2	3.0204E-05	4 7E-1	1.4494E-05
1 0E-2	4.6337E-06	7.0E-2	2.9567E-05	4 8E-1	1.5721E-05
1.1E-2	8.7646E-06	7 5E-2	2.9133E-05	4 9E-1	1.4811E-05
1.2E-2	8.6269E-06	8.0E-2	2.9166E-05	5 0E-1	1 3806E-05
1.3E-2	8 5019E-06	8.5E-2	2 7622E-05	5.5E-1	6.4219E-05
1.4E-2	8.2861E-06	9 0E-2	2.6579E-05	6 0E-1	5.5709E-05
1.5E-2	8.1277E-06	9.5E-2	2.7966E-05	6.5E-1	4.8393E-05
1.6E-2	8.0487E-06	1 0E-1	2 5670E-05	7 0E-1	4.1323E-05
1.7E-2	8.3144E-06	1.1E-1	5.1417E-05	7 5E-1	3.6202E-05
1 8E-2	7.8874E-06	1.2E-1	4 8658E-05	8 0E-1	2 9311E-05
1 9E-2	7.6820E-06	1.3E-1	4.6692E-05	8.5E-1	2.2626E-05
2 0E-2	8 1451E-06	1.4E-1	4.4465E-05	9 0E-1	1.6191E-05
2 1E-2	7.4202E-06	1 5E-1	4 3495E-05	9 5E-1	9.8531E-06
2 2E-2	7.9665E-06	1.6E-1	4 2995E-05	1.0E+0	4.7332E-06
2.3E-2	7 3227E-06	1 7E-1	3 9812E-05	TOTAL	2 1166E-03

Table C.9. Flux results for the 250 MeV nucleon^{-1} iron beam with the source on surface 1 and tally in cell 2.

MeV	$\#/cm^2/se$	MeV	$\#/cm^2/se$	MeV	$\#/cm^2/se$
1.0E-3	0	2 4E-2	1 0422E-5	1.8E-1	5 3529E-5
1 2E-3	3.8252E-6	2.5E-2	9.6291E-6	1.9E-1	5.5273E-5
1 4E-3	3.6180E-6	2.6E-2	1.0463E-5	2.0E-1	5 0326E-5
1.6E-3	3 4117E-6	2.7E-2	9.3390E-6	2.1E-1	5.0523E-5
1.8E-3	3 3158E-6	2.8E-2	1.0423E-5	2.2E-1	4.7387E-5
2.0E-3	3.1449E-6	2.9E-2	9.3022E-6	2.3E-1	4.5933E-5
2.2E-3	3.0797E-6	3.0E-2	1.0012E-5	2.4E-1	4 4936E-5
2.4E-3	3.0089E-6	3.1E-2	1.0118E-5	2.5E-1	4.3207E-5
2.6E-3	2.9476E-6	3.2E-2	9.0047E-6	2.6E-1	4.1450E-5
2.8E-3	2.8946E-6	3 3E-2	1.0101E-5	2.7E-1	4 1859E-5
3 0E-3	2 8965E-6	3.4E-2	9.6651E-6	2.8E-1	3.7035E-5
3.2E-3	2 7470E-6	3.5E-2	8.9453E-6	2.9E-1	3.9696E-5
3.4E-3	2.7254E-6	3.6E-2	1.0008E-5	3 0E-1	3.4716E-5
3.6E-3	2.7821E-6	3.7E-2	9.5855E-6	3.1E-1	3.6527E-5
3.8E-3	2.6701E-6	3.8E-2	8.7039E-6	3.2E-1	3 5319E-5
4.0E-3	2.6243E-6	3.9E-2	9.8179E-6	3.3E-1	3 1567E-5
4.2E-3	2.7245E-6	4.0E-2	9 6797E-6	3.4E-1	3 3916E-5
4.4E-3	2.5174E-6	4 1E-2	8.4522E-6	3 5E-1	3.2150E-5
4 6E-3	2.6957E-6	4.2E-2	9.3596E-6	3 6E-1	2 8309E-5
4.8E-3	2.4620E-6	4.3E-2	9.7623E-6	3.7E-1	3 0752E-5
5.0E-3	2.6609E-6	4 4E-2	9.1717E-6	3.8E-1	2 8983E-5
5.5E-3	6.3289E-6	4.5E-2	8.2699E-6	3.9E-1	2 5778E-5
6.0E-3	6.2219E-6	4.6E-2	9.3587E-6	4.0E-1	2 7410E-5
6.5E-3	6.1406E-6	4.7E-2	9.5655E-6	4 1E-1	2.7075E-5
7.0E-3	6.0002E-6	4.8E-2	8 9660E-6	4.2E-1	2 4619E-5
7.5E-3	5.9002E-6	4.9E-2	8.0327E-6	4.3E-1	2.3045E-5
8.0E-3	5.8813E-6	5.0E-2	9.1026E-6	4.4E-1	2.4750E-5
8.5E-3	6.0476E-6	5.5E-2	4.4318E-5	4.5E-1	2.3779E-5
9.0E-3	5.7179E-6	6 0E-2	4 3198E-5	4.6E-1	2 1794E-5
9.5E-3	5.6491E-6	6.5E-2	4.2038E-5	4.7E-1	2.1149E-5
1.0E-2	5.9585E-6	7.0E-2	4.1002E-5	4.8E-1	2.2363E-5
1.1E-2	1.1332E-5	7.5E-2	4.0733E-5	4.9E-1	2.1199E-5
1.2E-2	1.1186E-5	8.0E-2	4.0999E-5	5.0E-1	1.9955E-5
1.3E-2	1.1067E-5	8.5E-2	3.8750E-5	5.5E-1	9.2243E-5
1.4E-2	1.0869E-5	9.0E-2	3.7473E-5	6.0E-1	8.0767E-5
1.5E-2	1.0645E-5	9.5E-2	3.9056E-5	6.5E-1	7.0406E-5
1.6E-2	1.0566E-5	1.0E-1	3.5924E-5	7.0E-1	5 9137E-5
1.7E-2	1.0927E-5	1.1E-1	7.2130E-5	7.5E-1	4.8400E-5
1.8E-2	1 0419E-5	1.2E-1	6 9490E-5	8.0E-1	3 9605E-5
1.9E-2	1 0176E-5	1.3E-1	6.6457E-5	8.5E-1	3.1264E-5
2.0E-2	1.0865E-5	1.4E-1	6.3693E-5	9.0E-1	2.3037E-5
2.1E-2	9 9075E-6	1.5E-1	6.1842E-5	9.5E-1	1.4053E-5
2.2E-2	1.0634E-5	1.6E-1	6.1001E-5	1.0E+0	6.4815E-6
2.3E-2	9.8243E-6	1.7E-1	5.6680E-5	TOTAL	2.9588E-3

Table C.10. Flux results for the 1050 MeV nucleon^{-1} iron beam with the source on surface 1 and tally in cell 2.

MeV	#/cm^2/se	MeV	#/cm^2/se	MeV	#/cm^2/se
1.0E-3	0	2 4E-2	8 6372E-06	1 8E-1	4 0894E-05
1.2E-3	3.4646E-06	2.5E-2	7.9402E-06	1.9E-1	4 1699E-05
1.4E-3	3.2668E-06	2.6E-2	8.6401E-06	2.0E-1	3 8398E-05
1.6E-3	3.0723E-06	2.7E-2	7.6827E-06	2.1E-1	3.7933E-05
1.8E-3	2 9817E-06	2 8E-2	8 5411E-06	2.2E-1	3.5993E-05
2 0E-3	2 8195E-06	2.9E-2	7 6266E-06	2.3E-1	3.4895E-05
2.2E-3	2 7565E-06	3.0E-2	8.2228E-06	2.4E-1	3.4057E-05
2.4E-3	2 6912E-06	3.1E-2	8 2817E-06	2 5E-1	3.2738E-05
2 6E-3	2 6315E-06	3.2E-2	7.3392E-06	2.6E-1	3.1461E-05
2.8E-3	2.5843E-06	3.3E-2	8.2353E-06	2.7E-1	3.1210E-05
3.0E-3	2 5810E-06	3.4E-2	7.8900E-06	2.8E-1	2 7729E-05
3.2E-3	2.4490E-06	3.5E-2	7.2572E-06	2.9E-1	2.9660E-05
3.4E-3	2.4183E-06	3.6E-2	8.0657E-06	3.0E-1	2.5955E-05
3.6E-3	2.4625E-06	3 7E-2	7.7700E-06	3.1E-1	2.7163E-05
3.8E-3	2.3598E-06	3.8E-2	7.0291E-06	3.2E-1	2.6175E-05
4.0E-3	2.3222E-06	3 9E-2	7.9329E-06	3.3E-1	2.3310E-05
4.2E-3	2 4014E-06	4.0E-2	7 8561E-06	3 4E-1	2.5148E-05
4.4E-3	2 2231E-06	4.1E-2	6 7790E-06	3.5E-1	2 3606E-05
4.6E-3	2.3791E-06	4.2E-2	7.5561E-06	3 6E-1	2.0713E-05
4.8E-3	2.1612E-06	4.3E-2	7 8301E-06	3.7E-1	2 2372E-05
5.0E-3	2 3395E-06	4.4E-2	7.3824E-06	3 8E-1	2.1462E-05
5.5E-3	5.5459E-06	4 5E-2	6 6186E-06	3.9E-1	1.9116E-05
6 0E-3	5 4290E-06	4.6E-2	7.5136E-06	4.0E-1	2.0233E-05
6.5E-3	5 3384E-06	4 7E-2	7 6768E-06	4 1E-1	1.9987E-05
7.0E-3	5 2038E-06	4.8E-2	7 2046E-06	4.2E-1	1.8300E-05
7.5E-3	5 1135E-06	4.9E-2	6 4546E-06	4.3E-1	1.6300E-05
8.0E-3	5.0797E-06	5.0E-2	7.3221E-06	4.4E-1	1.8248E-05
8.5E-3	5 2088E-06	5.5E-2	3 5362E-05	4.5E-1	1.7259E-05
9.0E-3	4.9168E-06	6.0E-2	3.4177E-05	4.6E-1	1.5765E-05
9.5E-3	4 8537E-06	6.5E-2	3.3322E-05	4 7E-1	1.5001E-05
1.0E-2	5.1039E-06	7.0E-2	3 2539E-05	4.8E-1	1.6243E-05
1.1E-2	9 6649E-06	7.5E-2	3.2052E-05	4.9E-1	1.5318E-05
1.2E-2	9.5201E-06	8.0E-2	3 2049E-05	5.0E-1	1.4249E-05
1.3E-2	9 3840E-06	8.5E-2	3.0335E-05	5.5E-1	6 6115E-05
1.4E-2	9.1566E-06	9.0E-2	2 9128E-05	6.0E-1	5 7074E-05
1.5E-2	8.9860E-06	9.5E-2	3.0613E-05	6 5E-1	4 9468E-05
1.6E-2	8 8974E-06	1.0E-1	2.8036E-05	7.0E-1	4 2128E-05
1.7E-2	9 1980E-06	1 1E-1	5 6091E-05	7.5E-1	3.6595E-05
1 8E-2	8 7332E-06	1 2E-1	5 3083E-05	8 0E-1	2 9529E-05
1.9E-2	8 5002E-06	1.3E-1	5 0750E-05	8.5E-1	2 2757E-05
2.0E-2	9.0144E-06	1 4E-1	4.8251E-05	9.0E-1	1.6239E-05
2.1E-2	8.2196E-06	1.5E-1	4.7143E-05	9.5E-1	9.8850E-06
2.2E-2	8 8190E-06	1.6E-1	4 6437E-05	1.0E+0	4 7332E-06
2.3E-2	8 1108E-06	1 7E-1	4 3038E-05	TOTAL	2 2632E-03

Table C.11. Flux results for the 250 MeV nucleon^{-1} iron beam with the source on surface 1, tally in cell 1, and cell 2 having zero importance.

MeV	#/cm^2/se	MeV	#/cm^2/se	MeV	#/cm^2/se
1.0E-3	0	2.4E-2	2.1823E-3	1.8E-1	6.8416E-4
1.2E-3	1.3991E-2	2.5E-2	2.0007E-3	1.9E-1	5 8667E-4
1.4E-3	1 2880E-2	2.6E-2	1.9080E-3	2.0E-1	5 3065E-4
1.6E-3	1.1767E-2	2.7E-2	1.8057E-3	2.1E-1	5.2335E-4
1.8E-3	1.1053E-2	2.8E-2	1.7238E-3	2.2E-1	4 3961E-4
2.0E-3	1.0112E-2	2.9E-2	1.5915E-3	2.3E-1	4.3418E-4
2.2E-3	9.5226E-3	3.0E-2	1.4885E-3	2 4E-1	3.9097E-4
2.4E-3	8.9339E-3	3.1E-2	1.4541E-3	2.5E-1	3.3959E-4
2.6E-3	8.3902E-3	3.2E-2	1.3079E-3	2.6E-1	3.3802E-4
2.8E-3	7.9057E-3	3.3E-2	1.2380E-3	2.7E-1	3.3208E-4
3 0E-3	7.5748E-3	3.4E-2	1.1956E-3	2.8E-1	2.8282E-4
3 2E-3	6.9178E-3	3.5E-2	1.1145E-3	2.9E-1	2.7429E-4
3.4E-3	6.5841E-3	3.6E-2	1.0412E-3	3.0E-1	2.6490E-4
3.6E-3	6.4141E-3	3.7E-2	1.0222E-3	3.1E-1	2.5639E-4
3.8E-3	5.9244E-3	3.8E-2	1.0107E-3	3 2E-1	2.3760E-4
4 0E-3	5.6074E-3	3.9E-2	1 0065E-3	3.3E-1	2.3901E-4
4.2E-3	5 5478E-3	4.0E-2	9 2443E-4	3.4E-1	2 1619E-4
4 4E-3	4.9981E-3	4.1E-2	8 8824E-4	3.5E-1	2.0885E-4
4.6E-3	5.0929E-3	4.2E-2	8.2778E-4	3.6E-1	1.9474E-4
4.8E-3	4.5018E-3	4 3E-2	8 1437E-4	3.7E-1	1.8491E-4
5.0E-3	4.6421E-3	4 4E-2	7.3094E-4	3.8E-1	1.8052E-4
5.5E-3	1 0459E-2	4.5E-2	7.8569E-4	3.9E-1	1.6408E-4
6 0E-3	9 3804E-3	4.6E-2	7.2776E-4	4.0E-1	1.5253E-4
6.5E-3	8.4796E-3	4.7E-2	7.2318E-4	4.1E-1	1 7339E-4
7.0E-3	7.5624E-3	4.8E-2	6.5145E-4	4 2E-1	1.5215E-4
7.5E-3	6.8675E-3	4.9E-2	6.2275E-4	4 3E-1	1.5029E-4
8 0E-3	6.2938E-3	5.0E-2	5.8948E-4	4.4E-1	1.3311E-4
8 5E-3	5 9277E-3	5 5E-2	2.7436E-3	4.5E-1	1.1994E-4
9 0E-3	5.2993E-3	6.0E-2	2.3397E-3	4.6E-1	1 3591E-4
9.5E-3	4.7935E-3	6.5E-2	2 0291E-3	4.7E-1	1 2536E-4
1.0E-2	4.6865E-3	7.0E-2	1.7199E-3	4.8E-1	1.1972E-4
1.1E-2	8.1959E-3	7.5E-2	1.5949E-3	4.9E-1	1.1479E-4
1.2E-2	7.2073E-3	8.0E-2	1.3455E-3	5.0E-1	1 0541E-4
1.3E-2	6.2494E-3	8 5E-2	1.2240E-3	5 5E-1	4 7096E-4
1.4E-2	5.4605E-3	9.0E-2	1.2092E-3	6.0E-1	4.0972E-4
1.5E-2	4.9129E-3	9.5E-2	9 7863E-4	6 5E-1	3.8047E-4
1.6E-2	4.4425E-3	1.0E-1	9.5232E-4	7.0E-1	3.3975E-4
1.7E-2	3 9862E-3	1.1E-1	1.5897E-3	7.5E-1	2.6702E-4
1.8E-2	3.5891E-3	1.2E-1	1.4117E-3	8 0E-1	2.2252E-4
1.9E-2	3.2448E-3	1.3E-1	1.1938E-3	8.5E-1	2.1014E-4
2.0E-2	2.9941E-3	1 4E-1	1 1101E-3	9 0E-1	2.1444E-4
2 1E-2	2.7183E-3	1.5E-1	9 6298E-4	9.5E-1	1.8229E-4
2.2E-2	2.6259E-3	1.6E-1	8.3958E-4	1.0E+0	1 7370E-4
2.3E-2	2 3666E-3	1 7E-1	7 6343E-4	TOTAL	3 5315E-1

Table C.12. Flux results for the 1050 MeV nucleon^{-1} iron beam with the source on surface 1, tally in cell 1, and cell 2 having zero importance.

MeV	#/cm^2/se	MeV	#/cm^2/se	MeV	#/cm^2/se
1.0E-3	0	2.4E-2	1.9692E-03	1.8E-1	5 1956E-04
1 2E-3	1 4490E-02	2 5E-2	1.7750E-03	1 9E-1	4 4868E-04
1 4E-3	1 3229E-02	2 6E-2	1.6807E-03	2.0E-1	4 1254E-04
1 6E-3	1.2012E-02	2.7E-2	1 5275E-03	2.1E-1	4.0475E-04
1 8E-3	1.1234E-02	2 8E-2	1 4220E-03	2.2E-1	3 3061E-04
2.0E-3	1.0211E-02	2 9E-2	1.3400E-03	2 3E-1	3.2356E-04
2 2E-3	9.5912E-03	3.0E-2	1.3482E-03	2.4E-1	3 1326E-04
2.4E-3	8.9637E-03	3 1E-2	1.3138E-03	2.5E-1	2.8587E-04
2 6E-3	8.3748E-03	3 2E-2	1.1707E-03	2.6E-1	2 7376E-04
2.8E-3	7.8764E-03	3.3E-2	1.1111E-03	2 7E-1	2 5705E-04
3.0E-3	7 5413E-03	3 4E-2	1.0656E-03	2.8E-1	2.3877E-04
3.2E-3	6.8636E-03	3.5E-2	1.0124E-03	2 9E-1	2.1901E-04
3 4E-3	6.4975E-03	3 6E-2	9.8077E-04	3 0E-1	2.0121E-04
3.6E-3	6.3161E-03	3 7E-2	9.5447E-04	3 1E-1	1.8191E-04
3.8E-3	5.8168E-03	3.8E-2	8.2244E-04	3.2E-1	1 8461E-04
4.0E-3	5.5092E-03	3 9E-2	7.9832E-04	3 3E-1	1 9053E-04
4.2E-3	5.4485E-03	4.0E-2	7 9821E-04	3 4E-1	1 6367E-04
4.4E-3	4.8658E-03	4.1E-2	7 5115E-04	3 5E-1	1 6408E-04
4.6E-3	4 9542E-03	4.2E-2	6 9101E-04	3.6E-1	1 3905E-04
4.8E-3	4.3880E-03	4 3E-2	6.5286E-04	3.7E-1	1 3102E-04
5.0E-3	4 5274E-03	4.4E-2	6.2458E-04	3.8E-1	1 6113E-04
5.5E-3	1.0109E-02	4.5E-2	6 2073E-04	3.9E-1	1.1096E-04
6 0E-3	8.9930E-03	4 6E-2	6 3537E-04	4.0E-1	1.2464E-04
6.5E-3	8.0900E-03	4 7E-2	5 4699E-04	4 1E-1	1 0572E-04
7.0E-3	7 2323E-03	4 8E-2	5.9365E-04	4.2E-1	1 2007E-04
7.5E-3	6.5319E-03	4.9E-2	5 4387E-04	4.3E-1	1.0001E-04
8 0E-3	5 9502E-03	5 0E-2	5.0721E-04	4 4E-1	9 2515E-05
8 5E-3	5 5967E-03	5 5E-2	2.2882E-03	4.5E-1	9.3981E-05
9.0E-3	4.9814E-03	6.0E-2	1.9787E-03	4.6E-1	9 9380E-05
9.5E-3	4.5671E-03	6 5E-2	1.6518E-03	4 7E-1	8 0466E-05
1.0E-2	4.4031E-03	7 0E-2	1.5447E-03	4.8E-1	8 4669E-05
1 1E-2	7.5432E-03	7.5E-2	1.2871E-03	4 9E-1	8 3391E-05
1 2E-2	6.5696E-03	8 0E-2	1.1714E-03	5.0E-1	8 2960E-05
1.3E-2	5.7849E-03	8.5E-2	9.4633E-04	5.5E-1	3 7286E-04
1.4E-2	4.9893E-03	9.0E-2	9.5040E-04	6.0E-1	3.0796E-04
1.5E-2	4 4506E-03	9.5E-2	8 5597E-04	6 5E-1	2.9026E-04
1.6E-2	3 9231E-03	1.0E-1	7.3900E-04	7.0E-1	1.8925E-04
1 7E-2	3 6401E-03	1 1E-1	1 3856E-03	7 5E-1	1 8850E-04
1.8E-2	3 2620E-03	1 2E-1	1 1379E-03	8.0E-1	1 7030E-04
1 9E-2	2.9391E-03	1 3E-1	9.9477E-04	8.5E-1	1.7299E-04
2 0E-2	2.7301E-03	1 4E-1	8 5164E-04	9 0E-1	1.4886E-04
2 1E-2	2.4267E-03	1.5E-1	7.0485E-04	9.5E-1	1.2693E-04
2 2E-2	2 3729E-03	1.6E-1	6.6895E-04	1.0E+0	1.2166E-04
2 3E-2	2.1036E-03	1 7E-1	5.7422E-04	TOTAL	3.3370E-01

Table C.13. Flux results for the 250 MeV nucleon^{-1} iron beam with the source on surface 1 and tally in cell 1.

MeV	#/cm²/se	MeV	#/cm²/se	MeV	#/cm²/se
1.0E-3	0	2.4E-2	2.4572E-03	1.8E-1	7 4873E-04
1 2E-3	1 4839E-02	2.5E-2	2 2306E-03	1.9E-1	6 3921E-04
1.4E-3	1.3699E-02	2.6E-2	2 1338E-03	2.0E-1	5 7957E-04
1.6E-3	1.2541E-02	2.7E-2	1.9853E-03	2.1E-1	5 7735E-04
1.8E-3	1 1813E-02	2.8E-2	1.9314E-03	2.2E-1	4 8925E-04
2.0E-3	1.0824E-02	2.9E-2	1.7579E-03	2.3E-1	4.7663E-04
2.2E-3	1.0218E-02	3.0E-2	1.6432E-03	2.4E-1	4 1641E-04
2.4E-3	9.6125E-03	3.1E-2	1.6367E-03	2.5E-1	3.6411E-04
2.6E-3	9.0509E-03	3.2E-2	1.4477E-03	2.6E-1	3.6206E-04
2.8E-3	8.5432E-03	3.3E-2	1.3967E-03	2.7E-1	3 6336E-04
3 0E-3	8.1955E-03	3 4E-2	1.3447E-03	2.8E-1	3 0217E-04
3 2E-3	7.5009E-03	3.5E-2	1.2409E-03	2.9E-1	2 9458E-04
3.4E-3	7.1531E-03	3.6E-2	1.1540E-03	3.0E-1	2.8685E-04
3.6E-3	6.9848E-03	3.7E-2	1.1260E-03	3.1E-1	2.7331E-04
3 8E-3	6.4584E-03	3.8E-2	1.1244E-03	3.2E-1	2.5336E-04
4.0E-3	6.1093E-03	3.9E-2	1.1136E-03	3.3E-1	2.5427E-04
4.2E-3	6.0573E-03	4.0E-2	1.0160E-03	3.4E-1	2.2693E-04
4 4E-3	5.4600E-03	4.1E-2	9.9303E-04	3.5E-1	2.1927E-04
4.6E-3	5.5707E-03	4.2E-2	9.2961E-04	3.6E-1	2 0327E-04
4.8E-3	4.9306E-03	4.3E-2	8.9610E-04	3.7E-1	1 9630E-04
5.0E-3	5.0907E-03	4.4E-2	8 1204E-04	3.8E-1	1.9418E-04
5.5E-3	1 1459E-02	4.5E-2	8.5662E-04	3.9E-1	1.6858E-04
6.0E-3	1.0286E-02	4.6E-2	7.9450E-04	4.0E-1	1.6126E-04
6.5E-3	9.3161E-03	4 7E-2	8 0090E-04	4.1E-1	1 7849E-04
7.0E-3	8.3221E-03	4.8E-2	7.2979E-04	4.2E-1	1.6051E-04
7.5E-3	7.5683E-03	4 9E-2	6.8704E-04	4.3E-1	1.5688E-04
8 0E-3	6.9459E-03	5.0E-2	6.5761E-04	4.4E-1	1 3693E-04
8.5E-3	6.5312E-03	5.5E-2	3.0612E-03	4.5E-1	1.2720E-04
9.0E-3	5.8216E-03	6.0E-2	2.5926E-03	4.6E-1	1.3804E-04
9.5E-3	5.2929E-03	6.5E-2	2 2559E-03	4.7E-1	1.3148E-04
1.0E-2	5.1898E-03	7.0E-2	1.9260E-03	4.8E-1	1.2575E-04
1 1E-2	9.0877E-03	7.5E-2	1.7663E-03	4.9E-1	1.1751E-04
1.2E-2	7.9565E-03	8.0E-2	1.5019E-03	5.0E-1	1.1074E-04
1.3E-2	6.9236E-03	8.5E-2	1.3770E-03	5.5E-1	4 9030E-04
1.4E-2	6.0432E-03	9.0E-2	1.3348E-03	6.0E-1	4.2034E-04
1.5E-2	5.4476E-03	9.5E-2	1.0772E-03	6.5E-1	3.9171E-04
1.6E-2	4.9248E-03	1.0E-1	1.0562E-03	7.0E-1	3 4523E-04
1.7E-2	4.4407E-03	1.1E-1	1 7411E-03	7.5E-1	2 6986E-04
1.8E-2	3 9808E-03	1.2E-1	1.5520E-03	8.0E-1	2 2355E-04
1 9E-2	3.5928E-03	1.3E-1	1.3234E-03	8.5E-1	2 1219E-04
2.0E-2	3.3276E-03	1.4E-1	1.2165E-03	9.0E-1	2 1539E-04
2.1E-2	3.0220E-03	1.5E-1	1.0460E-03	9.5E-1	1.8237E-04
2.2E-2	2.9155E-03	1.6E-1	9.1735E-04	1.0E+0	1.7370E-04
2.3E-2	2.6231E-03	1.7E-1	8.3744E-04	TOTAL	3.8551E-01

Table C.14. Flux results for the 1050 MeV nucleon^{-1} iron beam with the source on surface 1 and tally in cell 1.

MeV	#/cm²/se	MeV	#/cm²/se	MeV	#/cm²/se
1.0E-3	0	2 4E-2	2 2021E-03	1 8E-1	5.6912E-04
1.2E-3	1 5307E-02	2.5E-2	1 9660E-03	1 9E-1	4 8993E-04
1.4E-3	1 4013E-02	2 6E-2	1.8712E-03	2 0E-1	4 4341E-04
1.6E-3	1 2756E-02	2.7E-2	1.6941E-03	2 1E-1	4.4461E-04
1.8E-3	1 1956E-02	2 8E-2	1.5838E-03	2.2E-1	3.5727E-04
2.0E-3	1 0888E-02	2.9E-2	1 4615E-03	2 3E-1	3 4693E-04
2.2E-3	1 0253E-02	3.0E-2	1.5022E-03	2 4E-1	3 3827E-04
2.4E-3	9.5990E-03	3.1E-2	1.4597E-03	2.5E-1	3 0589E-04
2.6E-3	8.9905E-03	3 2E-2	1.2782E-03	2.6E-1	2.9087E-04
2.8E-3	8 4728E-03	3.3E-2	1.2341E-03	2 7E-1	2.7635E-04
3.0E-3	8 1211E-03	3.4E-2	1.1780E-03	2 8E-1	2 5717E-04
3 2E-3	7.4088E-03	3.5E-2	1.1187E-03	2.9E-1	2.3330E-04
3.4E-3	7.0154E-03	3 6E-2	1.0801E-03	3.0E-1	2 1462E-04
3 6E-3	6.8341E-03	3 7E-2	1.0734E-03	3.1E-1	1.9308E-04
3.8E-3	6.2987E-03	3 8E-2	9 1394E-04	3.2E-1	1 9467E-04
4.0E-3	5.9775E-03	3.9E-2	8.7950E-04	3 3E-1	1 9931E-04
4 2E-3	5 9154E-03	4.0E-2	9.0550E-04	3 4E-1	1 7389E-04
4 4E-3	5 2891E-03	4 1E-2	8.2238E-04	3 5E-1	1.7192E-04
4 6E-3	5.3912E-03	4 2E-2	7 7045E-04	3.6E-1	1 4990E-04
4.8E-3	4 7768E-03	4 3E-2	7 5191E-04	3 7E-1	1.4061E-04
5.0E-3	4 9334E-03	4.4E-2	7 0593E-04	3 8E-1	1 6914E-04
5.5E-3	1.1029E-02	4.5E-2	6 8524E-04	3 9E-1	1 1580E-04
6.0E-3	9.8216E-03	4.6E-2	7.0634E-04	4 0E-1	1.3277E-04
6.5E-3	8.8461E-03	4.7E-2	6.0956E-04	4 1E-1	1 0816E-04
7.0E-3	7 9198E-03	4 8E-2	6 5159E-04	4.2E-1	1.2278E-04
7.5E-3	7 1557E-03	4 9E-2	6 0272E-04	4 3E-1	1 0508E-04
8 0E-3	6.5274E-03	5.0E-2	5 6622E-04	4 4E-1	1.0035E-04
8.5E-3	6 1585E-03	5.5E-2	2.5389E-03	4 5E-1	9 5990E-05
9 0E-3	5 5013E-03	6.0E-2	2.1963E-03	4.6E-1	1.0172E-04
9 5E-3	5.0492E-03	6.5E-2	1 8401E-03	4 7E-1	8.3774E-05
1.0E-2	4.8621E-03	7.0E-2	1 7199E-03	4.8E-1	8.8578E-05
1.1E-2	8.3508E-03	7.5E-2	1 4317E-03	4 9E-1	8.6953E-05
1.2E-2	7.3044E-03	8 0E-2	1 2967E-03	5 0E-1	8.7892E-05
1.3E-2	6.4011E-03	8.5E-2	1.0445E-03	5.5E-1	3 8315E-04
1.4E-2	5 5272E-03	9 0E-2	1.0446E-03	6 0E-1	3.1637E-04
1.5E-2	4.9184E-03	9 5E-2	9 4051E-04	6 5E-1	2 9787E-04
1.6E-2	4.3549E-03	1 0E-1	8 1192E-04	7 0E-1	1.9274E-04
1 7E-2	4.0516E-03	1 1E-1	1 5054E-03	7.5E-1	1 9055E-04
1.8E-2	3.6258E-03	1 2E-1	1 2421E-03	8 0E-1	1.7153E-04
1 9E-2	3.2428E-03	1 3E-1	1 0810E-03	8.5E-1	1.7479E-04
2 0E-2	3 0422E-03	1 4E-1	9 2025E-04	9 0E-1	1.4954E-04
2 1E-2	2 6910E-03	1 5E-1	7 6941E-04	9 5E-1	1.2693E-04
2 2E-2	2.6381E-03	1 6E-1	7.2982E-04	1 0E+0	1.2166E-04
2 3E-2	2.3377E-03	1 7E-1	6.3206E-04	TOTAL	3.6289E-01

VITA

Jennifer Lynn Parsons was born in Grand Rapids, Michigan on June 4, 1976 After moving with her family multiple times in her childhood, she attended high school in Brentwood, Tennessee, where she graduated second in her class from Brentwood High School in June 1994. The following August she entered the University of Tennessee, Knoxville, where she received the four-year Neyland and McWherter scholarships. During her first two years at the University of Tennessee, she participated in the Lady Volunteers Swim Team in long distance freestyle events Also, while attending the university, she performed summer research at Vanderbilt University Medical Center in the Radiology Department and at Oak Ridge National Laboratory In May 1998, she received a Bachelor of Science degree with highest honors in nuclear engineering with a concentration in radiological engineering. She entered the Master's program in nuclear engineering at the University of Tennessee, Knoxville in August of 1998. At this time, she also received a four-year, Department of Energy Nuclear Engineering and Health Physics Fellowship. During the summer following her first year of graduate school, she performed a summer practicum at Los Alamos (New Mexico) National Laboratory in the Health Physics Measurement Group. She officially received the Master of Science degree in May 2000. Following the receipt of the Master's degree, she has elected to remain at the University of Tennessee and complete a Ph.D. in nuclear engineering.